Third Edition

AERODYNAMICS OF WIND TURBINES

MARTIN O. L. HANSEN

earthscan
from Routledge

Aerodynamics of Wind Turbines

Aerodynamics of Wind Turbines is the established essential text for the fundamental solutions to efficient wind turbine design. Now in its third edition, it has been substantially updated with respect to structural dynamics and control. The new control chapter includes details on how to design a classical pitch and torque regulator to control rotational speed and power, while the section on structural dynamics has been extended with a simplified mechanical system explaining the phenomena of forward and backward whirling modes. Readers will also benefit from a new chapter on vertical-axis wind turbines (VAWTs).

Topics covered include increasing mass flow through the turbine, performance at low and high wind speeds, assessment of the extreme conditions under which the turbine will perform, and the theory for calculating the lifetime of the turbine. The classical blade element momentum method is also covered, as are eigenmodes and the dynamic behaviour of a turbine.

The book describes the effects of the dynamics and how this can be modelled in an aeroelastic code, which is widely used in the design and verification of modern wind turbines. Furthermore, it examines how to calculate the vibration of the whole construction, as well as the time varying loads and global case studies.

Martin O. L. Hansen is a lecturer at the Technical University of Denmark, where he teaches wind turbine and related technologies.

This page intentionally left blank

Aerodynamics of Wind Turbines

Third edition

Martin O. L. Hansen

Routledge
Taylor & Francis Group
LONDON AND NEW YORK

earthscan
from Routledge

First published 2015
by Routledge
2 Park Square, Milton Park, Abingdon, Oxon OX14 4RN

and by Routledge
711 Third Avenue, New York, NY 10017

Routledge is an imprint of the Taylor & Francis Group, an informa business

British Library Cataloguing-in-Publication Data
A catalogue record for this book is available from the British Library

Library of Congress Cataloging-in-Publication Data
Hansen, Martin O. L.
Aerodynamics of wind turbines / Martin O. L. Hansen.
pages cm
1. Wind turbines – Aerodynamics. I. Title.
TJ828.H35 2015
621.4′5–dc23 2014042473

ISBN: 978-1-138-77507-7 (hbk)
ISBN: 978-1-315-76998-1 (ebk)

Typeset in Goudy
by HWA Text and Data Management, London

Contents

Figures

Tables

Preface

This book has been written based on notes from two courses given at the Technical University of Denmark on the mechanical aspects of wind turbines to give a basic understanding of how a wind turbine converts the kinetic energy of the wind into mechanical shaft power, which can be used to drive a generator to finally produce electrical power. This also includes various ways to control the loads and thus the output of the wind turbine by pitching the blades and by controlling the rotational speed. How to actually apply power electronics to vary the torque on the generator shaft to control the rotational rotor speed is not addressed in detail, and an interested reader is referred to textbooks on electrical motors and power electronics. Chapters describing the most important loads on the wind turbine construction are also included. Chapters 1–8, 10 and 11 could form the basis of an undergraduate course in basic wind turbine technology. From these chapters it is possible for a student knowing the geometry of a wind turbine to write a program based on the blade element momentum (BEM) method that can actually estimate the static loads and thus the mechanical power for various wind speeds, pitch angles and rotational speed. Such a program is a valuable tool in an optimization process, where the load distribution must be calculated many times for different design variables in order to maximize some desired property, such as, e.g., the annual energy production.

Building a wind turbine that will not break down during the design lifetime involves calculating time histories of the internal material loads for various unsteady conditions, the most important being a turbulent inflow, which varies in time, as well as space, over the rotor area. This involves building a so-called aeroelastic method that also takes into account the dynamic response of the wind turbine construction from the time varying aerodynamic, gravitational and other loads. The vibration velocities of the blades directly influence the aerodynamic loads, and there is therefore a strong coupling between the aerodynamics and the structural dynamics. Further, local accelerations must be taken into account when calculating the internal material loads. The outline of such a method is given in Chapters 9 and 12, describing respectively an unsteady blade element momentum method and some basic structural dynamics tools. Together with Chapters 14 and 15 these can be used in a graduate course

concerning wind turbine aeroelasticity. Chapter 14 deals with a method to construct a 3D turbulent inflow and Chapter 15 outlines how the fatigue damage is estimated from the various load time histories. These chapters should be supplemented with some norms describing all the different load cases that a wind turbine must be designed for, both with respect to fatigue and ultimate loads. Finally, the vertical-axis concept is addressed in Chapter 16.

1 General introduction to wind turbines

Before addressing more technical aspects of wind turbine technology, an attempt is made to give a short general introduction to wind energy. This involves a very brief historical part explaining the development of wind power, as well as a part dealing with economy and wind turbine design. It is far from intended to give a full historical review of wind turbines, but merely to mention some major milestones in their development and to show examples of historical exploitation of wind power.

Short historical review

The force of the wind can be very strong, as seen after the passage of a hurricane or a typhoon. Historically, people have harnessed this force peacefully, its most important use probably being the propulsion of ships using sails before the invention of the steam engine and the internal combustion engine. Wind has also been used in windmills to grind grain or to pump water for irrigation or, as in Holland, to prevent the ocean from flooding low-lying land. At the beginning of the twentieth century electricity came into use and windmills gradually became wind turbines as the rotor was connected to an electric generator.

The first electrical grids consisted of low-voltage DC cables with high losses. Electricity therefore had to be generated close to the site of use. On farms, small wind turbines were ideal for this purpose and in Denmark Poul la Cour, who was among the first to connect a windmill to a generator, gave a course for 'agricultural' electricians. La Cour had great foresight and in his school he installed one of the first wind tunnels in the world in order to investigate rotor aerodynamics. Gradually, however, diesel engines and steam turbines took over the production of electricity and only during the two world wars, when fuel was scarce, did wind power flourish again.

However, even after the Second World War, the development of more efficient wind turbines was still pursued in several countries such as Germany, the USA, France, the UK and Denmark. In Denmark, this work was undertaken by Johannes Juul, who was an employee in the utility company SEAS and a former student of la Cour. In the mid-1950s Juul introduced what was later called

the Danish concept by constructing the famous Gedser turbine, which had an upwind three-bladed, stall-regulated rotor, connected to an AC asynchronous generator running with almost constant speed. With the oil crisis in 1973, wind turbines suddenly became interesting again for countries which wanted to be less dependent on oil imports. Therefore many national research programmes were initiated to investigate the possibilities of utilizing wind energy. Large non-commercial prototypes were built to evaluate the economy of wind-produced electricity and to measure the loads on big wind turbines. Since the oil crisis, commercial wind turbines have gradually become an important multibillion dollar industry with annual growth rates of up to 20 per cent.

Why use wind power?

As already mentioned, a country or region where energy production is based on imported coal or oil will become more self-reliant by using alternatives such as wind power. Electricity produced from the wind produces no CO_2 emissions and therefore does not contribute to the greenhouse effect. Wind energy is relatively labour intensive and thus creates many jobs. In remote areas or areas with a weak electricity grid, wind energy can be used for charging batteries or can be combined with a diesel engine to save fuel whenever wind is available. Moreover wind turbines can be used for the desalination of water in coastal areas with little fresh water, for instance the Middle East. At windy sites the cost of electricity, measured in $/kWh, is competitive with the production cost from more conventional methods, for example, from coal-fired power plants.

To reduce the price further and to make wind energy more competitive with other production methods, wind turbine manufacturers are concentrating on bringing down the price of the turbine itself. Other factors, such as interest rates, cost of land and, not least, the amount of wind available at a certain site, also influence the production cost of the electrical energy generated. The production cost is computed as the investment plus the discounted maintenance cost divided by the discounted production measured in kWh over a period of typically 20 years. When the characteristics of a given turbine is known, i.e. the power for a given wind speed, as well as the annual wind distribution, the annual energy production can be estimated at a specific site.

Some of the drawbacks of wind energy can also be mentioned. Wind turbines create a certain amount of noise when they produce electricity. In modern wind turbines, manufacturers have managed to reduce almost all mechanical noise and are now working hard on reducing aerodynamic noise from the rotating blades. Noise is an important competition factor, especially in densely populated areas. Some people think that wind turbines are unsightly in the landscape, but as bigger and bigger machines gradually replace the older smaller machines, the actual number of wind turbines will be reduced and, at the same time, a greater capacity is available. If many turbines are to be erected in a region, it is important to have public acceptance. This can be achieved by allowing those people living close to the turbines to own a part of the project and thus share

the income. Noise and visual impact will in the future be less important as more wind turbines will be sited offshore.

One problem is that wind energy can only be produced when the wind is blowing. This is not a problem for most countries that are connected to big grids and can therefore buy electricity from the grid in the absence of wind. It is, however, an advantage to know in advance what resources will be available in the near future so that conventional power plants can adapt their production. Reliable weather forecasts are desirable since it takes some time for a coal-fired power plant to change its production. Combining wind energy with hydropower would be a perfect match, since it takes almost no time to open or close a valve at the inlet to a water turbine, i.e. one can save water in the reservoirs when the wind is sufficiently strong.

The wind resource

A wind turbine transforms the kinetic energy in the wind into mechanical energy in a shaft and finally into electrical energy in a generator. The maximum available energy, P_{max}, is thus obtained if theoretically the wind speed could be reduced to zero:

$$P_{max} = \tfrac{1}{2}\dot{m}V_o^2 = \tfrac{1}{2}\rho A V_o^3 \tag{1.1}$$

where $\dot{m}$ is the massflow through the rotor, V_o is the wind speed, ρ the density of the air and A the area where the wind speed has been reduced. The equation for the maximum available power is very important since it tells us that the power increases with the cube of the wind speed and only linearly with density and area. The available wind speed at a given site is therefore often first measured over a period of time before a project is initiated.

In practice one cannot reduce the wind speed to zero, so a power coefficient C_p is defined as the ratio between the actual power obtained and the maximum available power as given by Equation 1.1. A theoretical maximum for C_p exists denoted the Betz limit, $C_{p,\,max}$ =16/27=0.593. Modern optimized wind turbines operate close to this limit with C_p up to 0.5. Statistics have been gathered from many turbines sited in Denmark, and as rule of thumb, they produce approximately 1,000kWh/m^2/year. However, the production is very site dependent and the rule of thumb can only be used as a crude estimation and only for a site in Denmark.

Sailors discovered very early that it is more efficient to use the lift force rather than simple drag as the main source of propulsion. Lift and drag are the components of the force perpendicular and parallel to the direction of the relative wind, respectively. It is easy to show theoretically that it is much more efficient to use lift rather than drag when extracting power from the wind. All modern wind turbines therefore consist of a number of rotating blades which look like propeller blades. If the blades are connected to a vertical shaft, the turbine is called a vertical-axis wind turbine, VAWT, and if the shaft is horizontal, the turbine is called a horizontal-axis wind turbine, HAWT. For commercial wind turbines, the majority are HAWTs and the following text therefore mainly focuses on this

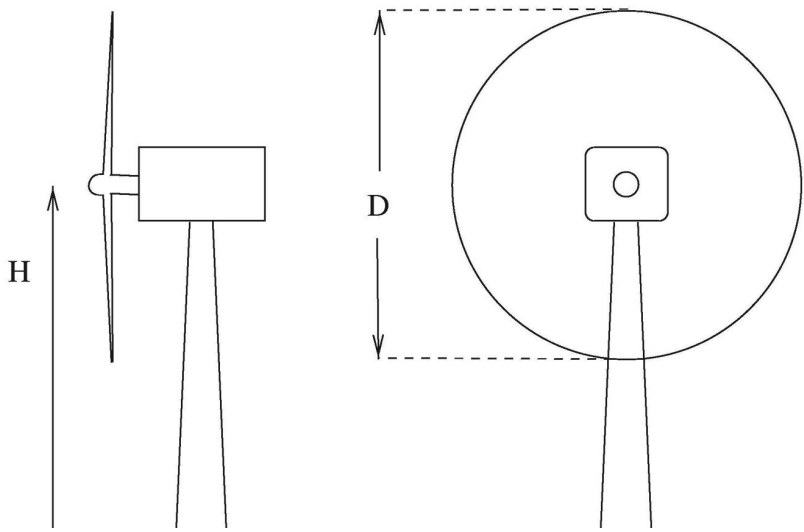

Figure 1.1 Horizontal-axis wind turbine, HAWT

type of machine. A HAWT, as sketched in Figure 1.1, is described in terms of the rotor diameter, the number of blades, the hub height, the rated power and the control strategy.

The hub height is important since the wind speed increases with the height above the ground, and the rotor diameter is important since this gives the area A in the formula for the available power. The ratio between the rotor diameter D and the hub height H is often approximately 1. The rated power is the maximum power allowed for the installed generator, and the control system must ensure that this power is not exceeded in high winds. The number of blades is most commonly two or three. Two-bladed wind turbines are cheaper since they have one blade fewer, but they rotate faster and cause more flickering to the eyes, whereas three-bladed wind turbines seem calmer and therefore less disturbing in a landscape. The aerodynamic efficiency is lower on a two-bladed than on a three-bladed wind turbine. A two-bladed wind turbine is often, but not always, a downwind machine, i.e. the rotor is placed downwind of the tower. Furthermore the connection to the shaft is not rigid, the rotor being mounted on the shaft through a hinge. This is called a teeter mechanism and the effect is that no bending moments are transformed from the rotor to the mechanical shaft. Such a construction is more flexible than the stiff three-bladed rotor, and some components can be built lighter and smaller and thus reduce the price of the wind turbine. The stability of the more flexible rotor must, however, be ensured. Downwind turbines are noisier than upstream turbines, since the passage of each blade in the wake behind the tower at each revolution causes low-frequency noise.

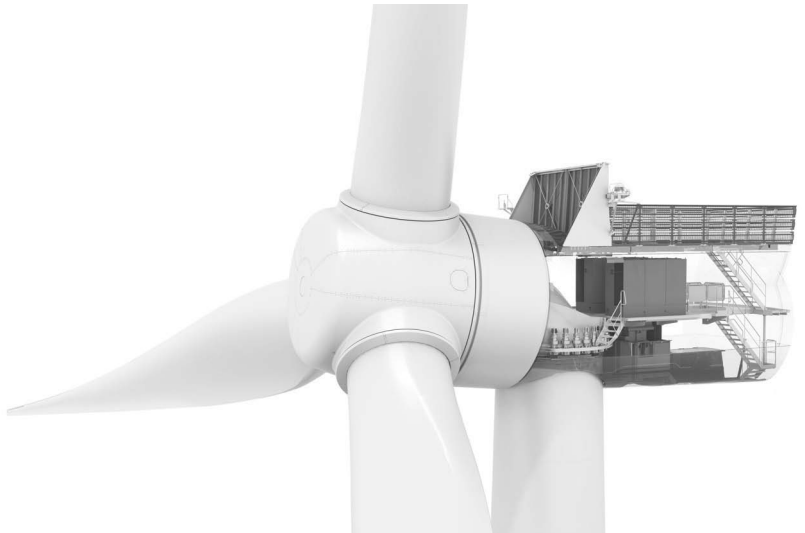

Figure 1.2 The nacelle of a modern Siemens wind turbine (with permission from Siemens Wind Power)

The rotational speed of a wind turbine rotor is approximately 10 to 50 RPM and the rotational speed of most generator shafts is approximately 1,000 to 3,000 RPM. Therefore a gearbox must be placed between the low-speed rotor shaft and the high-speed generator shaft. However, some turbines are equipped with multipole generators, which rotate so slowly that no gearbox is needed, as for example the Siemens wind turbine shown in Figure 1.2, where the blades and a ring of permanent magnets rotates in one large bearing.

Ideally a wind turbine rotor should always be perpendicular to the wind. On most wind turbines a wind vane is therefore mounted somewhere on the turbine to measure the direction of the wind. This signal is coupled with a yaw motor, which continuously turns the nacelle into the wind.

The rotor has undergone great development in recent years. The airfoils used on the first modern wind turbine blades were developed for aircrafts and were not optimized for the much higher angles of attack frequently experienced by a wind turbine blade. Even though old airfoils, as for instance, NACA63-4XX, were often successfully used in many older wind turbines, blade manufacturers have now started to use airfoils specifically optimized for wind turbines. Different materials have been tried in the construction of the blades, which must be sufficiently strong and stiff, have a high fatigue endurance limit and be as cheap as possible. Today most blades are built of glass-fibre-reinforced plastic, but other materials such as laminated wood are also used.

The text in this chapter, including the historical review, the arguments for supporting wind power and the short description of the technology, hopefully will motivate the reader to study the more technical sections concerned with aerodynamics, structures and loads on a wind turbine construction.

2 Two-dimensional aerodynamics

Wind turbine blades are long and slender structures where the spanwise velocity component is much lower than the streamwise component, and it is therefore assumed in many aerodynamic models that the flow at a given radial position is two dimensional and that 2-D airfoil data thus can be applied. Two-dimensional flow is confined to a single plane and if this plane is described with a coordinate system as shown in Figure 2.1, the velocity component in the z-direction is zero.

In order to realize a 2-D flow it is necessary to extrude an airfoil into a wing of infinite span. On a real wing the planform and twist changes along the span and the wing starts at a hub and ends in a tip, but for long slender wings as on modern gliders and wind turbines, Prandtl (see, for example, Prandtl and Tietjens, 1957) has shown that local 2-D data for the forces can be used if the angle of attack is corrected accordingly with the trailing vortices behind the wing. These effects will be dealt with later, but it is now clear that 2-D aerodynamics are of practical interest even though they are difficult to realize. Figure 2.1 shows the leading edge stagnation point present in the 2-D flow past an airfoil. The reacting force F from the flow is decomposed into a direction perpendicular to the velocity at infinity V_∞ and to a direction parallel to V_∞. The former component is denoted the lift, L, and the latter is called the drag, D, see Figure 2.2.

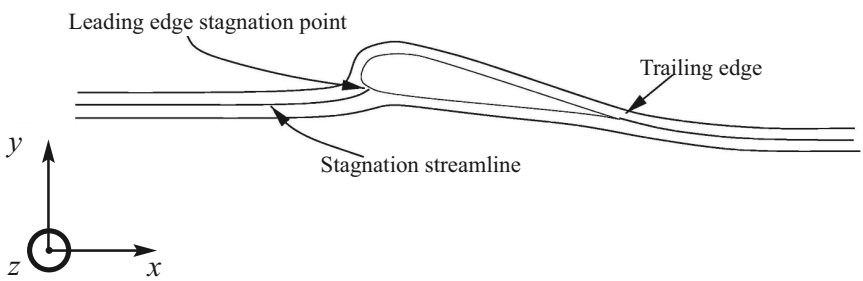

Figure 2.1 Schematic view of streamlines past an airfoil

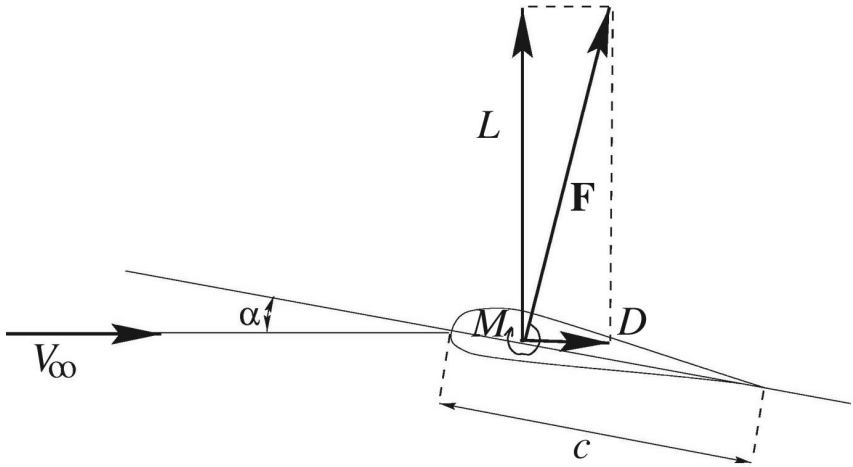

Figure 2.2 Definition of lift and drag

If the airfoil is designed for an aircraft it is obvious that the ratio, *L*/*D*, should be maximized. The lift is the force used to overcome gravity and the higher the lift, the higher mass can be lifted off the ground. In order to maintain a constant speed the drag must be balanced by a propulsion force delivered from an engine, and the smaller the drag, the smaller the engine required. Lift and drag coefficients C_l and C_d are defined as:

$$C_l = \frac{l}{\frac{1}{2}\rho V_\infty^2 c} \tag{2.1}$$

and

$$C_d = \frac{d}{\frac{1}{2}\rho V_\infty^2 c} \tag{2.2}$$

where ρ is the density and c the length of the airfoil often denoted as the chord. Note that the unit for the lift and drag in Equations (2.1) and (2.2) is force per length (N/m) and to indicate this they are therefore denoted with small letters. A chordline can be defined as the line from the trailing edge to the nose of the airfoil, see Figure 2.2. To describe the forces completely it is also necessary to know the moment M about a point in the airfoil. This point is often located on the chordline at $c/4$ from the leading edge. The moment is positive when it tends to turn the airfoil in Figure 2.2 clockwise (nose up) and a moment coefficient is defined as

$$C_m = \frac{m}{\frac{1}{2}\rho V_\infty^2 c^2} \tag{2.3}$$

The physical explanation of the lift is that the shape of the airfoil forces the streamlines to curve around the geometry, as indicated in Figure 2.3.

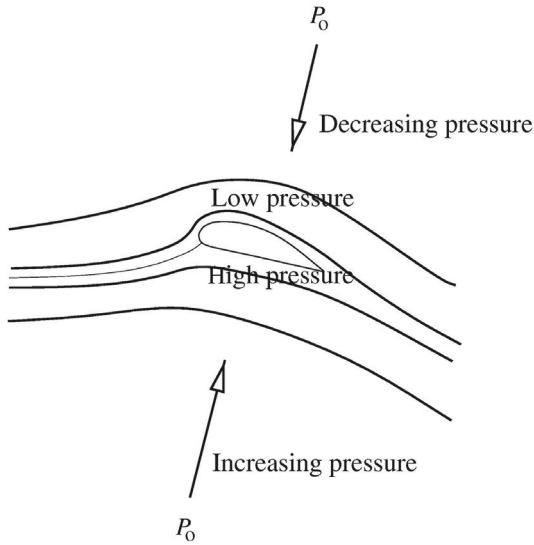

Figure 2.3 Explanation of the generation of lift

From basic fluid mechanics is known that a pressure gradient, $\frac{\partial p}{\partial r} = \rho \frac{V^2}{r}$, is necessary to curve the streamlines. r is the curvature of the streamline and V the speed. This pressure gradient acts like the centripetal force known from the circular motion of a particle. Since there is atmospheric pressure p_o far from the airfoil there must thus be a lower than atmospheric pressure on the upper side of the airfoil and a higher than atmospheric pressure on the lower side of the airfoil. This pressure difference gives a lifting force on the airfoil. When the airfoil is almost aligned with the flow the boundary layer stays attached and the associated drag is mainly caused by friction with the air.

The coefficients C_l, C_d and C_m are functions of α, Re, Ma. α is the angle of attack defined as the angle between the chordline and V_∞, Re is the Reynolds number based on the chord and V_∞, i.e. $Re = c\, V_\infty/\nu$, where ν is the kinematic viscosity. Ma denotes the Mach number, i.e. the ratio between V_∞ and the speed of sound. For a wind turbine and a slow-moving aircraft, the lift, drag and moment coefficients are only functions of α and Re. For a given airfoil the behaviour of C_l, C_d and C_m are measured or computed and plotted in so-called polars. An example of a measured polar for the FX67-K-170 airfoil is shown in Figure 2.4.

C_l increases linearly with α, with an approximate slope of 2π/rad, until a certain value of α, where a maximum value of C_l, is reached. Hereafter the airfoil is said to stall and C_l decreases in a very geometrically dependent manner. For small angles of attack, the drag coefficient C_d is almost constant, but increases rapidly after stall. The Reynolds number dependency can also be seen in Figure 2.4. It is seen, especially on the drag, that as the Reynolds number reaches a certain value, the Reynolds number dependency becomes small. The Reynolds

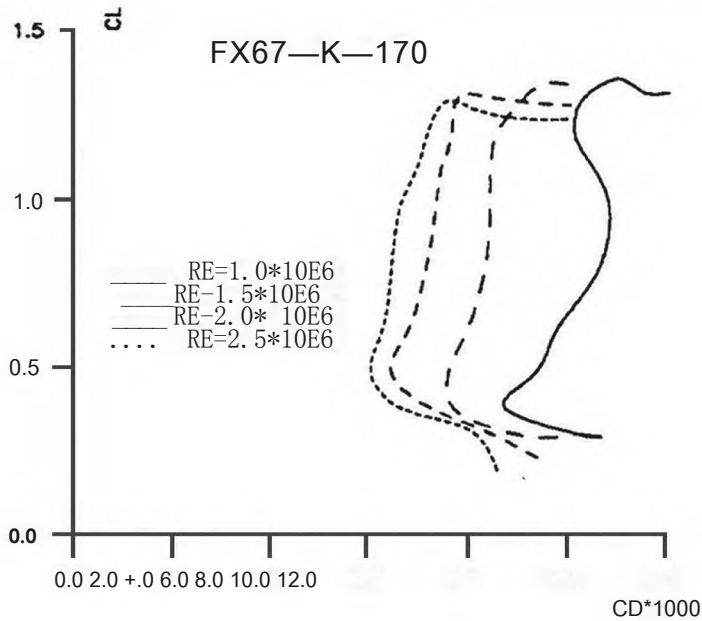

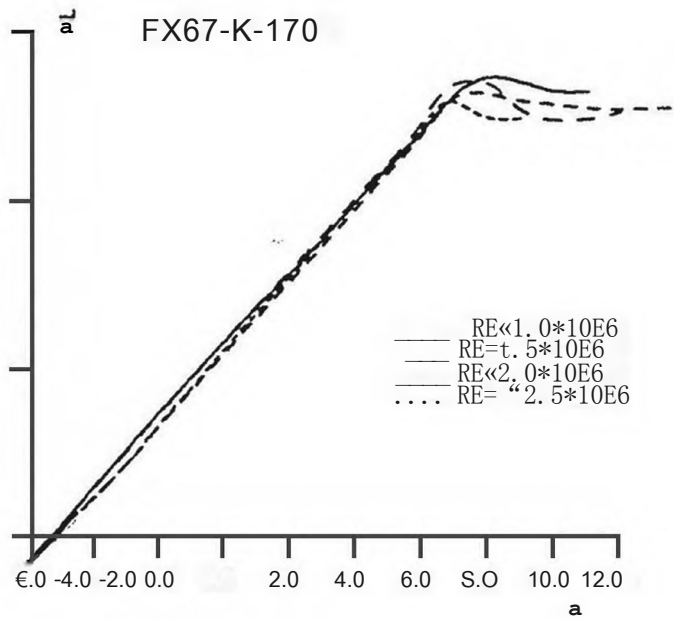

Figure 2.4 Polar for the FX67-K-170 airfoil

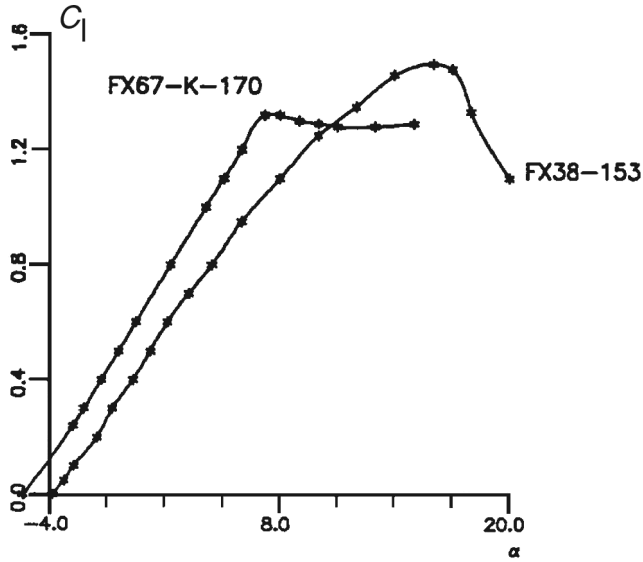

Figure 2.5 Different stall behaviours

number dependency is related to the point on the airfoil, where the boundary layer transition from laminar to turbulent flow occurs. The way an airfoil stalls is very dependent on the geometry. Thin airfoils with a sharp nose, i.e. high curvature around the leading edge, tend to stall more abruptly than thick airfoils. Different stall behaviours are shown in Figure 2.5, where $C_l(\alpha)$ is compared for two different airfoils. The FX38-153 is seen to lose its lift more rapidly than the FX67-K-170.

The explanation lies in the way the boundary layer separates from the upper side of the airfoil. If the separation starts at the trailing edge of the airfoil and increases slowly with increasing angle of attack, a soft stall is observed, but if the separation starts at the leading edge of the airfoil the entire boundary layer may separate almost simultaneously with a dramatic loss of lift. The behaviour of the viscous boundary layer is very complex and depends among other things on the curvature of the airfoil, the Reynolds number, the surface roughness and, for high speeds, also on the Mach number. Some description of the viscous boundary is given in this text but for a more elaborate description see standard textbooks on viscous boundary layers such as (White, 1991) and (Schlichting, 1968).

Figure 2.6 shows the computed streamlines for a NACA63-415 airfoil at an angle of attack of 5° and 15°, respectively.

For α=15° a trailing edge separation is observed. The forces on the airfoil stems from the pressure distribution $p(x)$ and the skin friction with the air $\tau_w = \mu \left(\partial u / \partial y \right)_{y=0}$ (x,y) is the surface coordinate system as shown in Figure 2.7,

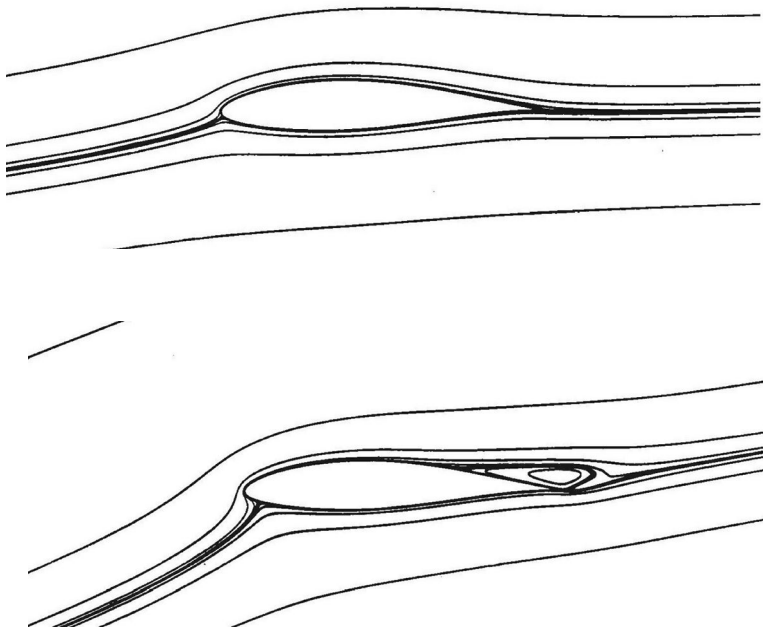

Figure 2.6 Computed streamlines for an angle of attack of 5° and 15°, respectively

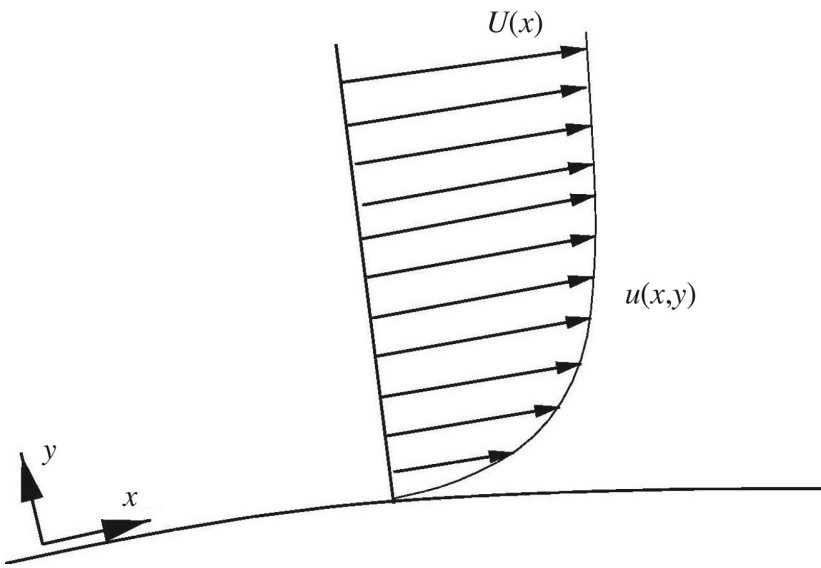

Figure 2.7 Viscous boundary layer at the wall of an airfoil

and μ is the dynamic viscosity. The skin friction is mainly contributing to the drag, whereas the force found from integrating the pressure has a lift and drag component. The drag component from the pressure distribution is known as the form drag and becomes very large when the airfoil stalls. The stall phenomenon is closely related to separation of the boundary layer (see next paragraph). Therefore the first rule in reducing drag is to avoid separation. Abbot and von Doenhoff (1959) give a lot of data for NACA (National Advisory Committee for Aeronautics) airfoils, which have been extensively used on small aircrafts, wind turbines and helicopters. Close to the airfoil there exists a viscous boundary layer due to the no-slip condition on the velocity at the wall, see Figure 2.7.

A boundary layer thickness is often defined as the normal distance $\delta(x)$ from the wall where $u(x)/U(x) = 0.99$. Further, the displacement thickness $\delta^*(x)$, the momentum thickness $\theta(x)$ and the shape factor $H(x)$ are defined as:

$$\delta^*(x) = \int_0^\delta (1 - \frac{u}{U}) dy, \tag{2.4}$$

$$\theta(x) = \int_0^\delta \frac{u}{U}(1 - \frac{u}{U}) dy, \tag{2.5}$$

$$H(x) = \frac{\delta^*}{\theta}. \tag{2.6}$$

The coordinate system (x,y) is a local system, where $x = 0$ is at the leading edge stagnation point and y is the normal distance from the wall. A turbulent boundary layer separates for H between 2 and 3. The stagnation streamline, see Figure 2.1, divides the fluid that flows over the airfoil from the fluid that flows under the airfoil. At the stagnation point the velocity is zero and the boundary layer thickness is small. The fluid, which flows over the airfoil, accelerates as it passes the leading edge and, since the leading edge is close to the stagnation point, the boundary layer is thin. It is known from viscous boundary layer theory (see, e.g. White, 1991) that the pressure is approximately constant from the surface to the edge of the boundary layer, i.e. $\partial p/\partial y = 0$. Outside the boundary layer the Bernoulli equation, see Appendix A, is valid and since the flow accelerates the pressure decreases, i.e. $\partial p/\partial x<0$. On the lower side the pressure gradient is much smaller since the curvature of the wall is small compared to the leading edge. At the trailing edge the pressure must be the same at the upper and lower side (the Kutta condition) and therefore the pressure must rise, $\partial p/\partial x>0$, from a minimum value somewhere on the upper side to a higher value at the trailing edge. An adverse pressure gradient, $\partial p/\partial x>0$, may lead to separation. This can be seen directly from the Navier–Stokes equations, see Appendix A, which applied at the wall, where the velocity is zero, reduces to:

$$\frac{\partial^2 u}{\partial y^2} = \frac{1}{\mu}\frac{\partial p}{\partial x} \tag{2.7}$$

The curvature of the u-velocity component at the wall is therefore given by the sign of the pressure gradient. Further, it is known that $\partial u/\partial y=0$ at $y=\delta$. From

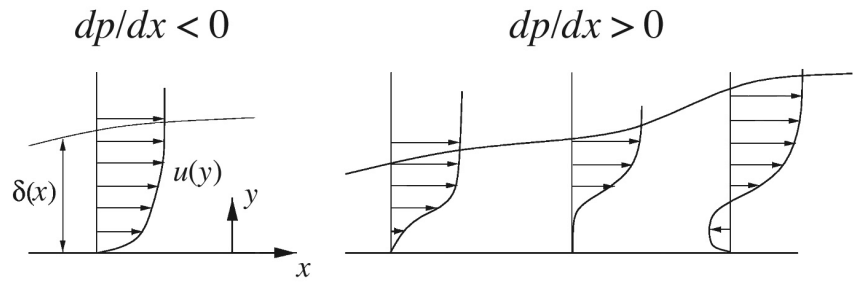

Figure 2.8 Schematic view of the shape of the boundary layer for a favourable and an adverse pressure gradient

this can be deduced that the u velocity profile in an adverse pressure gradient, $\partial p/\partial x > 0$, is S-shaped and separation may occur, whereas the curvature of the u velocity profile for $\partial p/\partial x < 0$ is negative throughout the entire boundary layer and the boundary layer stays attached. A schematic picture showing the different shapes of the boundary layer is found in Figure 2.8.

Since the form drag increases dramatically when the boundary layer separates, it is of utmost importance to the performance of an airfoil to control the pressure gradient.

For small values of x the flow is laminar, but for a certain x_{trans} the laminar boundary layer becomes unstable and a transition from laminar to turbulent flow occurs. At x_T the flow is fully turbulent. The transition from a laminar to a turbulent boundary layer is sketched in Figure 2.9.

The transitional process is very complex and not yet fully understood, but a description of the phenomenon is found in White (1991) where some engineering tools to predict x_{trans} are also given. One of the models, which sometimes are used in airfoil computations, is called the Michel one-step method. The method predicts transition when:

$$\mathrm{Re}_\theta = 2.9\,\mathrm{Re}_x^{0.4} \tag{2.8}$$

where $\mathrm{Re}_\theta = U(x)\theta(x)/\nu$ and $\mathrm{Re}_x = U(x)x/\nu$. For a laminar airfoil (see later) the Michel method might be inadequate, and more advanced methods such as the e^9 method (see White, 1991) should be applied.

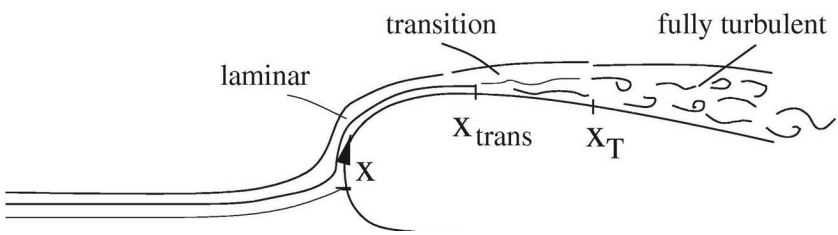

Figure 2.9 Schematic view of the transitional process

Turbulent flow is characterized by being more stable in regions of adverse pressure gradients $\partial p/\partial x > 0$ and by a steeper velocity gradient at the wall $\partial u/\partial y \mid_{y=0}$. The first property is good since it delays stall, but the second property increases the skin friction and thus the drag. These two phenomena are exploited in the design of high-performance airfoils termed laminar airfoils. A laminar airfoil is an airfoil where a large fraction of the boundary layer is laminar and attached in the range it is designed for. To design such an airfoil it is necessary to specify the maximum angle of attack, where the boundary layer to a large extent is supposed to be laminar. The airfoil is then constructed so that the velocity at the edge of the boundary layer $U(x)$ is constant after the acceleration past the leading edge and downstream. It is known from boundary layer theory (White, 1991; Schlichting, 1968) that the pressure gradient is expressed by the velocity outside the boundary layer as:

$$\frac{dp}{dx} = -\rho U(x)\frac{dU(x)}{dx} \tag{2.9}$$

At this angle the pressure gradient is therefore zero and no separation will occur. For smaller angles of attack the flow $U(x)$ will accelerate and dp/dx becomes negative, which again avoids separation and is stabilizing for the laminar boundary layer and thus delays transition. At some point x at the upper side of the airfoil it is, however, necessary to decelerate the flow in order to fulfil the Kutta condition, i.e. the pressure has to be unique at the trailing edge. If this deceleration is started at a position where the boundary layer is laminar, the boundary layer is likely to separate. Just after the laminar/turbulent transition, the boundary layer is relatively thin and the momentum close to the wall is relatively large and is therefore capable of withstanding a high positive pressure gradient without separation. During the continuous deceleration towards the trailing edge the ability of the boundary layer to withstand the positive pressure gradient diminishes and, to avoid separation, it is therefore necessary to decrease the deceleration towards the trailing edge. It is of utmost importance to ensure that the boundary layer is turbulent before decelerating $U(x)$. To ensure this, a turbulent transition can be triggered by placing a tripwire or tape before the point of deceleration. A laminar airfoil is thus characterized by a high value of the lift to drag ratio C_l/C_d below the design angle. But before choosing such an airfoil it is important to consider the stall characteristic and the roughness sensitivity. On an airplane it is necessary to fly with a high C_l at landing since the speed is relatively small. If the pilot exceeds $C_{l,\,max}$ and the airfoil stalls, it could be devastating if C_l drops as drastically with the angle of attack as on the FX38-153 in Figure 2.5. The airplane will then lose its lift and might crash. If the airfoil is sensitive to roughness, the good performance is lost if the wings are contaminated by dust, rain particles or insects, for example. On a wind turbine this could alter the performance with time if, for instance, the turbine is sited in an area with many insects. If a wind turbine is situated near the coast, salt might build up on the blades if the wind comes from the sea; and if the airfoils used are sensitive to roughness, the power output from the turbine will become dependent on

the direction of the wind. Fuglsang and Bak (2003) describe attempts to design airfoils specifically for use on wind turbines, where insensitivity to roughness is one of the design targets.

To compute the power output from a wind turbine it is necessary to have data of $C_l(\alpha, \mathrm{Re})$ and $C_d(\alpha, \mathrm{Re})$ for the airfoils applied along the blades. These data can be measured or computed using advanced numerical tools, but since the flow becomes unsteady and three-dimensional after stall, it is difficult to obtain reliable data for the high angles of attack. On a wind turbine very high angles of attack may exist locally, so it is often necessary to extrapolate the available data to high angles of attack.

References

Abbot, H. and von Doenhoff, A.E. (1959) *Theory of Wing Sections*, New York: Dover Publications.

Fuglsang, P. and Bak, C. (2003) 'Status of the Risø wind turbine airfoils', Presented at the European Wind Energy Conference, 16–19 June, EWEA, Madrid.

Prandtl, L. and Tietjens. O.G. (1957) *Applied Hydro and Aeromechanics*, New York: Dover Publications.

Schlichting, H. (1968) *Boundary-Layer Theory*, New York: McGraw-Hill.

White, F.M. (1991) *Viscous Fluid Flow*, New York: McGraw-Hill.

3 Three-dimensional aerodynamics

This chapter describes qualitatively the flow past a 3-D wing and how the spanwise lift distribution changes the upstream flow and thus the local angle of attack. It is based on basic vortex theory as described in various textbooks such as Milne-Thomson (1952). Since this theory is not directly used in the blade element momentum method derived later, it is only touched on very briefly here. This chapter may therefore be quite abstract for the reader with limited knowledge of vortex theory, but hopefully some of the basic results will be qualitatively understood.

A wing is a beam of finite length with airfoils as cross sections, and therefore a pressure difference between the lower and upper side is created, giving rise to the lift. At the tips are leakages, where air flows around the tips from the lower side to the upper side. The streamlines flowing over the wing will thus be deflected inwards and the streamlines flowing under the wing will be deflected outwards. Therefore, at the trailing edge there is a jump in the tangential velocity, see Figures 3.1 and 3.2.

A jump in the tangential velocity is seen, due to the leakage at the tips. Because of this jump there is a continuous sheet of streamwise vorticity in the wake behind a wing. This sheet is termed the trailing vortices.

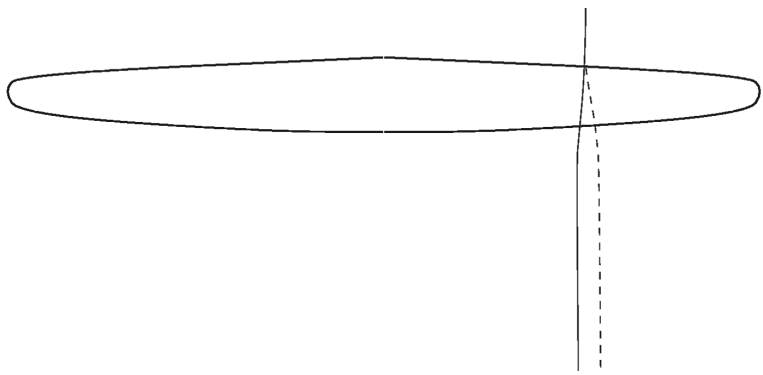

Figure 3.1 Streamlines flowing over and under a wing. The wing is seen from the suction side. The streamline flowing over the suction side (full line) is deflected inwards and the streamline flowing under (dashed line) is deflected outwards.

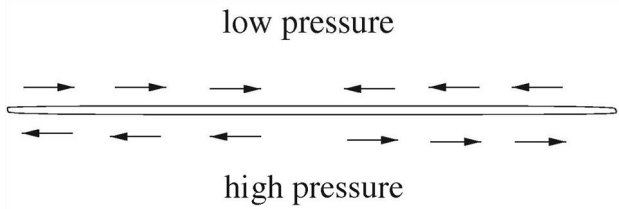

Figure 3.2 Velocity vectors seen from behind a wing

In classic literature on theoretical aerodynamics, such as Milne-Thomson (1952), it is shown that a vortex filament of strength, Γ, can model the flow past an airfoil for small angles of attack. This is because the flow for small angles of attack is mainly inviscid and governed by the linear Laplace equation, and it can be shown analytically that for this case the lift is given by the Kutta–Joukowski equation:

$$\mathbf{L} = \rho \mathbf{V}_{\infty} \times \Gamma \tag{3.1}$$

An airfoil may be thus be substituted by one vortex filament of strength Γ, and the lift produced by a 3-D wing can for small angles of attack be modelled by a series of vortex filaments oriented in the spanwise direction of the wing, known as the bound vortices. According to the Helmholtz theorem (see Milne-Thomson, 1952) a vortex filament, however, cannot terminate in the interior of the fluid but must either terminate on the boundary or be closed. A complete wing may be modelled by a series of vortex filaments, Γ_i, i =1, 2, 3, 4, ..., which are oriented as shown in Figure 3.3

In a real flow, the trailing vortices will curl up around the strong tip vortices and the vortex system will look more as shown in Figure 3.4.

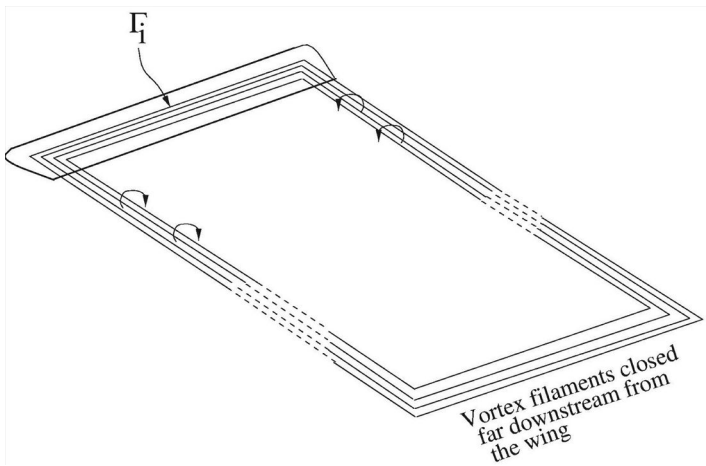

Figure 3.3 A simplified model of the vortex system on a wing

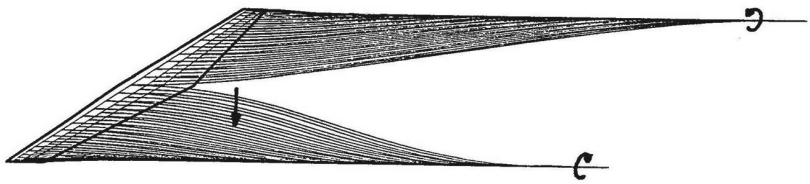

Figure 3.4 More realistic vortex system on a wing

The model based on discrete vortices, as shown in Figure 3.3, is called the lifting line theory; see Schlichting and Truckenbrodt (1959) for a complete description. The vortices on the wing (bound vortices) model the lift and the trailing vortices (free vortices) model the vortex sheet stemming from the three-dimensionality of the wing. The free vortices induce, by the Biot–Savart law, a downwards velocity component at any spanwise position of the wing. For one vortex filament of strength Γ the induced velocity at a point p is (see Figure 3.5).

$$\mathbf{w} = \frac{\Gamma}{4\pi}\oint \frac{\mathbf{r}\times\mathbf{ds}}{|\mathbf{r}|^3} \tag{3.2}$$

The total induced velocity from all vortices at a section of the wing is known as the downwash, and the local angle of attack at this section is therefore reduced by α_i, since the relative velocity is the vector sum of the wind speed $\mathbf{V}_\infty$ and the induced velocity $\mathbf{w}$, see Figure 3.6. α_g, α_i and α_e denote the geometric, the induced and the effective angle of attack, respectively. The effective angle of attack is thus

$$\alpha_e = \alpha_g - \alpha_i \tag{3.3}$$

In Figure 3.6 the induced velocity $\mathbf{w}$, the onset flow $\mathbf{V}_\infty$ and the effective velocity $\mathbf{V}_e$ is shown for a section on the wing together with the different angles

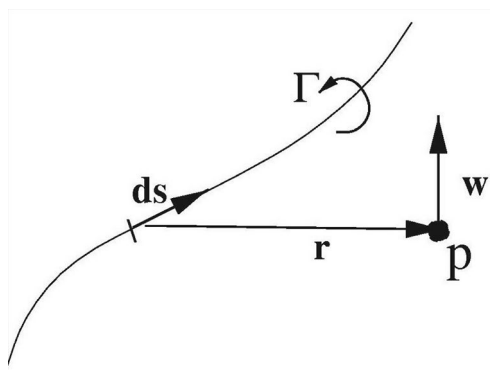

Figure 3.5 Induced velocity from a vortex line of strength

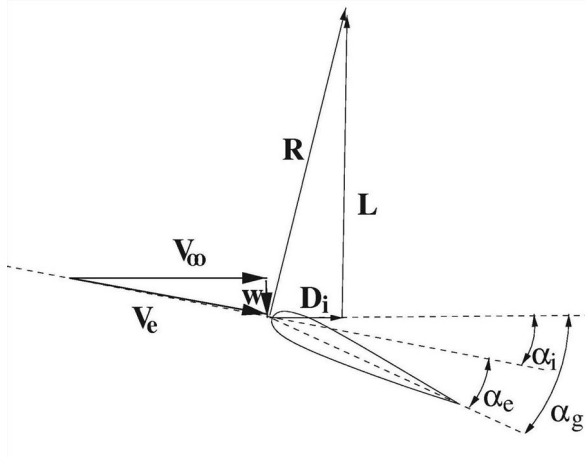

Figure 3.6 The effective angle of attack for a section in a wing and the resulting force **R**, the lift **L** and the induced drag $\mathbf{D}_i$

of attack α_g, α_i and α_e. It is assumed that Equation 3.1 is also valid for a section in a 3-D wing if the effective velocity is used. The local lift force **R**, which is perpendicular to the relative velocity, is also shown in Figure 3.6. The global lift is, however, by definition the force perpendicular to the onset flow $\mathbf{V}_\infty$, and the resulting force, **R**, is therefore decomposed into a component perpendicular to and a component in the direction of $\mathbf{V}_\infty$. The former component is thus the lift and the latter is a drag denoted the induced drag $\mathbf{D}_i$. At the tips of the wing the induced velocity obtains a value, which ensures zero lift.

An important conclusion is thus:

> *For a three-dimensional wing the lift is reduced compared to a two-dimensional wing at the same geometric angle of attack and the local lift has a component in the direction of the onset flow, which is denoted the induced drag. Both effects are due to the downwash induced by the vortex system of a 3-D wing.*

In the lifting line theory it is assumed that the three-dimensionality is limited to the downwash, i.e. the spanwise flow is still small compared to the streamwise velocity and 2-D data can therefore be used locally if the geometric angle of attack is modified by the downwash. This assumption is reasonable for long slender wings such as on a glider plane or a wind turbine. One method to determine the value of the vortices quantitatively, and thus the induced velocities, is Multhopp's solution of Prandtl's integral equation. This method is thoroughly described in Schlichting and Truckenbrodt (1959) and will not be shown here, but it is important to understand that the vortex system produced by a three-dimensional wing changes the local inflow conditions seen by the wing, i.e. although the flow is locally 2-D one cannot apply the geometric angle of attack when estimating the forces on the wing. This error was made in early propeller theory and the

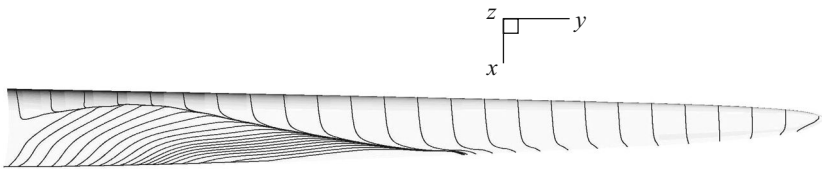

Figure 3.7 Computed limiting streamlines on a stall regulated wind turbine blade at a moderately high wind speed

discrepancy between measured and computed performance was believed to be caused by incorrect 2-D airfoil data. On a rotating blade Coriolis and centrifugal forces play an important role in separated boundary layers, i.e. after stall. In a separated boundary layer the velocity and thus the momentum is relatively small compared to the centrifugal force, which therefore starts to pump fluid in the spanwise direction towards the tip. When the fluid moves radially towards the tip, the Coriolis force points towards the trailing edge and acts as a favourable pressure gradient. The effect of the centrifugal and Coriolis force is to alter the 2-D airfoil data after stall. Whenever such data are needed, for example to compute the performance of a wind turbine at high wind speeds, much engineering skill and experience is needed to construct such post-stall data in order to obtain an acceptable result, see also Snel et al. (1993), and Chaviaropoulos and Hansen (2000).

Figure 3.7 shows the computed limiting streamlines on a modern wind turbine blade at a moderately high wind speed (see Hansen et al., 1997). Limiting streamlines are the flow pattern very close to the surface. Figure 3.7 shows that for this specific blade at a wind speed of 10m/s the flow is attached on the outer part of the blade and separated at the inner part, where the limiting streamlines have a spanwise component.

Vortex system behind a wind turbine

The rotor of a horizontal-axis wind turbine consists of a number of blades, which are shaped as wings. If a cut is made at a radial distance, r, from the rotational axis as shown in Figure 3.8, a cascade of airfoils is observed as shown in Figure 3.9.

The local angle of attack α is given by the pitch of the airfoil θ, the axial velocity and rotational velocity at the rotor plane, denoted respectively as V_a and V_{rot} (see Figure 3.9) as

$$\alpha = \phi - \theta, \tag{3.4}$$

where the flowangle ϕ is found as

$$\tan\phi = \frac{V_a}{V_{rot}}. \tag{3.5}$$

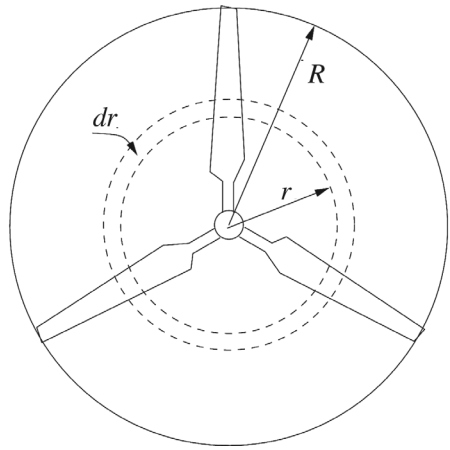

Figure 3.8 Rotor of a three-bladed wind turbine with rotor radius *R*

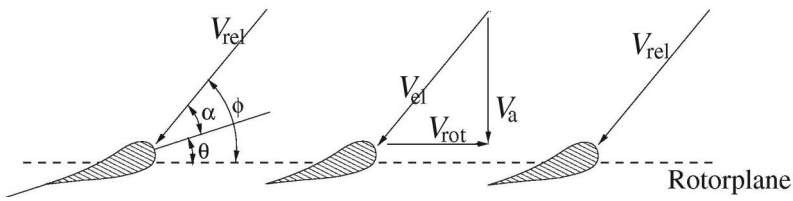

Figure 3.9 Radial cut in a wind turbine rotor showing airfoils at *r*/*R*

Since a horizontal-axis wind turbine consists of rotating blades, a vortex system similar to the linear translating wing must exist. The vortex sheet of the free vortices is oriented in a helical path behind the rotor. The strong tip vortices are located at the edge of the rotor wake and the root vortices lie mainly in a linear path along the axis of the rotor, see Figure 3.10.

The vortex system induces on a wind turbine an axial velocity component opposite the direction of the wind and a tangential velocity component opposite the rotation of the rotor blades. The induced velocity in the axial direction is specified through the axial induction factor a as aV_o, where V_o is the undisturbed wind speed. The induced tangential velocity in the rotor wake is specified through the tangential induction factor a' as $2a'\omega r$. Since the flow does not rotate upstream of the rotor, the tangential induced velocity in the rotor plane is thus approximately $a'\omega r$. ω denotes the angular velocity of the rotor and r is the radial distance from the rotational axis. If a and a' are known, a 2-D equivalent angle of attack could be found from Equations 3.4 and 3.5, where

$$V_a = (1-a)V_o, \tag{3.6}$$

(3.6)

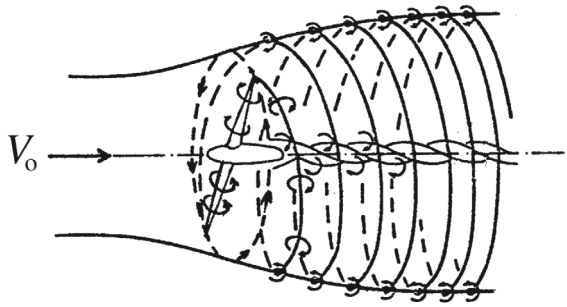

Figure 3.10 Schematic drawing of the vortex system behind a wind turbine (reproduced from Wilson and Lissaman (1974) with permission)

and

$$V_{rot} = (1 + a')\omega r. \tag{3.7}$$

Furthermore, if then also the lift and drag coefficients $C_l(\alpha)$ and $C_d(\alpha)$ are known for the airfoils applied along the blades, it is easy to compute the force distribution. Global loads such as the power output and the root-bending moments of the blades are found by integrating this distribution along the span. It is the purpose of the blade element momentum method, which will later be derived in detail, to compute the induction factors a and a' and thus the loads on a wind turbine. It is also possible to use a vortex method and construct the vortex system as shown in Figure 3.10 and use the Biot–Savart equation (3.2) to calculate the induced velocities. Such methods will, however, not be derived in this book, but can be found in, for example, Katz and Plotkin (2001) and Leishman (2006).

References

Chaviaropoulos, P.K. and Hansen, M.O.L. (2000) 'Investigating three-dimensional and rotational effects on wind turbine blades by means of a quasi-3D Navier–Stokes solver' *Journal of Fluids Engineering*, 122, pp 330–336.

Hansen, M.O.L., Sorensen, J.N., Michelsen, J.A. and Sorensen, N.N. (1997) 'A global Navier–Stokes rotor prediction model' AIAA 97-0970 paper presented at the 35th Aerospace Sciences Meeting and Exhibition, 6–9 January, Reno, NV.

Katz, J. and Plotkin, A. (2001) *Low-Speed Aerodynamics*, Cambridge: Cambridge University Press.

Leishmann, J.G. (2006) *Principles of Helicopter Aerodynamics*, Cambridge: Cambridge University Press.

Milne-Thomson, L.M. (1952) *Theoretical Aerodynamics*, London: Macmillan.

Schlichting, H. and Truckenbrodt, E. (1959) *Aerodynamik des Flugzeuges*, Berin: Springer-Verlag.

Snel, H., Houwink, B., Bosschers, J., Piers, W.J., van Bussel, G.J.W. and Bruining, A. (1993) 'Sectional prediction of 3-D effects for stalled flow on rotating blades and comparison with measurements', in *Proceedings ECWEC 1993*, Travemunde, March, pp 395–399.

Wilson, R.E. and Lissaman, P.B.S. (1974) *Applied Aerodynamics of Wind Power Machines*, Corvallis, OR: Oregon State University.

4 One-dimensional momentum theory for an ideal wind turbine

Before deriving the blade element momentum method it is useful to examine a simple one-dimensional (1-D) model for an ideal rotor. A wind turbine extracts mechanical energy from the kinetic energy of the wind. The rotor is in this simple 1-D model a permeable disc. The disc is considered ideal, i.e. it is frictionless and there is no rotational velocity component in the wake. The latter can be obtained by applying two contra rotating rotors or a stator. The rotor disc acts as a drag device slowing the wind speed down from V_o far upstream of the rotor to u at the rotorplane and to u_1 in the wake. Therefore the streamlines must diverge as shown in Figure 4.1. The drag is obtained by a pressure drop over the rotor. Close upstream of the rotor there is a small pressure rise from the atmospheric level p_o to p before a discontinuous pressure drop Δp over the rotor. Downstream of the rotor the pressure recovers continuously to the atmospheric level. The Mach number is small and the air density is thus constant and the axial velocity must decrease continuously from V_o to u_1. The behaviour of the pressure and axial velocity is shown graphically in Figure 4.1.

Due to the assumptions of an ideal rotor, it is possible to derive simple relationships between the velocities V_o, u_1, u, the thrust T and absorbed shaft power P. The thrust is the force in the streamwise direction, from the pressure drop over the rotor, and is used to reduce the wind speed from V_o to u_1:

$$T = \Delta p A, \tag{4.1}$$

where $A=\pi R^2$ is the area of the rotor. The flow is stationary, incompressible, frictionless and no external force acts on the fluid up- and downstream of the rotor. Therefore the Bernoulli equation (see Appendix A) is valid from far upstream to just in front of the rotor and from just behind the rotor to far downstream in the wake.

$$p_o + \tfrac{1}{2}\rho V_o^2 = p + \tfrac{1}{2}\rho u^2, \tag{4.2}$$

and

$$p - \Delta p + \tfrac{1}{2}\rho u^2 = p_o + \tfrac{1}{2}\rho u_1^2. \tag{4.3}$$

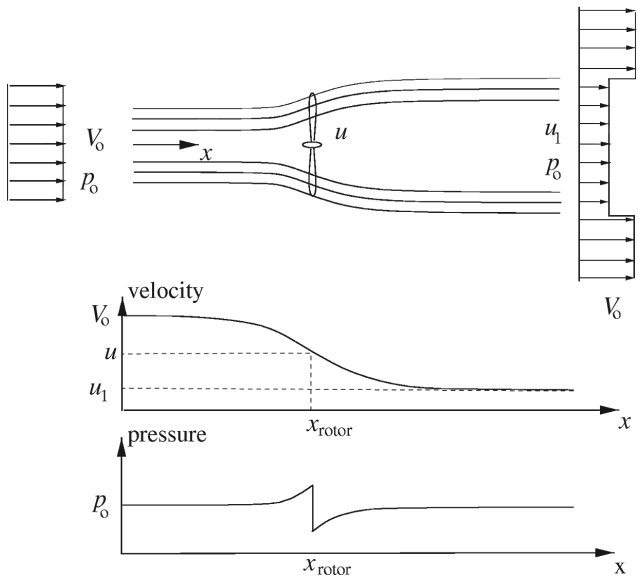

Figure 4.1 Streamlines past the rotor and the axial velocity and pressure up- and downstream of the rotor

Combining Equations 4.2 and 4.3 yields:

$$\Delta p = \tfrac{1}{2}\rho(V_o^2 - u_1^2). \tag{4.4}$$

The axial momentum equation on integral form (see Appendix A) is applied on the circular control volume with sectional area A_{cv} drawn with a dashed line in Figure 4.2 yielding

$$\frac{\partial}{\partial t}\iiint_{cv}\rho u(x,y,z)dxdydz + \iint_{cs} u(x,y,z)\rho\,\mathbf{V}\cdot\mathbf{dA} = F_{ext} + F_{pres}. \tag{4.5}$$

dA is a vector pointing outwards in the normal direction of an infinitesimal part of the control surface with a length equal to the area of this element. F_{pres} is the axial component of the pressure forces acting on the control volume. The first term in Equation 4.5 is zero since the flow is assumed stationary, and the last term is zero since the pressure has the same atmospheric value on the end planes and acts on an equal area. Further, on the lateral boundary of the control volume shown in Figure 4.2 the force from the pressure has no axial component.

Using the simplified assumptions of an ideal rotor, Equation 4.5 then yields:

$$\rho u_1^2 A_1 + \rho V_o^2(A_{cv} - A_1) + \dot{m}_{side}V_o - \rho V_o^2 A_{cv} = -T. \tag{4.6}$$

$\dot{m}_{side}$ can be found from the conservation of mass:

$$\rho A_1 u_1 + \rho(A_{cv} - A_1)V_o + \dot{m}_{side} = \rho A_{cv} V_{o,} \tag{4.7}$$

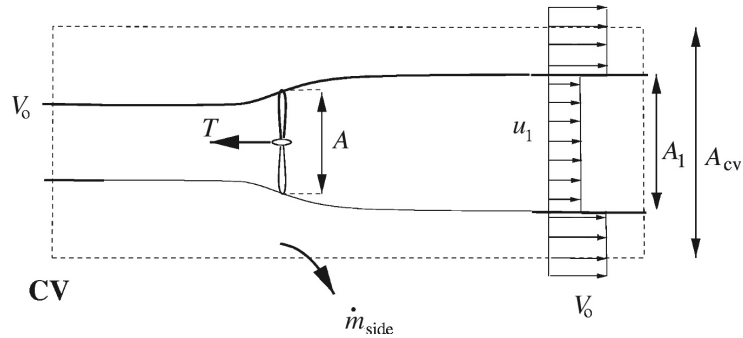

Figure 4.2 Circular control volume around a wind turbine

yielding:

$$\dot{m}_{side} = \rho A_1 (V_o - u_1). \tag{4.8}$$

The conservation of mass also gives a relationship between A and A_1 as:

$$\dot{m} = \rho u A = \rho u_1 A_1. \tag{4.9}$$

Combining Equations 4.8, 4.9 and 4.6 yields:

$$T = \rho u A (V_o - u_1) = \dot{m}(V_o - u_1). \tag{4.10}$$

If the thrust is replaced by the pressure drop over the rotor as in Equation 4.1 and the pressure drop from Equation 4.4 is used, an interesting observation is made:

$$u = \frac{1}{2}(V_o + u_1). \tag{4.11}$$

It is seen that the velocity in the rotor plane is the mean of the wind speed V_o and the final value in the wake u_1.

An alternative control volume to the one in Figure 4.2 can be made, see Figure 4.3.

The force from the pressure distribution along the lateral walls $F_{pres,\,lateral}$ of the control volume is unknown and thus also the net pressure contribution F_{pres}. On this alternative control volume there is no mass flow $\dot{m}_{side}$ through the lateral boundary, since this is aligned with the streamlines. The axial momentum Equation 4.5 therefore becomes:

$$T = \rho u A (V_o - u_1) + F_{pres} \tag{4.12}$$

Since the physical problem is the same, whether the control volume in Figure 4.2 or that in Figure 4.3 is applied, it can be seen by comparing Equations 4.10 and 4.12, that the net pressure force on the control volume following the streamlines is zero.

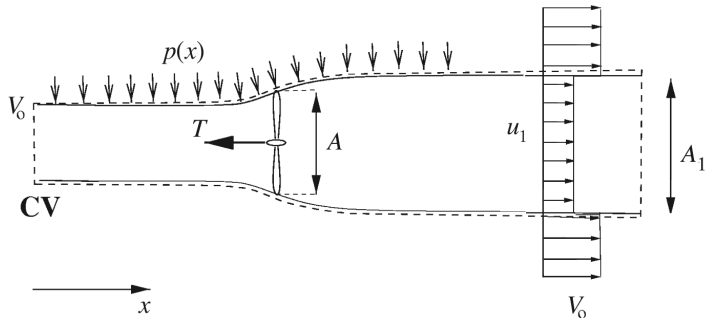

Figure 4.3 Alternative control volume around a wind turbine

The flow is assumed frictionless and there is therefore no change in the internal energy from the inlet to the outlet, and the shaft power P can be found using the integral energy equation on the control volume shown in Figure 4.3:

$$P = \dot{m}\left(\frac{1}{2}V_o^2 + \frac{p_o}{\rho} - \frac{1}{2}u_1^2 - \frac{p_o}{\rho}\right) \tag{4.13}$$

and since $\dot{m} = \rho \cdot u \cdot A$ the equation for P simply becomes:

$$P = \frac{1}{2}\rho u A(V_o^2 - u_1^2). \tag{4.14}$$

The axial induction factor a is defined as:

$$u = (1-a)V_o. \tag{4.15}$$

Combining Equation 4.15 with 4.11 gives:

$$u_1 = (1-2a)V_o, \tag{4.16}$$

which then can be introduced in Equation 4.14 for the power P and in Equation 4.10 for the thrust T, yielding:

$$P = 2\rho V_o^3 a(1-a)^2 A \tag{4.17}$$

and:

$$T = 2\rho V_o^2 a(1-a)A. \tag{4.18}$$

The available power in a cross section equal to the swept area A by the rotor is:

$$P_{avail} = \frac{1}{2}\rho A V_o^3. \tag{4.19}$$

The power P is often non-dimensionalized with respect to P_{avail} as a power coefficient C_p:

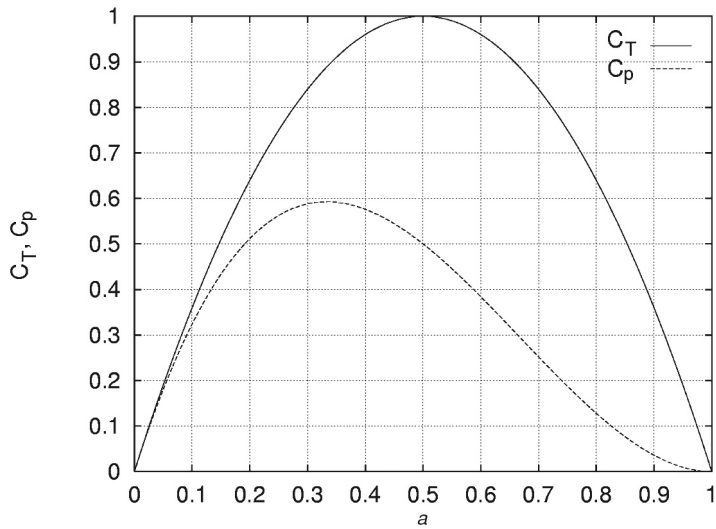

Figure 4.4 The power and thrust coefficients C_p and C_T as a function of the axial induction factor a for an ideal horizontal-axis wind turbine

$$C_p = \frac{P}{\frac{1}{2}\rho V_o^3 A}. \tag{4.20}$$

Similarly a thrust coefficient C_T is defined as:

$$C_T = \frac{T}{\frac{1}{2}\rho V_o^2 A}. \tag{4.21}$$

Using Equations 4.17 and 4.18 the power and thrust coefficients may for the ideal 1-D wind turbine be written as:

$$C_p = 4a(1-a)^2 \tag{4.22}$$

and:

$$C_T = 4a(1-a). \tag{4.23}$$

Differentiating C_p with respect to a yields:

$$\frac{dC_p}{da} = 4(1-a)(1-3a). \tag{4.24}$$

It is easily seen that $C_{p,max}=16/27$ for $a=1/3$. Equations 4.23 and 4.24 are shown graphically in Figure 4.4. This theoretical maximum for an ideal wind turbine is known as the Betz limit.

Experiments have shown that the assumptions of an ideal wind turbine leading to Equation 4.23 are only valid for an axial induction factor, a, less than approximately 0.3–0.4. This is seen in Figure 4.5 showing measurements of C_T as a function of a for different rotor states. If the momentum theory were valid for

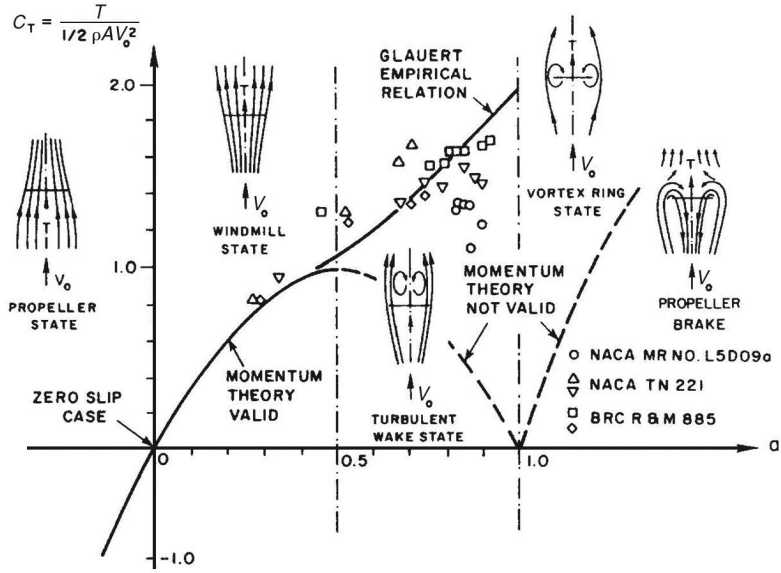

Figure 4.5 The measured thrust coefficient C_T as a function of the axial induction factor a and the corresponding rotor states (reproduced from Eggleston and Stoddard (1987) with permission)

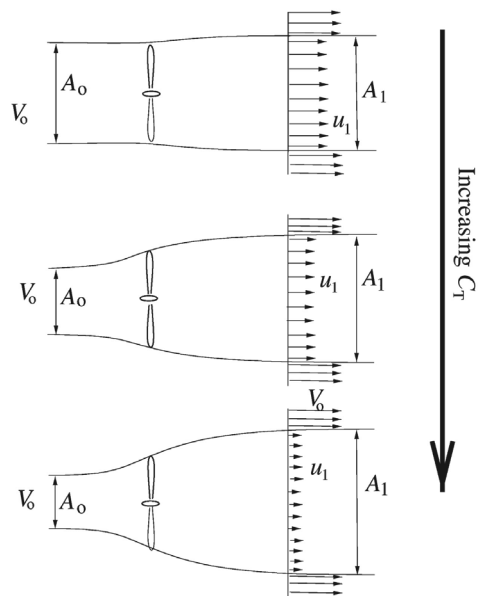

Figure 4.6 The expansion of the wake and the velocity jump in the wake for the 1-D model of an ideal wind turbine

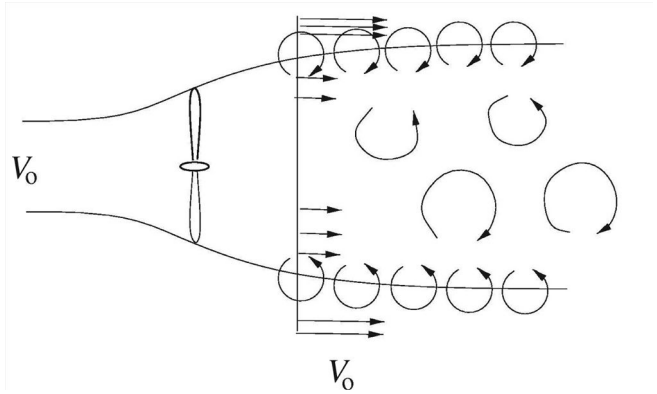

Figure 4.7 Schematic view of the turbulent-wake state induced by the unstable shear flow at the edge of the wake

higher values of a, the velocity in the wake would become negative as can readily be seen by Equation 4.16.

As C_T increases, the expansion of the wake increases and thus the velocity jump from V_o to u_1 in the wake, see Figure 4.6.

The ratio between the areas A_o and A_1 in Figure 4.6 can be found directly from the continuity equation as:

$$\frac{A_o}{A_1} = 1 - 2a. \tag{4.25}$$

A high thrust coefficient C_T and thus a high axial induction factor a is for a wind turbine present at low wind speeds. The reason that the simple momentum theory is not valid for a greater than approximately 0.3–0.4 is that the free shear layer at the edge of the wake becomes unstable when the velocity jump $V_o - u_1$ becomes too high and eddies are formed, which transport momentum from the outer flow into the wake. This situation is called the turbulent-wake state, see Figures 4.5 and 4.7.

Effects of rotation (Glauert optimum rotor)

The following section concerns with some effects of wake rotation and the theory of an optimum rotor as described by Glauert (1935). For the ideal rotor there is no rotation in the wake, i.e. a' is zero. Since a modern wind turbine consists of a single rotor without a stator the wake will possess some rotation as can be seen directly from Euler's turbine equation (see Appendix A) applied to an infinitesimal control volume of thickness dr, as shown in Figure 3.8:

$$dP = \dot{m}\omega r C_\theta = 2\pi r^2 \rho u \omega C_\theta dr, \tag{4.26}$$

where C_θ is the azimuthal component of the absolute velocity $C=(C_r, C_\theta, C_a)$ after the rotor and u the axial velocity through the rotor.

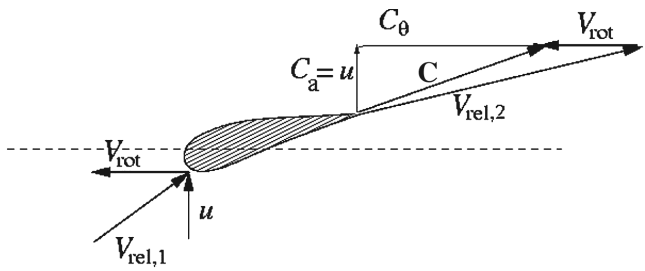

Figure 4.8 The velocity triangle for a section of the rotor

Since the forces felt by the wind turbine blades are also felt by the incoming air, but with opposite sign, the air will in the case of wind turbine rotate in the opposite direction of the blades. This can also be illustrated using Figure 4.8, where the relative velocity upstream of the blade $V_{rel,1}$ is given by the axial velocity u and the rotational velocity V_{rot}. For moderate angles of attack the relative velocity $V_{rel,2}$ downstream of the rotor approximately follows the trailing edge. The axial component, C_a, of the absolute velocity equals u due to conservation of mass and the rotational speed is unaltered. The velocity triangle downstream of the blade is now fixed and in Figure 4.8 is seen that the absolute velocity downstream of the blade, **C**, has a tangential component C_θ in the opposite direction of the blade.

From Equation 4.26 it is seen that for a given power P and wind speed the azimuthal velocity component in the wake C_θ decreases with increasing rotational speed ω of the rotor. From an efficiency point of view it is therefore desirable to have a high rotational speed of the wind turbine to minimize the loss of kinetic energy contained in the rotating wake. If we recall that the axial velocity through the rotor is given by the axial induction factor a as Equation 4.15 and that the rotational speed in the wake is given by a' as:

$$C_\theta = 2a'\omega r. \tag{4.27}$$

Equation (4.26) may then be written as:

$$dP = 4\pi\rho\omega^2 V_o a'(1-a)r^3 dr. \tag{4.28}$$

The total power is found by integrating dP from 0 to R as:

$$P = 4\pi\rho\omega^2 V_o \int_0^R a'(1-a)r^3 dr \tag{4.29}$$

or in non-dimensional form as:

$$C_p = \frac{8}{\lambda^2}\int_0^\lambda a'(1-a)x^3 dx, \tag{4.30}$$

where $\lambda = \omega R/V_o$ is the tip speed ratio and $x = \omega r/V_o$ is the local rotational speed at the radius r non-dimensionalized with respect to the wind speed V_o. It is clear from Equations 4.29 and 4.30 that in order to optimize the power it is necessary to maximize the expression:

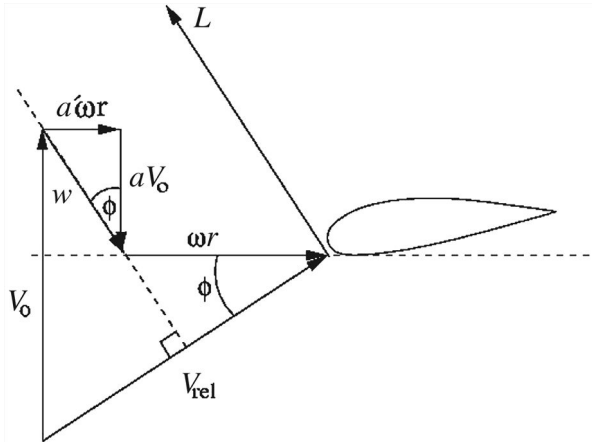

Figure 4.9 Velocity triangle showing the induced velocities for a section of the blade; note that for small angles of attack the total induced velocity w is perpendicular to the relative velocity seen by the section

$$f(a,a') = a'(1-a) \tag{4.31}$$

If the local angles of attack are below stall a and a' are not independent since the reacting force according to potential flow theory is perpendicular to the local velocity seen by the blade as indicated by Equation 3.1. The total induced velocity, **w**, must be in the same direction as the force and thus also be perpendicular to the local velocity. Employing this following relationship exists between a and a':

$$x^2 a'(1+a') = a(1-a). \tag{4.32}$$

Equation 4.32 is directly derived from Figure 4.9 since:

$$\tan\phi = \frac{a'\omega r}{aV_o} \tag{4.33}$$

and

$$\tan\phi = \frac{(1-a)V_o}{(1+a')\omega r}. \tag{4.34}$$

$x=\omega r/V_o$ denotes the ratio between the local rotational speed and the wind speed.

For local angles of attack below stall a and a' are related through Equation 4.32 and the optimization problem is thus to maximize Equation 4.31 and still satisfy Equation 4.32. Since a' is a function of a, the expression (4.31) is maximum when $df/da=0$ yielding:

$$\frac{df}{da} = (1-a)\frac{da'}{da} - a' = 0, \tag{4.35}$$

Table 4.1 The numerical relationships between a, a' and x

a	a'	x
0.26	5.5	0.073
0.27	2.375	0.157
0.28	1.333	0.255
0.29	0.812	0.374
0.30	0.500	0.529
0.31	0.292	0.753
0.32	0.143	1.15
0.33	0.031	2.63
0.333	0.00301	8.58

Table 4.2 Glauert's comparison of the computed optimum power coefficient including wake rotation with the Betz limit

$\lambda = \omega R/Vo$	$27Cp/16$
0.5	0.486
1.0	0.703
1.5	0.811
2.0	0.865
2.5	0.899
5.0	0.963
7.5	0.983
10.0	0.987

which can be simplified to:

$$(1-a)\frac{da'}{da} = a'. \tag{4.36}$$

Equation 4.32 differentiated with respect to a yields:

$$(1+2a')\frac{da'}{da}x^2 = 1-2a. \tag{4.37}$$

If Equations 4.36 and 4.37 are combined with Equation 4.32 the optimum relationship between a and a' becomes:

$$a' = \frac{1-3a}{4a-1}. \tag{4.38}$$

A table between a, a' and x can now be computed. a' is given by Equation 4.38 for a specified a and then x is found using Equation 4.32.

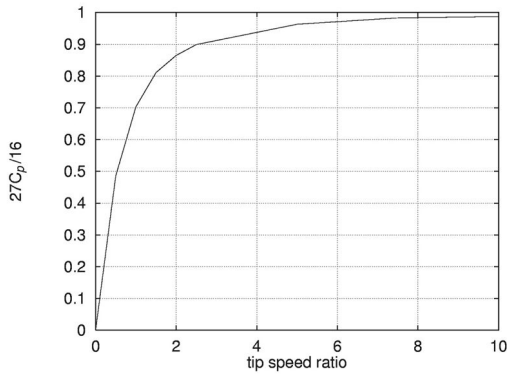

Figure 4.10 The efficiency of an optimum turbine with rotation. The efficiency is defined as the ratio between C_p including wake rotation and the Betz limit $C_{p,\,Betz}$=16/27

It is seen that as the rotational speed ω and thus also $x=\omega r/V_o$ is increased, the optimum value for a tends to 1/3, which is consistent with the simple momentum theory for an ideal rotor. Using the values from the table, the optimum power coefficient C_p is found by integrating Equation 4.30. This was done by Glauert (1935) for different tip speed ratios $\lambda=\omega R/V_o$. Glauert compared this computed optimum power coefficient with the Betz limit of 16/27, which is derived for zero rotation in the wake $a'=0$ – see Table 4.2. In Figure 4.10, Table 4.2 is plotted and it can be seen that the loss due to rotation is small for tip speed ratios greater than approximately 6.

It should be noted that some assumptions are made deriving the so-called Glauert optimum rotor. If the wake rotation becomes high, extra suction will be created behind the turbine since a radial pressure gradient is needed to maintain the curved streamlines so that the pressure becomes lower as the radial distance becomes smaller. This lower pressure at the centre behind the disc creates an extra massflow through the disc which is not accounted for when using the momentum equation, where the pressure is assumed constant. Further, the pressure can become so low that there is a risk of a vortex breakdown in the wake. Burton and colleagues (2001) argue that a=1/3 for all tip speed ratios and that the maximum C_p is 16/27 independent of the tip speed ratio.

References

Burton, T., Sharpe, D., Jenkins, N. and Bossanyi, E. (2001) *Wind Energy Handbook*, Chichester: Wiley.

Eggleston, D.M. and Stoddard, F.S. (1987) *Wind Turbine Engineering Design*, New York: Van Nostrand Reinhold Company.

Glauert, H. (1935) 'Airplane propellers', in W.F. Durand (ed.) *Aerodynamic Theory*, vol. 4, pp. 169–360, New York: Springer.

5 Shrouded rotors

It is possible to exceed the Betz limit by placing the wind turbine in a diffuser. If the cross section of the diffuser is shaped as an airfoil a lift force will be generated by the flow through the diffuser as seen in Figure 5.1.

As shown in de Vries (1979), the effect of this lift is to create a ring vortex, which by the Biot–Savart law will induce a velocity to increase the mass flow through the rotor. The axial velocity in the rotor plane is denoted V_2 and ε is the augmentation defined as the ratio between V_2 and the wind speed V_o, i.e. $\varepsilon = V_2/V_o$. A 1-D analysis of a rotor in a diffuser gives following expression for the power coefficient:

$$C_{p,d} = \frac{P}{\frac{1}{2}\rho V_o^3 A} = \frac{T \cdot V_2}{\frac{1}{2}\rho V_o^2 \frac{V_o}{V_2} V_2 A} = C_T \varepsilon. \tag{5.1}$$

For an ideal bare turbine Equations 4.22 and 4.23 are valid yielding:

$$C_{p,b} = C_T(1-a). \tag{5.2}$$

Combining the Equations 5.1 and 5.2 yields:

$$\frac{C_{p,d}}{C_{p,b}} = \frac{\varepsilon}{(1-a)}. \tag{5.3}$$

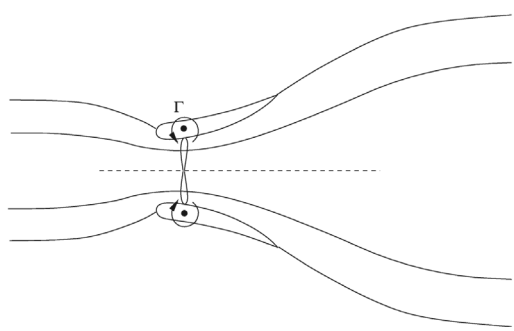

Figure 5.1 Ideal flow through a wind turbine in a diffuser

Further, the following equations are valid for the mass flow through a bare turbine $\dot{m}_b$ and the mass flow through a turbine in a diffuser $\dot{m}_d$:

$$\frac{\dot{m}_b}{\rho V_o A} = \frac{\rho(1-a)V_o A}{\rho V_o A} = 1-a \tag{5.4}$$

$$\frac{\dot{m}_d}{\rho V_o A} = \frac{\rho V_2 A}{\rho V_o A} = \varepsilon. \tag{5.5}$$

Combining Equations 5.3, 5.4 and 5.5 yields:

$$\frac{C_{p,d}}{C_{p,b}} = \frac{\dot{m}_d}{\dot{m}_b}. \tag{5.6}$$

Equation 5.6 states that the relative increase in the power coefficient for a shrouded turbine is proportional to the ratio between the mass flow through the turbine in the diffuser and the same turbine without the diffuser. Equation 5.6 is verified by computational fluid dynamics (CFD) results as seen in Figure 5.2, where for a given geometry the computed mass flow ratio $\dot{m}_d / \dot{m}_b$ is plotted against the computed ratio $C_{p,d} / C_{p,b}$. The CFD analysis is done on a simple geometry, without boundary layer bleed slots such as suggested by Gilbert and Foreman (1983). The diffuser was modeled using 266,240 grid points with 96 points around the diffuser airfoil section; and a turbulence model was chosen, which is sensitive to adverse pressure gradients (see Hansen et al. 2000). The rotor was modeled by specifying a constant volume force at the position of the rotor.

To check this approach some initial computations were made without the diffuser and in Figure 5.3, showing the relationship between the thrust and power coefficients, it can be seen that this approach gave good results compared with the following theoretical expression, which can be derived from Equations 4.22 and 4.23

$$C_{p,b} = \frac{1}{2} C_T (1 + \sqrt{1 - C_T}). \tag{5.7}$$

In Figure 5.3 is also seen that computations with a wind turbine in a diffuser gave higher values for the power coefficient than the Betz limit for a bare turbine.

The results are dependent on the actual diffuser geometry, i.e. the amount of lift which can be generated by the diffuser. An adverse pressure gradient is present for the flow in the diffuser, and the boundary layer will separate if the ratio between the exit area and the area in the diffuser becomes too high. To increase the lift giving a higher mass flow through the turbine and thus a higher power output, any trick to help the boundary layer from not separating is allowed such as, for example, vortex generators or boundary bleed slots. The computations in Figure 5.3 and wind tunnel measurements of Gilbert and Foreman (1983) show that the Betz limit can be exceeded if a device increasing

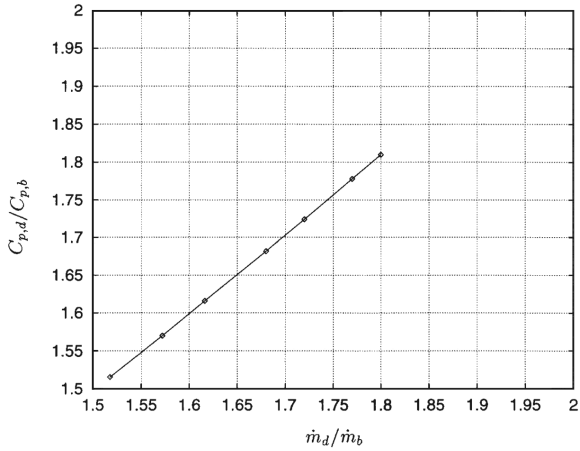

Figure 5.2 Computed mass flow ratio $\dot{m}_d / \dot{m}_b$ plotted against the computed ratio $C_{p,d} / C_{p,b}$

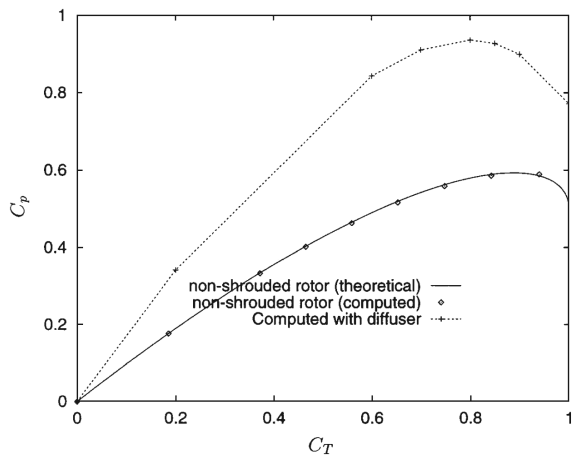

Figure 5.3 Computed power coefficient for a rotor in a diffuser as a function of the thrust coefficient C_T; further, the theoretical relationship Equation 5.7 for a bare rotor is also compared

the mass flow through the rotor is applied. But still this has to be proven on a full size machine. Further, the increased energy output has to be compared to the extra cost of building a diffuser and the supporting structure. Some more theoretical considerations on shrouded wind turbines can be found in Jamieson (2011).

References

Gilbert, B.L. and Foreman, K.M. (1983) 'Experiments with a diffuser-augmented model wind turbine', *Journal of Energy Resources Technology*, vol. 105, pp 46–53.

Hansen, M.O.L., Sorensen, N.N. and Flay, R.G.J. (2000) 'Effect of placing a diffuser around a wind turbine', *Wind Energy*, vol. 3, pp 207–213.

Jamieson, P. (2011) *Innovation in Wind Turbine Design*, Chichester: Wiley.

de Vries, O. (1979) *Fluid Dynamic Aspects of Wind Energy Conversion*, AGARDograph No. 243, Neuilly-sur-Seine: AGARD.

6 The classical blade element momentum method

All definitions and necessary theory have now been introduced to understand the blade element momentum method (BEM). In this chapter the classical BEM model from Glauert (1935) will be shown. With this model it is possible to calculate the steady loads and thus also the thrust and power for different settings of wind speed, rotational speed and pitch angle. To calculate time series of the loads for time-varying input some engineering models must be added, as will be shown in a later chapter. In the 1-D momentum theory the actual geometry of the rotor is not considered, i.e. the number of blades, the twist and chord distribution and the airfoils used. The blade element momentum method couples the momentum theory with the local events taking place at the actual blades. The streamtube introduced in the 1-D momentum theory is discretized into N annular elements of height, dr, as shown in Figure 6.1. The lateral boundary of these elements are streamlines, i.e. there is no flow across the elements.

In the BEM model the following is assumed for the annular elements:

1 No radial dependency, i.e. what happens at one element cannot be felt by the others.
2 The force from the blades on the flow is constant in each annular element. This corresponds to a rotor with an infinite number of blades.

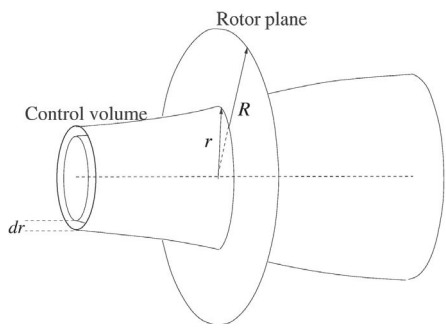

Figure 6.1 Control volume shaped as an annular element to be used in the BEM model

A correction, termed Prandtl's tip loss factor, is later introduced to correct for the latter assumption in order to compute a rotor with a finite number of blades.

In the previous section concerning the 1-D momentum theory it was proven that the pressure distribution along the curved streamlines enclosing the wake does not give an axial force component. Therefore it is assumed that this is also the case for the annular control volume shown in Figure 6.1. The thrust from the disc on this control volume can thus be found from the integral momentum equation since the cross section area of the control volume at the rotor plane is $2\pi r dr$:

$$dT = (V_o - u_1)d\dot{m} = 2\pi r\rho u(V_o - u_1)dr. \tag{6.1}$$

The torque dM on the annular element is found using the integral moment of momentum equation on the control volume (see Appendix A) and setting the rotational velocity upstream of the rotor to zero and to C_θ in the wake:

$$dM = rC_\theta d\dot{m} = 2\pi r^2 \rho u C_\theta dr. \tag{6.2}$$

This could also have been derived directly from Euler's turbine equation (Equation 4.26), since:

$$dP = \omega dM. \tag{6.3}$$

From the ideal rotor it was found that the axial velocity in the wake u_1 could be expressed by the axial induction factor a and the wind speed V_o as $u_1=(1-2a)V_o$ and if this is introduced to the Equations 6.1 and 6.2, together with the definitions for a and a' Equations 4.15 and 4.27, the thrust and torque can be computed as:

$$dT = 4\pi r\rho V_o^2 a(1-a)dr. \tag{6.4}$$

and:

$$dM = 4\pi r^3 \rho V_o \omega (1-a)a'dr. \tag{6.5}$$

The left-hand sides of Equations 6.4 and 6.5 are found from the local flow around the blade. It is recalled that the relative velocity V_{rel} seen by a section of the blade is a combination of the axial velocity $(1-a)V_o$ and the tangential velocity $(1+a')\omega r$ at the rotorplane, see Figure 6.2.

θ is the local pitch of the blade, i.e. the local angle between the chord and the plane of rotation. The local pitch is a combination of the pitch angle, θ_p, and the twist of the blade, β, as $\theta=\theta_p+\beta$, where the pitch angle is the angle between the tip chord and the rotorplane and the twist is measured relative to the tip chord. ϕ is the angle between the plane of rotation and the relative velocity V_{rel} and it is seen in Figure 6.2 that the local angle of attack is given by:

$$\alpha = \phi - \theta\ . \tag{6.6}$$

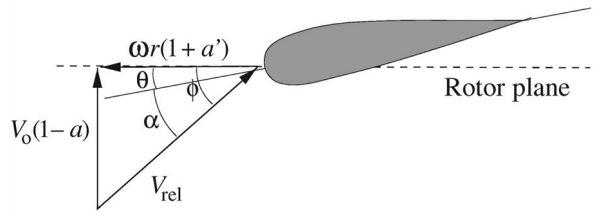

Figure 6.2 Velocities at the rotorplane

Further, it is seen that:

$$\tan\phi = \frac{(1-a)V_o}{(1+a')\omega r}. \tag{6.7}$$

It can be recalled from the chapter concerning 2-D aerodynamics that the lift by definition is perpendicular to the velocity seen by the airfoil, and the drag is parallel to the same velocity. In the case of a rotor this velocity is V_{rel} due to arguments given in the section about the vortex system of a wind turbine. Further, if the lift and drag coefficients C_l and C_d are known, the lift l and drag d force per length can be found from Equations 2.1 and 2.2 as:

$$l = \tfrac{1}{2}\rho V_{rel}^2 c C_l \tag{6.8}$$

and:

$$d = \tfrac{1}{2}\rho V_{rel}^2 c C_d \tag{6.9}$$

Since we are interested only in the force normal to and tangential to the rotorplane, the lift and drag are projected into these directions (see Figure 6.3):

$$p_N = l\cos\phi + d\sin\phi \tag{6.10}$$

and:

$$p_T = l\sin\phi - d\cos\phi \tag{6.11}$$

Equations 6.10 and 6.11 are normalized with respect to $\frac{1}{2}\rho V_{rel}^2 c$ yielding:

$$C_n = C_l\cos\phi + C_d\sin\phi \tag{6.12}$$

and:

$$C_t = C_l\sin\phi - C_d\cos\phi, \tag{6.13}$$

where,

$$C_n = \frac{p_N}{\frac{1}{2}\rho V_{rel}^2 c} \tag{6.14}$$

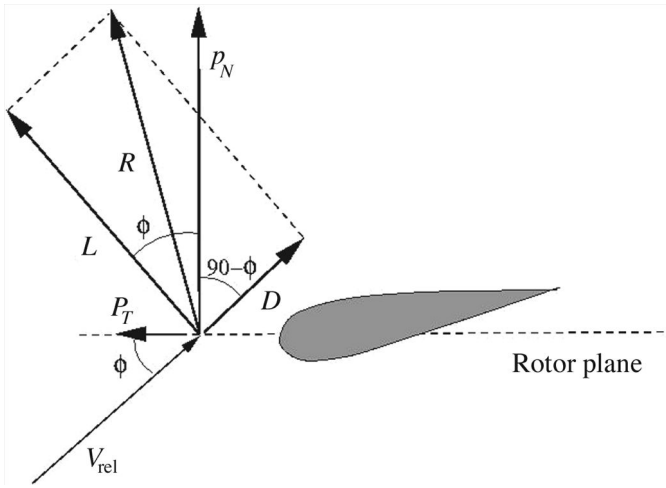

Figure 6.3 The local loads on a blade; **R** is the vector sum of the lift and the drag. p_N and p_T are the normal and tangential components of R, respectively

and:

$$C_t = \frac{p_T}{\frac{1}{2}\rho V_{rel}^2 c}. \tag{6.15}$$

From Figure 6.2 it is readily seen from the geometry that:

$$V_{rel}\sin\phi = V_o(1-a) \tag{6.16}$$

and:

$$V_{rel}\cos\phi = \omega r(1+a'). \tag{6.17}$$

Further, a solidity σ is defined as the fraction of the annular area in the control volume, which is covered by blades:

$$\sigma(r) = \frac{c(r)B}{2\pi r}. \tag{6.18}$$

B denotes the number of blades, $c(r)$ is the local chord and r is the radial position of the control volume.

The normal force and the torque on the control volume of thickness dr is since p_N and p_T are forces per length:

$$dT = Bp_N dr \tag{6.19}$$

and

$$dM = rBp_T dr. \tag{6.20}$$

Using Equation 6.14 for p_N and Equation 6.16 for V_{rel}, Equation 6.19 becomes

$$dT = \frac{1}{2}\rho B \frac{V_o^2(1-a)^2}{\sin^2\phi} c C_n dr. \tag{6.21}$$

Similarly if Equation 6.15 is used for p_T and Equations 6.16 and 6.17 are used for V_{rel}, Equation 6.20 becomes:

$$dM = \frac{1}{2}\rho B \frac{V_o(1-a)\omega r(1+a')}{\sin\phi\cos\phi} c C_t r dr. \tag{6.22}$$

If the two equations (6.21 and 6.4) for dT are equalized and the definition of the solidity equation (6.18) is applied an expression for the axial induction factor a is obtained:

$$a = \frac{1}{\frac{4\sin^2\phi}{\sigma C_n} + 1} \tag{6.23}$$

If Equations 6.22 and 6.5 are equalized, an equation for a' is derived:

$$a' = \frac{1}{\frac{4\sin\phi\cos\phi}{\sigma C_t} - 1} \tag{6.24}$$

Now all necessary equations for the BEM model have been derived and the algorithm can be summarized as the following eight steps. Since the different control volumes are assumed to be independent, each strip can be treated separately and the solution at one radius can be computed before solving for another radius, i.e. for each control volume the following algorithm is applied.

Step (1) Initialize a and a', typically a=a'=0

Step (2) Compute the flow angle ϕ using Equation 6.7

Step (3) Compute the local angle of attack using Equation 6.6

Step (4) Read $C_l(\alpha)$ and $C_d(\alpha)$ from table look-up

Step (5) Compute C_n and C_t from Equations 6.12 and 6.13

Step (6) Calculate a and a' from Equations 6.23 and 6.24

Step (7) If a and a' has changed more than a certain tolerance, go to Step (2) or else finish

Step (8) Compute the local loads on the segment of the blades

This is in principle the BEM method, but in order to get good results it is necessary to apply two corrections to the algorithm. The first is called Prandtl's tip loss factor, which corrects the assumption of an infinite number of blades.

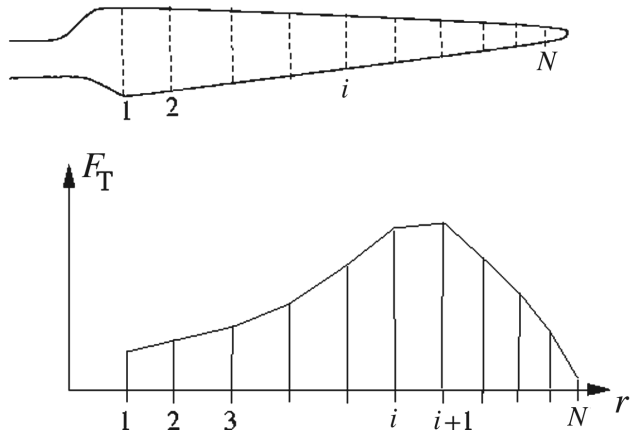

Figure 6.4 A linear variation of the load is assumed between two different radial positions r_i and r_{i+1}

The second correction is called the Glauert correction and is an empirical relation between the thrust coefficient C_T and the axial induction factor a for a greater than approximately 0.2–0.4, where the relation derived from the one-dimensional momentum theory is no longer valid. Each of these corrections will be treated in separate sections.

After having applied the BEM algorithm to all control volumes the tangential and normal load distribution is known and global parameters such as the mechanical power, thrust and root bending moments can be computed. One has, however, to be careful when integrating the tangential loads to give the shaft torque. The tangential force per length $p_{T,i}$ is known for each segment at radius r_i and a linear variation between r_i and r_{i+1} is assumed (see Figure 6.4). The load p_T between r_i and r_{i+1} is thus:

$$p_T = A_i r + B_i. \tag{6.25}$$

where:

$$A_i = \frac{p_{T,i+1} - p_{T,i}}{r_{i+1} - r_i} \tag{6.26}$$

and:

$$B_i = \frac{p_{T,i} r_{i+1} - p_{T,i+1} r_i}{r_{i+1} - r_i} \tag{6.27}$$

The torque dM for an infinitesimal part of the blade of length dr is:

$$dM = r p_T dr = (A_i r^2 + B_i r) dr \tag{6.28}$$

and the contribution $M_{i,i+1}$ to the total shaft torque from the linear tangential load variation between r_i and r_{i+1} is thus:

$$M_{i,i+1} = [\tfrac{1}{3}A_i r^3 + \tfrac{1}{2}B_i r^2]_{r_i}^{r_{i+1}} = \tfrac{1}{3}A_i(r_{i+1}^3 - r_i^3) + \tfrac{1}{2}B_i(r_{i+1}^2 - r_i^2) \tag{6.29}$$

The total shaft torque is the sum of all the contributions $M_{i,i+1}$ along one blade multiplied by the number of blades:

$$M_{tot} = B\sum_1^{N-1} M_{i,i+1} \tag{6.30}$$

Prandtl's tip loss factor

As already mentioned, Prandtl's tip loss factor corrects the assumption of an infinite number of blades. The vortex system in the wake is different for a rotor with a finite number of blades from a rotor with an infinite number of blades. The flow through the rotor is not axisymmetric and the ideal streamtube as indicated in Figure 6.1 does not exist and the use of the momentum equations becomes more complicated. However, Prandtl derived a correction factor F to the aerodynamic loads so that when the corrected loads are evenly distributed azimuthally and used in the momentum equations they give results for the induction at the blades very similar to what is found for the case with a finite number of blades. The result is that Equations 6.4 and 6.5 are modified with the correction factor F as:

$$dT = 4\pi r\rho V_o^2 a(1-a)F dr \tag{6.31}$$

and:

$$dM = 4\pi r^3 \rho V_o \omega (1-a)a' F dr \tag{6.32}$$

F is computed as:

$$F = \frac{2}{\pi}\cos^{-1}(e^{-f}), \tag{6.33}$$

where:

$$f = \frac{B}{2}\frac{R-r}{r\sin\phi}. \tag{6.34}$$

B is the number of blades, R is the total radius of the rotor, r is the local radius and ϕ is the flow angle. Using Equations 6.31 and 6.32 instead of Equations 6.4 and 6.5 in deriving the equations for a and a' yields:

$$a = \frac{1}{\frac{4F\sin^2\phi}{\sigma C_n} + 1} \tag{6.35}$$

and:

$$a' = \frac{1}{\frac{4F\sin\phi\cos\phi}{\sigma C_t} - 1}. \tag{6.36}$$

Equations 6.35 and 6.36 should be used instead of Equations 6.23 and 6.24 in Step 6 in the BEM algorithm, and an extra step computing Prandtl's tip loss factor F should be put in after Step 2. Deriving Prandtl's tip loss factor is very complicated and is not shown here, but a complete description can be found in Glauert (1935).

Glauert correction for high values of *a*

When the axial induction factor becomes larger than approximately 0.2–0.4, the simple momentum theory breaks down (see Figure 4.5), where the different states of the rotor also are shown. Different empirical relations between the thrust coefficient C_T can be made to fit with measurements, for example:

$$C_T = \begin{cases} 4a(1-a)F & a \le \frac{1}{3} \\ 4a(1-\frac{1}{4}(5-3a)a)F & a > \frac{1}{3} \end{cases} \tag{6.37}$$

or:

$$C_T = \begin{cases} 4a(1-a)F & a \le a_c \\ 4(a_c^2 + (1-2a_c)a)F & a > a_c \end{cases} \tag{6.38}$$

The last expression is found in Spera (1994), and a_c is approximately 0.2. F is Prandtl's tip loss factor and corrects the assumption of an infinite number of blades. In Figure 6.5 the two expressions for $C_T(a)$ are plotted for F=1 and compared to the simple momentum theory. Note that there is a difference at a=1/3 and the result of a design optimization may therefore depend on the choice of Glauert correction.

From the local aerodynamics the thrust dT on an annular element is given by Equation 6.21. For an annular control volume, C_T, is by definition:

$$C_T = \frac{dT}{\frac{1}{2}\rho V_o^2 2\pi r dr}. \tag{6.39}$$

If Equation 6.21 is used for dT, C_T becomes:

$$C_T = \frac{(1-a)^2\sigma C_n}{\sin^2\phi}. \tag{6.40}$$

This expression for C_T is now equated with the empirical expression in Equation 6.38.

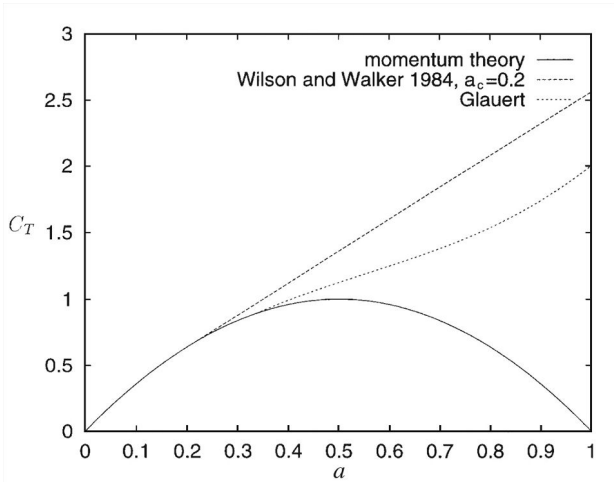

Figure 6.5 Different expressions for the thrust coefficient C_T versus the axial induction factor a.

If $a<a_c$:

$$4a(1-a)F = \frac{(1-a)^2 \sigma C_n}{\sin^2 \phi} \tag{6.41}$$

and this gives:

$$a = \frac{1}{\frac{4F\sin^2\phi}{\sigma C_n} + 1}, \tag{6.42}$$

which is the normal Equation 6.35.

If $a>a_c$:

$$4(a_c^2 + (1-2a_c)a)F = \frac{(1-a)^2 \sigma C_n}{\sin^2 \phi} \tag{6.43}$$

and this gives:

$$a = \frac{1}{2}\left[2 + K(1-2a_c) - \sqrt{(K(1-2a_c)+2)^2 + 4(Ka_c^2 - 1)}\right], \tag{6.44}$$

where:

$$K = \frac{4F\sin^2\phi}{\sigma C_n}. \tag{6.45}$$

In order to compute the induced velocities correctly for large values of the thrust coefficient, Equations 6.44 and 6.42 must replace Equation 6.35 from the simple momentum theory.

If one chooses to use the alternative Glauert correction Equation 6.37 instead of Equation 6.38 it is not possible to derive an explicit equation for a at high values of the thrust coefficient, but instead Equations 6.40 and 6.37 must be solved iteratively to find the value of a that satisfies both.

Annual energy production

The BEM method has now been derived and it is possible to compute a power curve, i.e. the shaft power as a function of the wind speed V_o. In order to compute the annual energy production it is necessary to combine this production curve with a probability density function for the wind. From this function the probability, $f(V_i < V_o < V_{i+1})$, that the wind speed lies between V_i and V_{i+1} can be computed. Multiplying this with the total number of hours per year gives the number of hours per year that the wind speed lies in the interval $V_i < V_o < V_{i+1}$. Multiplying this with the power (kW) produced by the wind turbine when the wind speed is between V_i and V_{i+1} gives the contribution of the total production (kWh) for this interval. The wind speed is discretized into N discrete values (V_i, i=1,N), typically with 1m/s difference (see Figure 6.6).

It must be noted that the production must be corrected for losses in the generator and gearbox, which have a combined efficiency of approximately 90 per cent. Typically the probability density function of the wind is given by either a Rayleigh or Weibull distribution. The Rayleigh distribution is given by the mean velocity $\overline{V}$ only as:

$$h_R(V_o) = \frac{\pi}{2}\frac{V_o}{\overline{V}^2}\exp\left(-\frac{\pi}{4}\left(\frac{V_o}{\overline{V}}\right)^2\right). \tag{6.46}$$

In the more general Weibull distribution some corrections for the local siting (landscape, vegetation, nearby houses, obstacles, etc.) can be modelled through a scaling factor A and a form factor k:

$$h_w(V_o) = \frac{k}{A}\left(\frac{V_o}{A}\right)^{k-1}\exp\left(-\left(\frac{V_o}{A}\right)^k\right). \tag{6.47}$$

The parameters k and A must be determined from local meteorological data, nearby obstacles and landscape. Of help in doing this is the *European Wind Atlas* (Troen and Petersen, 1989). From the Weibull distribution the probability $f(V_i < V_o < V_{i+1})$ that the wind speed lies between V_i and V_{i+1} is calculated as:

$$f(V_i < V_o < V_{i+1}) = \exp\left(-\left(\frac{V_i}{A}\right)^k\right) - \exp\left(-\left(\frac{V_{i+1}}{A}\right)^k\right). \tag{6.48}$$

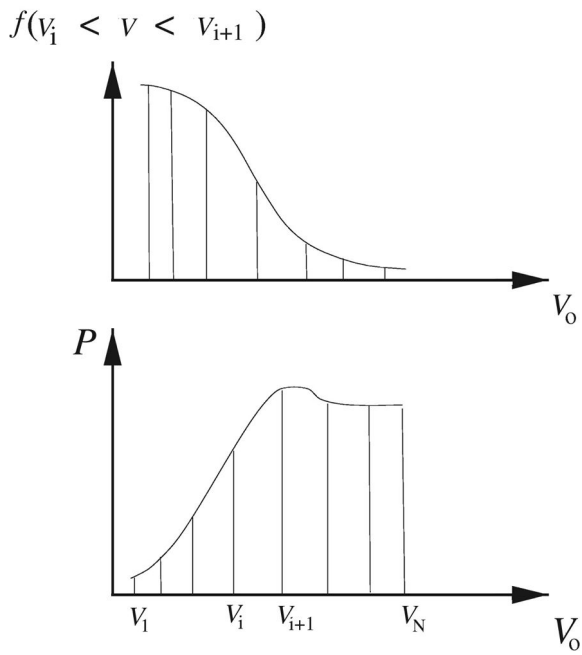

Figure 6.6 Probability $f(V_i < V_o < V_{i+1})$ that the wind speed lies between V_i and V_{i+1} and a power curve in order to compute the annual energy production for a specific turbine on a specific site

The total annual energy production (AEP) can thus be evaluated as:

$$AEP = \sum_{i=1}^{N-1} \tfrac{1}{2}(P(V_{i+1}) + P(V_i)) \cdot f(V_i < V_o < V_{i+1}) \cdot 8760. \tag{6.49}$$

Example

After having derived the BEM method and shown how the annual energy production can be calculated, it is time for a simple example to illustrate the accuracy that can be obtained for a real turbine. The following example is a Nordtank NTK 500/41 wind turbine. The turbine is stall-regulated, i.e. fixed pitch, and the main parameters are listed below:

- rotational speed of 27.1RPM;
- air density 1.225kg/m^3;
- rotor radius 20.5m;
- number of blades 3;
- hub height 35.0m;
- cut-in wind speed 4m/s and cut-out wind speed 25m/s.

Table 6.1 Blade description

r [m]	*twist [degrees]*	*chord [m]*
4.5	20.0	1.63
5.5	16.3	1.597
6.5	13.0	1.540
7.5	10.05	1.481
8.5	7.45	1.420
9.5	5.85	1.356
10.5	4.85	1.294
11.5	4.00	1.229
12.5	3.15	1.163
13.5	2.60	1.095
14.5	2.02	1.026
15.5	1.36	0.955
16.5	0.77	0.881
17.5	0.33	0.806
18.5	0.14	0.705
19.5	0.05	0.545
20.3	0.02	0.265

Since the power depends directly on the air density ρ, the computations must, according to the standards, be performed for ρ=1.225 kg/m^3. The difficult part is to find reliable data for the airfoil data $C_l(\alpha)$ and $C_d(\alpha)$ for the different airfoils applied along the span. The data available in the literature are for thin airfoils not much thicker than 20 per cent of the chord and for angles of attack only slightly above $C_{l,max}$. For structural reasons it is desirable to use very thick airfoils of approximately 40 per cent of the chord at the root of the blades in order to absorb the high bending moments. Further, the boundary layer on the rotating blades are influenced by centrifugal and Coriolis forces, which alter the post-stall lift and drag coefficients from what is measured in a wind tunnel. It is therefore clear that it requires significant engineering skill and experience to construct good airfoil data for thick airfoils at high angles of attack including 3-D effects. Some guidelines are given in Snel et al. (1993) and Chaviaropoulos and Hansen (2000) to correct for the rotational effects. When the power curve from an actual wind turbine is known from measurements, it is common to calibrate the airfoil data afterwards, in order to have a better agreement between measurements and computations. If a new blade is constructed which is not too different from blades where the airfoil data have been calibrated, it is possible to predict the power curve very well. But if a new blade is to be designed with completely new airfoils one has to be very careful in using the computed results. The actual geometry and airfoil data on the blade of the Nordtank NTK 500/41 is not shown here, but an experienced guess has been applied to extrapolate the data into high angles of attack. The power curve has been measured (Paulsen, 1995) and the comparison

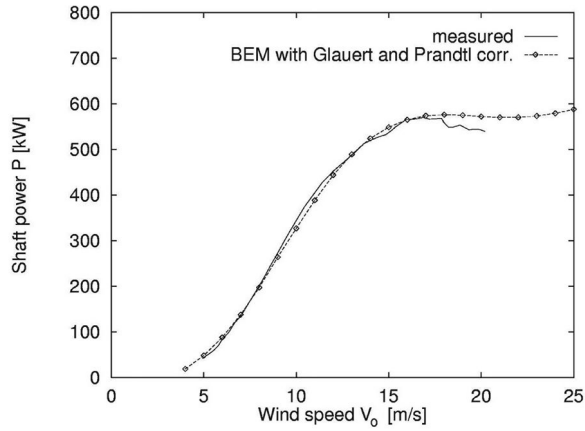

Figure 6.7 Comparison between computed and measured power curve, i.e. mechanical shaft power as function of the wind speed

between the computed and measured power curve is shown in Figure 6.7 in order to get an idea of the accuracy of the BEM model.

It is seen in Figure 6.7 that except for the very high wind speeds the BEM method captures the measurements very well. The power curve is often shown in non-dimensional form as in Figures 6.8 or 6.9. In Figure 6.8 is seen that this particular wind turbine has a maximum efficiency of approximately C_p=0.5 for a tip speed ratio λ between 9 and 10. The advantage of plotting the power coefficient as a function of the inverse tip speed ratio is that λ^{-1} increases linearly with the wind speed V_o.

If the turbine is erected at a site where the Weibull parameters are k=1.9 and A=6.8m/s, the annual energy output from the mechanical power would

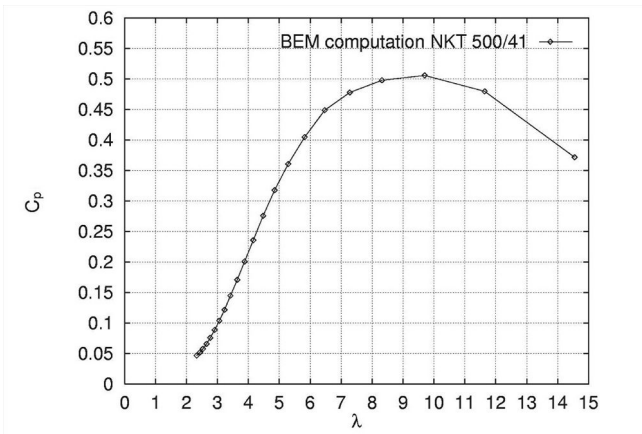

Figure 6.8 Power coefficient C_p as a function of the tip speed ratio $\lambda=\omega R/V_o$

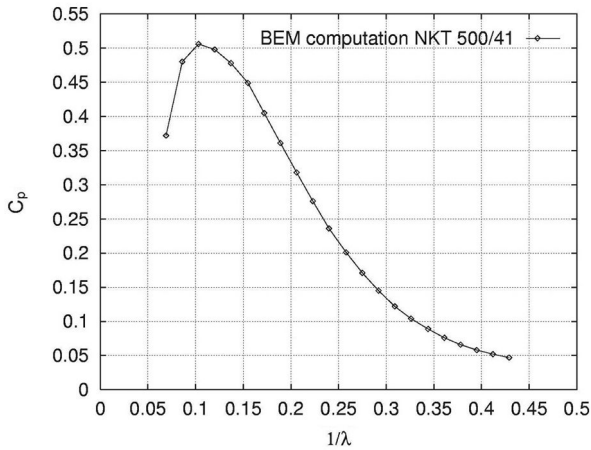

Figure 6.9 Power coefficient C_p as a function of the inverse tip speed ratio $\lambda^{-1} = V_o/wR$

be 1.09×10^6 kWh corresponding to the consumption of approximately 250 households. The real number is less, since the losses from the generator and gearbox have not been taken into account. It should also be remembered that the Weibull parameters vary from site to site and have to be evaluated for each individual siting. The example shown here is for a stall-regulated wind turbine, but the BEM method can also be used to predict the necessary pitch setting of a pitch-regulated wind turbine. When the pitch is mentioned for an entire wind turbine it is referred to as the angle between the chord line of the tip airfoil and the rotor plane. A pitch-regulated wind turbine may operate at a fixed pitch until a certain nominal power is generated. For higher wind speeds the blades are pitched normally with the leading edge into the wind in order to keep this nominal power. Therefore the power curve of a pitch-regulated wind turbine is absolutely flat after the nominal power has been reached. More runs are required with the BEM method to predict the power curve and the pitch setting for different wind speeds. One procedure for computing a pitch regulated wind turbine is sketched in Figure 6.10.

At point *A* the nominal power is reached and it is necessary to change the pitch. BEM calculations are made for a pitch of θ_2 and θ_3. It is seen that for a wind speed of $V_o(B)$ the pitch much be changed to θ_2 in order to obtain the nominal power. The BEM method as derived in this chapter is steady, so it is not possible to compute the transient from point *A* to point *B* and from point *B* to point C. This requires an extended BEM method as will be shown in Chapter 9. An alternative way of calculating the necessary pitch angle at the wind speed $V_o(B)$ would be to run the BEM method at a fixed wind speed and vary the pitch angle to determine the value of the pitch angle that exactly corresponds to the rated power.

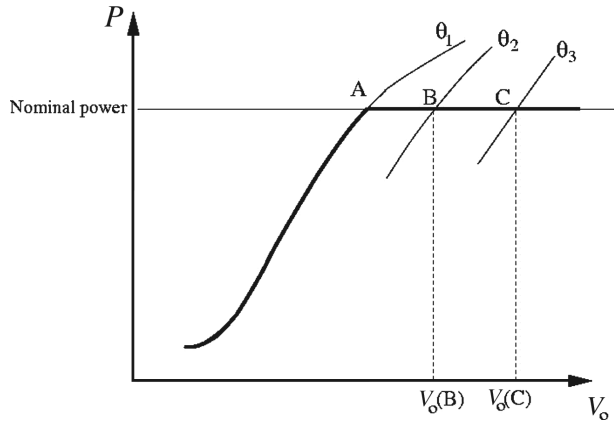

Figure 6.10 Power curve for a pitch controlled wind turbine

Simple test of BEM code

In the following is shown a very simple calculation that one can do to test the implementation of the BEM equations. Only one radial position is considered, r=24.5 [m], and constant airfoil data independent of the angle of attack is assumed.

R=31 [m]
B=3
ρ=1.225 [kg/m3]
V_o=8.0 [m/s]
ω=2.61 [rad/s]
θ_p=–3.d0 [degrees]
β=2.0 [degrees]
c=0.5 [m]
C_l=0.5 constant
C_d=0.01 constant

Results

r [m]	a	a'	p_T [N/m]	p_N [N/m]	F
24.500	0.088	0.001	59.353	632.918	0.981

Now the chord is changed to c=1 m

r [m]	a	a'	p_T	[N/m]	p_N [N/m]	F
24.500	0.19	0.002	101.149	1266.029	0.988	0.988

The chord is changed to c=1.5 m and the result now depends on the choice of Glauert correction.

Wilson&Walker equation (Equation 6.38)

r [m]	*a*	*a′*	p_T *[N/m]*	p_N *[N/m]*	*F*
24.500	0.329	0.003	120.756	1898.732	0.995

Equation 6.37

r [m]	*a*	*a′*	p_T *N/m]*	p_N *[N/m]*	*F*
24.500	0.370	0.003	111.099	1897.530	0.996

References

Chaviaropoulos, P.K. and Hansen, M.O.L. (2000) 'Investigating three-dimensional and rotational effects on wind turbine blades by means of a quasi-3D Navier–Stokes solver', *Journal of Fluids Engineering,* 122, pp 330–336.

Glauert, H. (1935) 'Airplane propellers', in W.F. Durand (ed.) *Aerodynamic Theory*, vol. 4, pp. 169–360, New York: Springer.

Paulsen, U.S. (1995) *Konceptundersøgelse Nordtank NTK 500/41 Strukturelle laster* Risø-I-936(DA), (in Danish). Roskilde: Risø National Laboratory.

Snel, H., Houwink, B., Bosschers, J., Piers, W.J., van Bussel, G.J.W. and Bruining, A. (1993) 'Sectional prediction of 3-D effects for stalled flow on rotating blades and comparison with measurements', in *Proceedings ECWEC 1993,* 8–10 March, Travemunde, pp. 395–399. London: James and James.

Spera, D.A. (1994) *Wind Turbine Technology*, New York: ASME Press.

Troen, I. and Petersen, E.L. (1989) *European Wind Atlas*, Roskilde: Risø National Laboratory.

7 Control/regulation and safety systems

The control or regulation system ensures that the turbine operates within the design range, that is either it

- keeps the rotational speed within a certain range;
- yaws the turbine;
- keeps the power output within a certain range;
- starts and stops the turbine.

Further, the control system can ensure a smooth power output $P(t)$ and/or may optimise the power output at lower wind speeds. To limit the power at high wind speeds the following four strategies may be used, where the three first are by far the most common and often the second and third are combined and then termed variable-speed pitch regulation (VSPR):

1 stall regulation
2 pitch regulation
3 torque regulation
4 yaw control.

Stall regulation

Stall regulation is mechanically the most simple, since the blades are fixed to the hub and cannot afterwards be pitched. A stall-regulated wind turbine is normally operated at an almost constant rotational speed and thus the angle of attack increases as the wind speed increases, see Figure 6.2. Eventually, as the local angles of attack are increased, the blades stall, causing the lift to decrease and the drag to increase, yielding a lower tangential load according to Equation 6.13. The power limitation depends on the pitch angle (angle between rotor plane and tip chord), the twist and chord distributions and the airfoils used for the blades. If a site test shows that the power is not limited sufficiently, it is necessary to unbolt the blades and change the fixed pitch setting of the blades. On a stall-regulated wind turbine an asynchronous generator is often used where the rotational speed is almost constant and determined by the torque characteristic of the generator,

i.e. the shaft torque of the generator, M_G, as a function of the rotational speed of the shaft n. A typical torque characteristic is shown in Figure 7.1, where it can be seen that the asynchronous generator can act both as a motor and as a generator. The sign is here chosen to be positive when the generator is producing electricity. The rotational speed of the generator will be between n_o and n_{nom} and the torque will equal the torque produced by the rotor blades M_R at the generator shaft. The rotational speed of the generator, for zero shaft torque, n_o, is for an asynchronous generator

$$n_o = 60 f_{grid} / p, \tag{7.1}$$

where f_{grid} is the frequency of the grid (in Europe 50Hz) and p denotes the number of pole pairs. n_o is thus 1500RPM for four poles and 1000RPM for six poles. The rotational speed of the generator is higher than the rotational speed of the rotor and therefore a gearbox exists between the generator and the rotor. The relationship between the rotational speed of the rotor, ω, and the rotational speed of the generator, n, is given through the transmission factor r as $\omega = n/r$. The relative difference between the actual rotational speed n and n_o is called the slip, $SL = (n - n_o)/n_o$, and for a normal stall-regulated wind turbine the slip is about 1–3 per cent. This means that the rotational speed of the rotor is almost constant and the possibility of using the rotor as a flywheel to store energy from, for example, a gust is small. Changes in the rotor torque M_R from, for example, turbulence in the wind is thus almost immediately transferred to the generator torque M_G and thus to the produced electrical power $P_{EL} = M_G \, 2\pi n/60$. Consider a wind turbine operating at point A on Figure 7.1 and that the wind speed increases. Then the torque, M_R, from the rotor blades increases and the rotor accelerates according to equation (7.2)

$$I \frac{d\omega}{dt} = M_R - M_G, \tag{7.2}$$

until M_G again equals M_R at point B. I denotes the moment of inertia of the rotor about the rotational axis and here M_R and M_G are the rotor and generator torque at the rotor shaft.

If the generator is disconnected from the grid, the term $M_R - M_G$ on the right hand side of Equation 7.2 is always positive and the rotor will start to accelerate and the rotational speed can become so high that a risk of breakdown exists. The safety system must detect this and ensure that the rotor is stopped. On a stall-regulated wind turbine it is common that the outer part of the blades are activated by the centrifugal force to turn 90° and thus act as an aerodynamic brake limiting M_R (see Figure 7.2).

An example of a time history of a start-up at a high wind speed for a stallregulated wind turbine is shown in Figure 7.3. This figure shows actual measurements performed on the Elkraft 1MW demonstration wind turbine, which was sited near Copenhagen. This turbine could run as a stall-regulated machine as well as a pitch-regulated machine. The first curve in Figure 7.3 shows the wind speed at hub height,

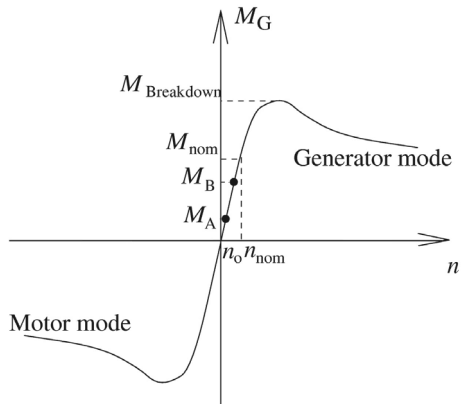

Figure 7.1 A typical torque characteristic for an asynchronous generator

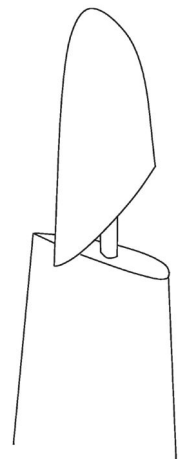

Figure 7.2 Turnable tip used as an aerodynamic brake and activated by the centrifugal force

the second curve shows the rotational speed of the generator, n, and the last curve shows the corresponding power as a function of time. When starting the turbine, at t=420s, the generator is switched off, i.e. M_G is zero and the rotor starts to accelerate until n=n_o at t=445s. Then the generator is connected instantaneously, giving rise to an overshoot in the power, as seen directly in the power time history.

Pitch regulation (constant rotational speed)

On a pitch-regulated machine it is possible to actively pitch the entire blade and thus to change simultaneously the angles of attack along the blade. One way of controlling the pitch is sketched in Figure 7.4, where a piston placed within the

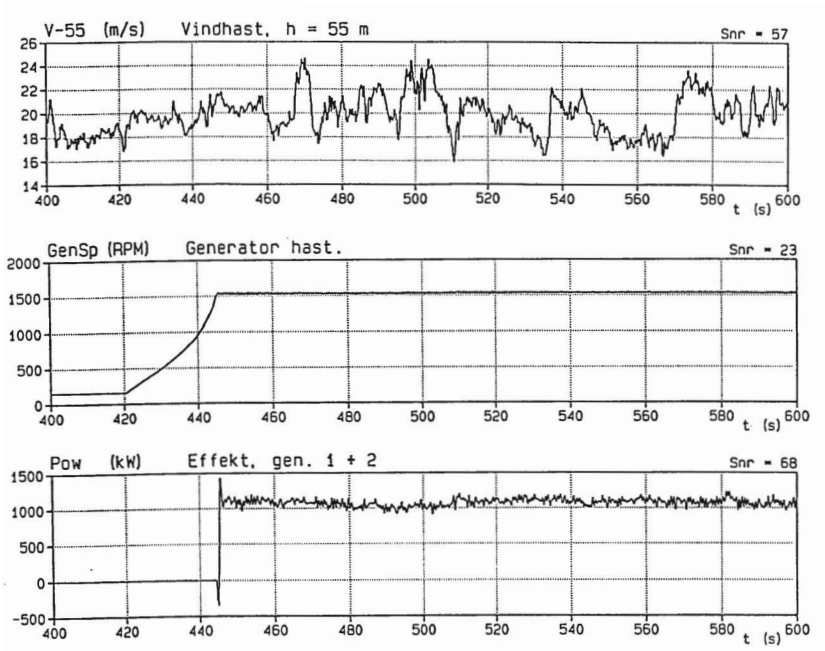

Figure 7.3 Starting a stall-regulated wind turbine at high wind speed, Elkraft 1MW demonstration wind turbine at Avedøre, Denmark

main shaft changes the pitch. The position of the piston is determined by the hydraulic pressure applied. If the hydraulic pressure is lost a spring will retract the piston twisting the leading edge of the blades up against the wind. It should be mentioned that this is not the only way to pitch the blades. Alternatively each blade could be fitted with a hydraulic cylinder, small electrical or hydraulic motor, so that they can be pitched independently.

A pitched blade can act as an aerodynamic brake and it is no longer necessary to include tip brakes as on a stall-regulated machine. By pitching the entire blade it is possible to control the angles of attack and thus the power output. Normally, the power is reduced by decreasing the angles of attack by pitching the leading edge of the blades up against the wind, i.e. by increasing θ_p in the expression for the angle of attack $\alpha=\phi-(\beta+\theta_p)$, where ϕ is the flow angle. Alternatively, one could reduce the power output by increasing the angle of attack, thus forcing the blades to stall. This is called active stall. Due to the turbulent characteristic of the wind, the instantaneous power output of a pitch-regulated machine will often exceed the rated power, and the timescales of these fluctuations (see Figure 7.5) are smaller than the time it takes to pitch the blades. Figure 7.5 shows a start-up of the same turbine as the one in Figure 7.3, but now running as a pitch-controlled machine. It is seen that the start-up occurs much more smoothly since the blades are gradually pitched from 50° to about 15°, see the second curve in Figure 7.5. Comparing the time history of the power output after the start up for the turbine

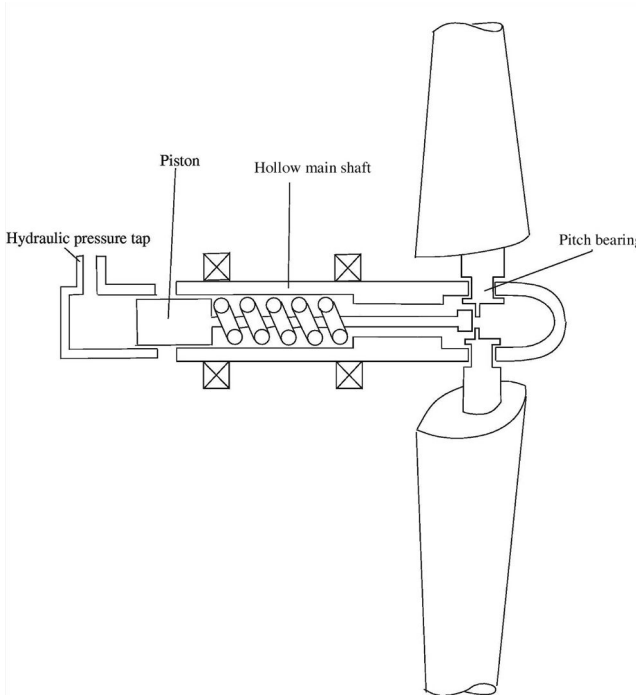

Figure 7.4 Sketch of mechanism to change the pitch of the blades through a piston placed inside the main shaft

running as a pitch-regulated wind turbine (Figure 7.5) with the time history of the power output for the same turbine running as a stall-regulated wind turbine (Figure 7.3), it is seen that the peaks are smaller when the turbine is running as a stall-regulated turbine. Since turbulent fluctuations of the wind speed occur much faster than the time it takes to pitch the blades, the power from a pitch-regulated wind turbine follows for some time the stationary power curve for a fixed pitch (see Figure 6.10). For high wind speeds the stationary power curve for a pitch-regulated machine at a fixed pitch has a much higher slope dP/dV_o than the corresponding stationary power curve for a stall-regulated wind turbine and thus a larger variation $\Delta P = dP/dV_o \times \Delta V_o$ for the wind speed interval ΔV_o. This is the reason that the power fluctuations are lower for a stall-regulated wind turbine than for a pitch-regulated machine at high wind speeds, when an asynchronous generator is used. The function diagram when the pitch is used to control the power is shown in Figure 7.6. The controller of a classical pitch-regulated wind turbine is, however, not responding to the wind speed but reacts directly on the power, e.g., as:

$$\frac{d\theta_p}{dt} = \frac{KI(P - P_{ref})}{1 + \dfrac{\theta_p(t)}{KK}} \tag{7.3}$$

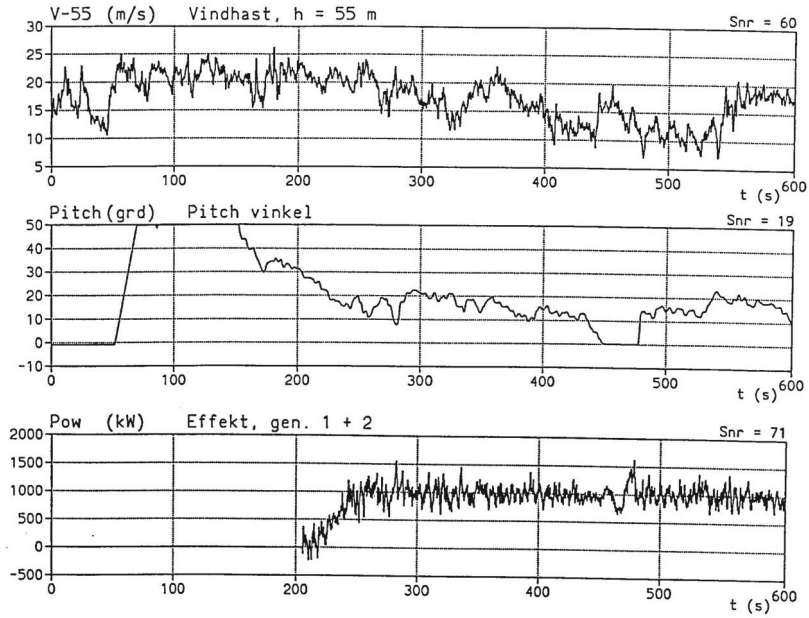

Figure 7.5 Starting a pitch-regulated wind turbine at high wind speed, Elkraft 1MW demonstration wind turbine at Avedøre, Denmark

where KI is an integration constant and KK is the gain reduction that reduces the pitch rate at high values of the pitch angle itself. High values of the pitch angle correspond to high wind speeds where also the loads are very big and thus very sensitive to the pitch angle.

To overcome the problem with the large peaks in power and loads on a pitch-regulated wind turbine at high wind speeds, a system called OptiSlip® is applied by VESTAS. OptiSlip® utilizes that the torque characteristic, i.e. the slip, for an asynchronous generator, can be altered by changing an inner resistance R in the generator. A torque characteristic with, for example, a constant torque, after a certain value, $M_G=M_{nom}=$const, can thus be obtained as indicated by the thick curve in Figure 7.7, which shows the effective characteristic obtained with the different resistances R_1, R_2, R_3, …. In high winds the power output from a wind turbine using OptiSlip® will thus be almost constant with very small fluctuations around the nominal value.

When the rotor torque M_R exceeds M_{nom} the rotor will start to accelerate in accordance with Equation 7.2. The control system detects this and starts pitching the blades. The advantage is that the timescale to accelerate the rotor is larger than the timescale to pitch the blades, so that there is enough time available to physically move the blades, and at the same time, a much smoother power output is obtained since the torque on the generator shaft is almost constant. Further, the loads are also reduced, which increases the fatigue lifetime. The pitch system is thus controlling the rotational speed and not the power.

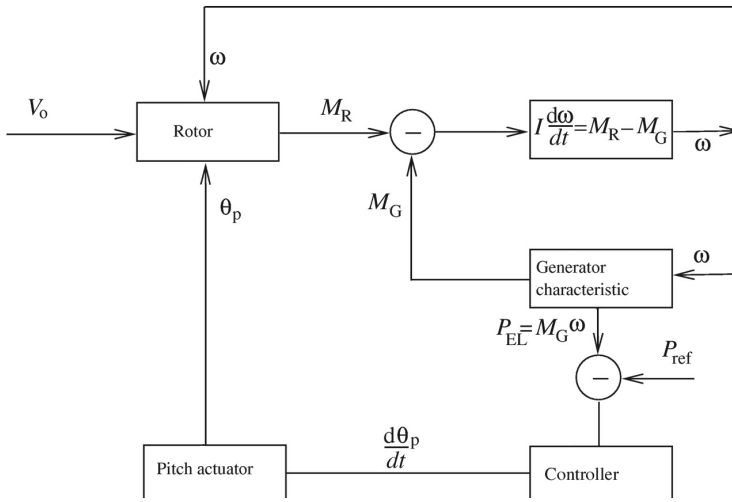

Figure 7.6 Function diagram for a pitch-regulated wind turbine controlling the power

An example illuminating the steady output for stall regulation, pitch regulation and active stall is given on the basis of the previously introduced stall-controlled NTK 500/41 wind turbine. Using the same blades, the same rotational speed and the same Weibull parameters, the potential increase from a pitch mechanism in the annually captured energy is investigated. It is decided to use the same generator, i.e. the rated mechanical power remains unaltered at approximately 580kW. For each wind speed an optimum pitch angle is sought by varying the pitch in a BEM calculation, see Figure 7.8. It is seen that the

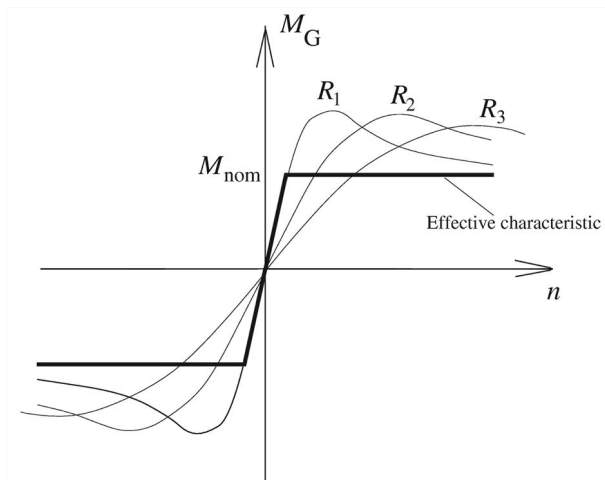

Figure 7.7 Torque characteristic for an asynchronous generator with variable slip

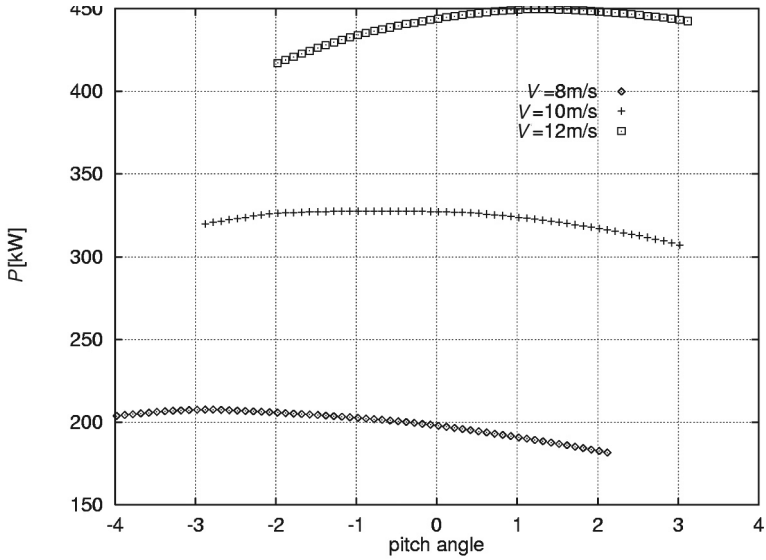

Figure 7.8 Optimum pitch angle for different wind speeds

mechanical power for a constant wind speed has an optimum value for the global pitch, but that for this turbine the variation is relatively small.

For higher wind speeds the optimum value of the power exceeds the rated power as shown in Figure 7.9. In the figure is also seen that there exists two choices for the pitch, which yields exactly the rated power. The smaller value, θ_p=0.16°, corresponds to active stall since the local angles of attack are higher than the limit for unseparated flow. The higher value, θ_p=20.2°, corresponds to classical pitch regulation, where the local angles of attack and thus the loads on the blades are reduced.

The computed mechanical steady power curves for the NTK 500/41 wind turbine running as a stall- and pitch-controlled wind turbine are plotted in Figure 7.10. For the variable pitch machine, the optimum values for the pitch have been used for the smaller wind speeds. These optimum pitch values are shown in Figure 7.11 as a function of the wind speed. For wind speeds higher than 14m/s, the blades must be pitched to ensure a power below the rated value. The lower branch in Figure 7.11 shows the pitch setting on a machine controlled by active stall, and the upper branch shows the pitch setting on a pitch-controlled wind turbine.

Assuming the same Weibull parameters as in the example concerning the NTK 500/41 machine, i.e. k=1.9 and A=6.8m/s, the annual energy production from the turbine, running as a pitch-regulated machine, is 1.11×10^6kWh. In this example an increase in the annual energy production of approximately 2 per cent has thus been achieved by changing from a stall- to a pitch-regulated machine. It should be noted that the annual energy production in both cases have been

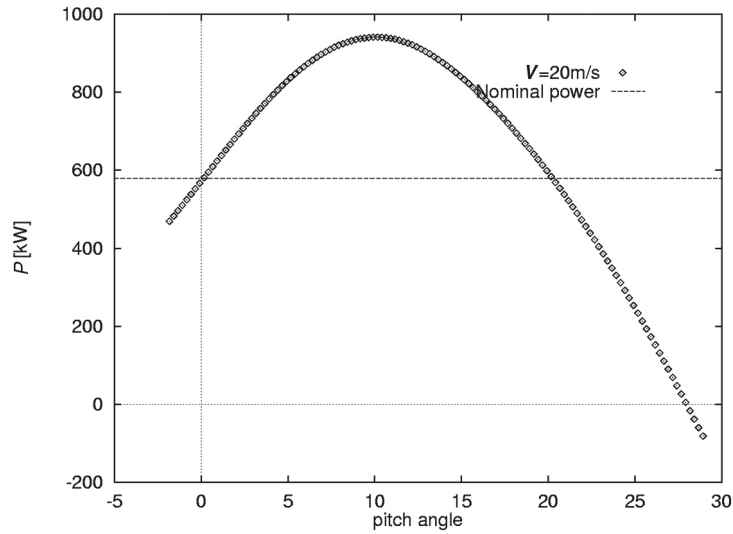

Figure 7.9 Variation of the mechanical power with the pitch for a wind speed of 20m/s on a NTK 500/41 wind turbine

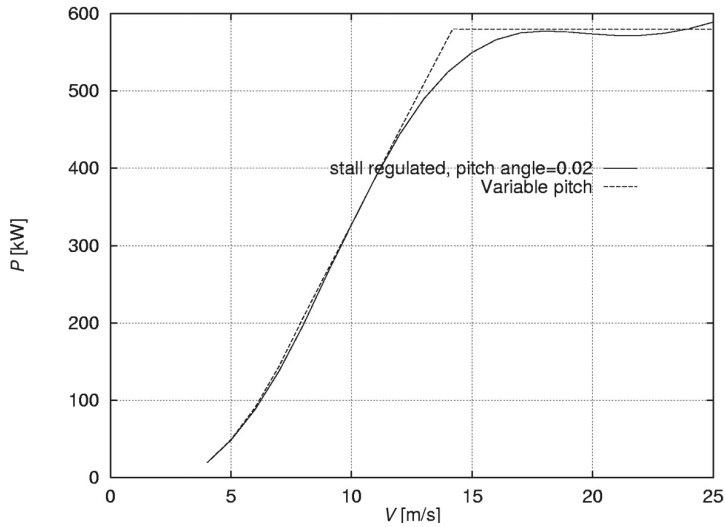

Figure 7.10 Computed power curve for the NTK 500/41 wind turbine running as a stall-controlled or pitch-regulated machine

computed using the mechanical power, i.e. the losses in the generator and in the gearbox have been ignored. The main contribution to this achievement comes from the shape of the power curve just before reaching the rated power, where the power curve of the pitch-regulated wind turbine is steeper than the stall-regulated

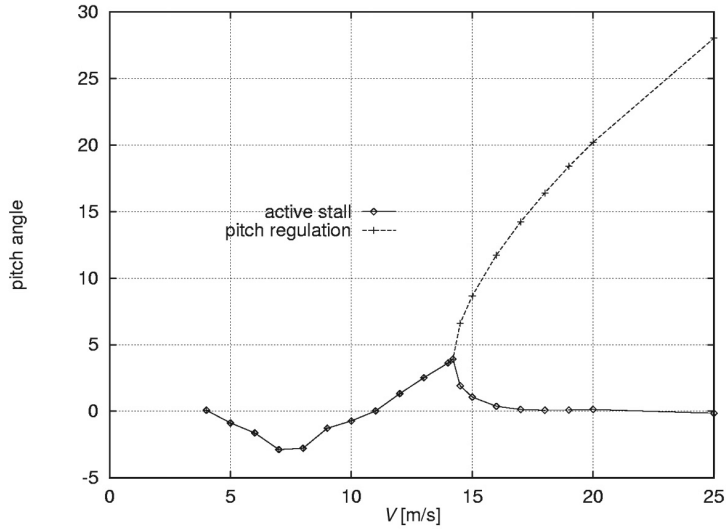

Figure 7.11 Optimum values for the pitch and the necessary pitch to avoid exceeding the nominal power

machine. Due to the turbulent characteristics of the wind the power curve on a real pitch-regulated machine is not as steep close to P_{nom} as the theoretical curve indicates in Figure 7.10, so the increase in the annual production is probably slightly lower than estimated from the theoretical power curves.

Yaw control

Instead of limiting the power output using pitch or stall regulation it is possible to control the yaw of the turbine. On normal pitch- or stall-regulated machines, it is common to have a yaw drive, which is constantly trying to rotate the nacelle to minimize the yaw misalignment in order to get as much air through the rotor disc as possible. On a yaw-controlled machine, the rotor is turned out of the wind in high winds to limit the airflow through the rotor and thus the power extraction. Yaw control was used on the old Western mills. For larger machines, to the author's knowledge only the 1.5MW Italian prototype called GAMMA 60 is yaw-controlled. Therefore yaw control will not be treated further in this text.

Variable-speed pitch regulation

The power coefficient is generally a function of both the tip speed ratio and the pitch angle, $C_p(\theta_p,\lambda)$, and by applying variable speed on a pitch-regulated rotor it is possible to run the turbine at the optimum point, $C_{p,\,max}$ occurring at $\theta_{p,opt}$ and λ_{opt}. From Figure 6.8, that shows the C_p–λ curve for the NTK 500/41 machine, it is seen that the turbine for this pitch angle runs most efficiently at λ approximately

equal to 9.8. From a C_p–λ curve, a plot showing the power P as a function of the rotational speed ω for different wind speeds, can be derived as:

$$P = \tfrac{1}{2}\rho V_o^3 A C_p(\lambda) \tag{7.4}$$

and:

$$\omega = \frac{\lambda V_o}{R}. \tag{7.5}$$

This has been done for the NTK 500/41 machine and the result is shown in Figure 7.12. This turbine is equipped with an asynchronous generator forcing the blades to rotate at 27.1RPM indicated by the vertical line. It is seen that the turbine is running most efficiently at a wind speed V_o of approximately 7m/s corresponding to $C_{p,\,max}$. Some stall- and pitch-regulated wind turbines using an asynchronous generator, i.e. running at a fixed rotational speed, therefore have two generators, one which is efficient at lower wind speeds and one which is efficient at higher wind speeds. If another type of generator had been used, which is able to run at different rotational speeds, the turbine could be operated at the optimum rotational speed for each wind speed, as indicated in Figure 7.12 by the operational line that intersects all the top points in the curves for the different wind speeds. All points on this line correspond to the highest C_p that can be obtained for the applied pitch angle. It is noted that at a fixed value of the tip speed ratio, λ, the angular velocity, ω, and thus the tip speed will increase proportionally with the wind speed according to Equation 7.5. Due to noise emission the tip speed is limited to approximately ωR=70–80 m/s and therefore the optimum tip speed ratio can only be obtained for lower wind speeds. The alternating current produced by such a generator will have a frequency different from the frequency of the grid (50Hz in Europe). Therefore the alternating current, AC, is first transformed to direct current, DC, and then back to alternating current with the correct frequency using a so-called ACDC/DCAC device.

Combining that the power is the torque multiplied with the angular velocity, P=Mω, with Equations 7.4 and 7.5 yields:

$$M = \tfrac{1}{2}\rho\omega^2 R^3 A C_p(\lambda,\theta_p)/\lambda^3. \tag{7.6}$$

The generator characteristic for the highest obtainable power coefficient $C_{p,\,max}(\theta_{p,opt}, \lambda_{opt})$ is thus:

$$M_{opt} = \tfrac{1}{2}\rho\omega^2 R^3 A C_{p,max}(\theta_{p,opt},\lambda_{opt})/\lambda_{opt}^3 = const\cdot\omega^2 \tag{7.7}$$

This characteristic should be used until the maximum allowable angular velocity, ω_{max}, is reached corresponding to a tip speed of approximately 70–80 m/s (region I in Figure 7.13). At ω_{max} the power, P=M_G.ω may be lower than the rated power and a steep change in the generator torque is needed for a very

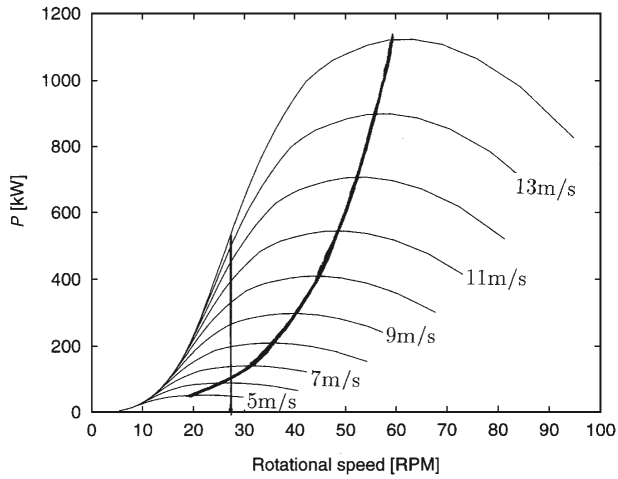

Figure 7.12 Constant speed versus variable speed

small increase in angular velocity (region II in Figure 7.13). Now the rated power is reached and the torque characteristic can continue as a constant value or the generator torque may decrease as $M_G(\omega) = P_{rated}/\omega$ to keep the power constant at rated (region III in Figure 7.13). If the rotor torque exceeds the maximum generator torque it will accelerate according to Equation 7.2, but since the inertia of the rotor is large it will take some time for the rotor to build up speed. In case the wind turbine is operated at rated power the pitch controller compares the actual rotor speed with a reference speed and adjusts the pitch angle to force the angular velocity to get back to the reference value, as described in more details below. Since the time it takes to accelerate the rotor is high compared to a realistic pitch rate in the order of 10°/s there is plenty of time to control the rotational speed and at the same time have a constant power output. Below rated power the pitch angle is often constant corresponding to the value of $C_{p,max}$ and the rotational speed is governed by Equation 7.2 where the rotor torque is given by the aerodynamics and the generator torque by the torque characteristic $M_G(\omega)$, shown in Figure 7.13. This is the description of a VSPR (variable speed variable pitch) machine, which is torque controlled below rated power and pitch and torque regulated after rated power, where the rotational speed is kept close to a reference value and at the same time obtaining a constant power. This cures the problem with the large spikes/fluctuations in the power from a pitch-regulated wind turbine operating at constant rotational speed as, for example, seen in the measured time series of the power in Figure 7.5 for pitch-regulated wind turbine using an asynchronous generator with almost constant rotational speed. The function diagram for a pitch regulated variable speed machine is shown in Figure 7.14.

The basic pitch controller is a PI regulation, calculating a new collective setpoint pitch angle, θ_p^{set}, for all blades (input to the pitch actuator) that at rated

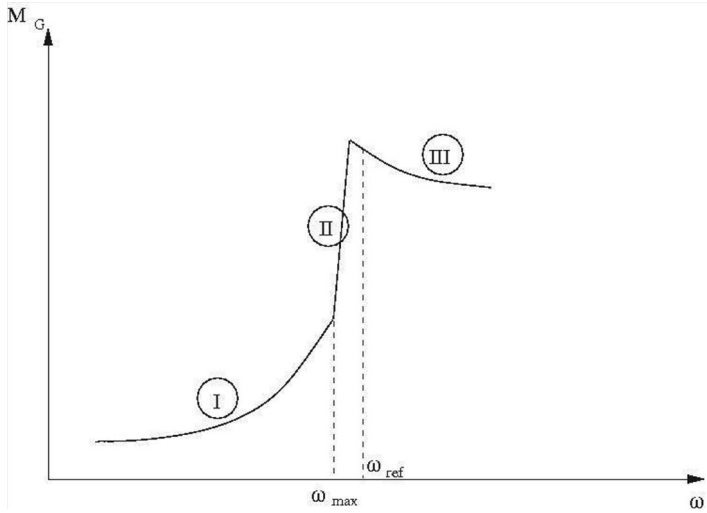

Figure 7.13 A generic torque characteristic for a variable-speed pitch-regulated wind turbine

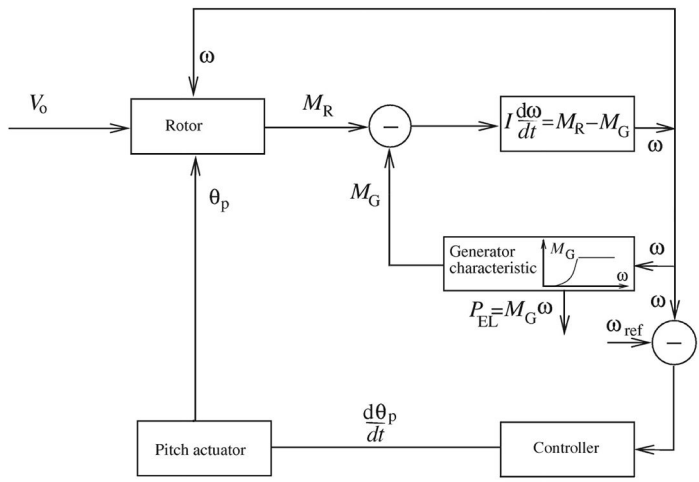

Figure 7.14 Schematic drawing of a function diagram for a pitch-regulated variable-speed machine

power will force the angular velocity towards a reference value, see Equation 7.8. The setpoint value is comprised by an integral part, θ_p^I, and a proportional part, θ_p^P. The proportional and integral gains are multiplied by a gain reduction, *GK*, that limits the change in pitch angle at high pitch angles corresponding to high wind speeds where the aerodynamic loads are more sensitive to changes in the angles of attack.

$$\theta_p^I(t) = \int GK \cdot K_I(\omega(t) - \omega_{ref})dt = \theta_p^I(t - \Delta t) + GK \cdot K_I(\omega(t) - \omega_{ref})\Delta t \tag{7.8}$$

$$\theta_p^P(t) = GK \cdot K_p(\omega(t) - \omega_{ref})$$

$$\theta_p^{set}(t) = (\theta_p^I(t) + \theta_p^P(t))$$

$$GK(\theta_p) == \frac{1}{1 + \frac{\theta_p}{KK}}$$

Below rated power the pitch is kept constant, at least in region I, Figure 7.13, where the rotor is operating at the optimum tip speed ratio and pitch angle. In region II, where the tip speed ratio is no longer the optimum, a small gain in power can potentially be achieved by adjusting the pitch. If the turbine has been running for a long time below rated power the rotational speed where $\omega(t) < \omega_{ref}$, the integral term will become more and more negative and has to be limited. Also the final setpoint pitch angle should be limited between a maximum and minimum value as in Equation 7.9.

$$\theta_p^I = \max(\theta_p^I, \theta_{p,min})$$

$$\theta_p^I = \min(\theta_p^I, \theta_{p,max})$$

and (7.9)

$$\theta_p^{set} = \max(\theta_p^{set}, \theta_{p,min})$$

$$\theta_p^{set} = \min(\theta_p^{set}, \theta_{p,max})$$

The minimum pitch angle, $\theta_{p,min}$, could be the value corresponding to the highest possible power coefficient in which case this will be the pitch angle in both Regions I and II.

In Hansen et al. (2005) and Jonkman et al (2009) it is stated how the two gains in Equation 7.8 can be estimated as

$$K_p = \frac{2I_{drivetrain}\omega_{rated}\varsigma_\phi\omega_{\phi\eta}}{N_{Gear}\left(-\frac{dP}{d\theta_p}\right)_{rated}}$$

$$K_I = \frac{I_{drivetrain}\omega_{rated}\omega_{\phi\eta}^2}{N_{Gear}\left(-\frac{dP}{d\theta_p}\right)_{rated}} \tag{7.10}$$

$I_{drivetrain}$ is the total inertia moment of the drivetrain on the low speed shaft, ω_{rated} is the rotational speed of the low speed shaft at rated power, N_{gear} is the gear ratio between the low- and high-speed shaft. The dynamic response of the PI-regulator is second order with resonance frequency $\omega_{\varphi\eta}$ and damping ratio ς_ϕ. Values of $0.6 < \varsigma_\phi < 0.7$ and $\omega_{\varphi\eta} = 0.6$ are recommended. $dP/d\theta_p$ is the slope of the

power curve with respect to a change in the pitch angle and can be estimated numerically with a steady BEM code assuming constant induced velocities, also denoted a frozen-wake approach. In Equation 7.10 the value for this slope should be evaluated at rated wind speed, and the constant, KK, in the gain reduction term in Equation 7.8 is the pitch angle where this slope has doubled its value from the value at rated wind speed. Having a steady BEM code one can estimate the necessary generator torque characteristic as sketched in Figure 7.13 and calculate the three gains, K_p, K_I and KK.

Example: NREL rotor

Using the description of the NREL reference rotor from Jonkman et al. (2009) the gains and the torque characteristic have been calculated using a steady BEM code and hereafter an unsteady BEM code, as described in Chapter 9, is applied. The rotor is considered stiff except for the rotation of the shaft, which is determined by Equation 7.2, where the generator torque as function of shaft speed is given by a characteristic as shown in Figure 7.13, and the pitch angle in each time step is calculated from Equations 7.8 and 7.9. First, the response is calculated for a sudden increase in wind speed at t=300s from 6 m/s to 8 m/s. The computed time series of the rotor speed and power is shown in Figures 7.15 and 7.16, respectively. The rated power is first reached at a wind speed slightly above 11 m/s, so the pitch angle is constant at 0° for the simulations shown in Figures 7.15 and 7.16 and a close correlation between the shaft speed and the power is observed. Next a simulation above rated wind speed is made at a mean value of 14 m/s assuming only a temporal variation of the wind speed due to turbulence. A time series is created based on a Kaimal spectrum using a turbulence intensity of 12 per cent as described in Chapter 14 and shown graphically in Figure 7.17. It must be emphasized that in reality there is also a spatial variation of the wind speed that must also be simulated, see Chapter 14.

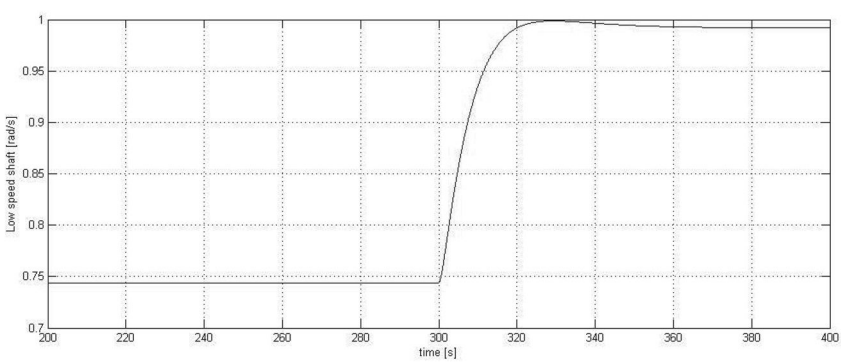

Figure 7.15 Computed time series of the low speed shaft angular velocity of the NREL 5 MW reference turbine for a sudden change in wind speed at t=300s from 6 m/s to 8 m/s

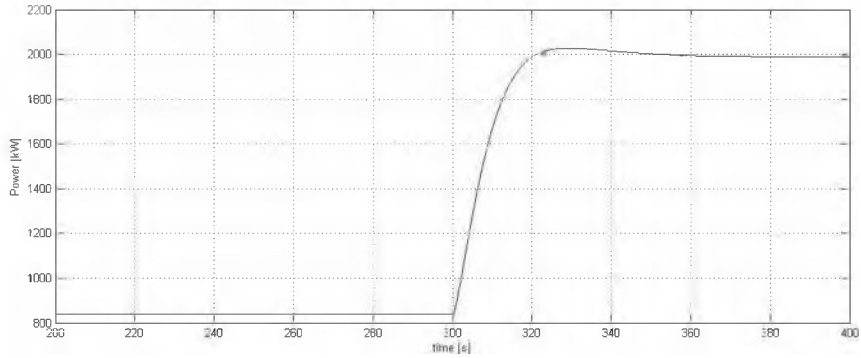

Figure 7.16 Computed time series of the produced power from the NREL 5 MW reference turbine for a sudden change in wind speed at t=300s from 6 m/s to 8 m/s

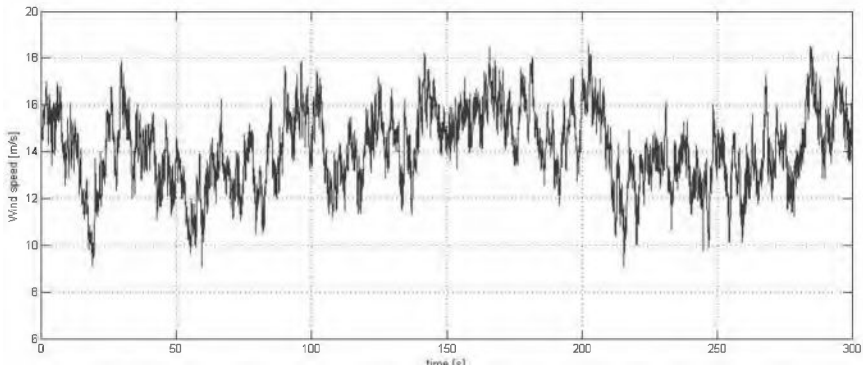

Figure 7.17 Simulated time history of turbulent wind speed using a Kaimal spectrum, a mean wind speed of 14 m/s and a turbulence intensity of 12 per cent

Figures 7.18 to 7.20 show the computed time histories of the rotor speed, the pitch angle and the produced power implementing the described collective pitch controller in an unsteady blade element momentum method and using the wind speed shown in Figure 7.17, respectively.

It is seen that the rotor speed and the pitch angle are highly correlated with the wind speed in the sense that, as the rotor speed increases with the wind speed, the pitch also increases to lower the loads and thus the rotor torque to prevent the rotor speed from increasing too much. At the same the power is almost constant, except at some short periods where the wind speed decreases below the rated wind speed (11.3 m/s). In the more realistic case where the wind speed is also spatially distributed these dips may not occur since the wind speed will not decrease below the rated value on the entire rotor, but only in some areas.

The collective pitch controller described above can be further combined with individual pitching of the blades to compensate for periodic load variations

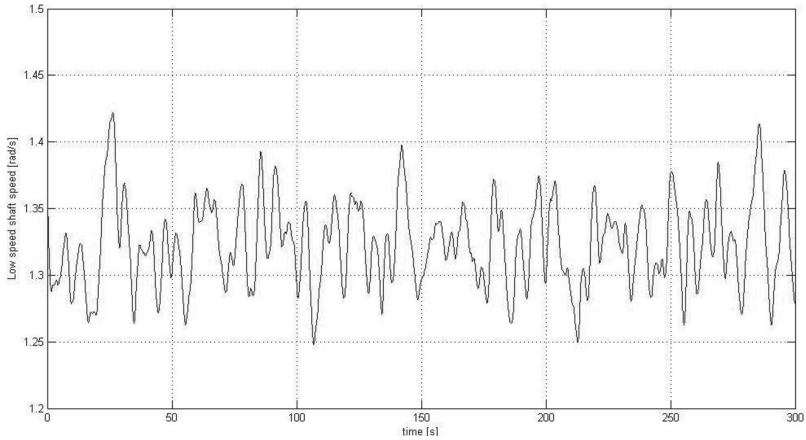

Figure 7.18 Computed rotor speed using the VSPR controller on the NREL 5 MW reference wind turbine and the wind speed time history shown in Figure 7.17

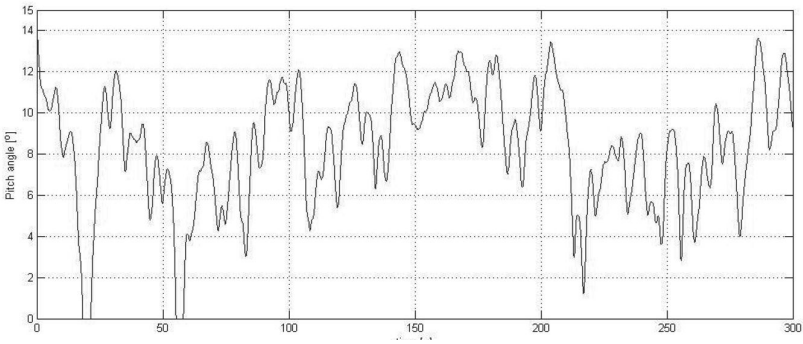

Figure 7.19 Computed pitch angle using the VSPR controller on the NREL 5 MW reference wind turbine and the wind speed time history shown in Figure 7.17

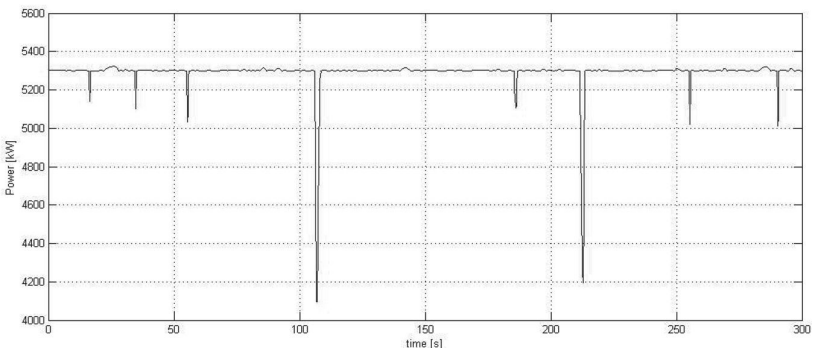

Figure 7.20 Computed power using the VSPR controller on the NREL 5 MW reference wind turbine and the wind speed time history shown in Figure 7.17

stemming from, for instance, wind shear where the aerodynamic loads on a blade will be higher at the top position than when the same blade is pointing downwards. Another example could be a rotor standing partially in the wake of an upstream wind turbine where the aerodynamic loads on a blade is decreased each time it enters the wake once per revolution (see, for example, Bottasso et al., 2014).

References

Bottasso, C.L., Croce, A., Riboldi, C.E.D. and Salvetti, M. (2014) 'Cyclic pitch control for the reduction of ultimate loads on wind turbines', TORQUE 2014, *Journal of Physics: Conference Series* vol. 524, pp. 12063–12072.

Hansen, M.H., Hansen, A., Larsen, T.J., Øye, S., Sørensen, P. and Fuglsang, P. (2005) *Control Design for a Pitch-Regulated, Variable Speed Wind Turbine*, Risø-R-1500(EN). Roskilde: Risø National Laboratory.

Jonkman, J., Butterfield, S., Musial, W. and Scott, G. (2009) *Definition of a 5-MW Reference Wind Turbine for Offshore System Development*, Technical Report NREL/TP-500-38060. Golden, CO: NREL.

8 Optimization

After having derived all necessary equations to compute a given wind turbine one would like to use these to compute an optimum design. First, an optimum design must be defined, but since the purpose of a wind turbine is to produce electricity, and this should be at a competitive cost, the object function is a design that can last for a typical design lifetime of 20 years and:

At a given site minimize energy production cost $/kWh.

To do this it is necessary to estimate a cost function for every component of the wind turbine and a maintenance cost. From a purely technical point of view, the optimum design could be a wind turbine which for a given rotor diameter captures as many kWh/year as possible. If the turbine is sited on a spot where the wind speed V_o is constant in time, it is obvious to optimize the power coefficient at this wind speed. Since the wind speed is not constant an optimum design could have lower $C_{p,max}$ as sketched in the Design 2 in Figure 8.1.

As shown in Chapter 6, the annual energy production is a combination of the wind distribution and the power curve. So the optimum design also depends on the actual siting. A BEM method as described earlier can be coupled with an

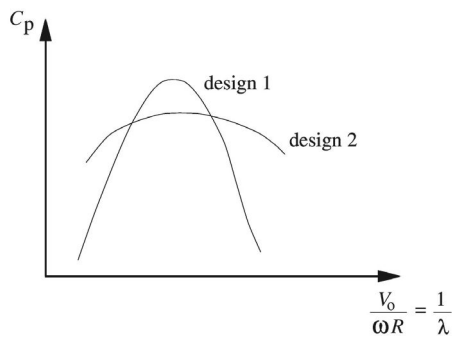

Figure 8.1 Two different designs. Design 1 has a high $C_{p,max}$ but C_p drops off quickly at different tip speed ratios. Design 2 has a lower $C_{p,max}$ but performs better over a range of tip speed ratios

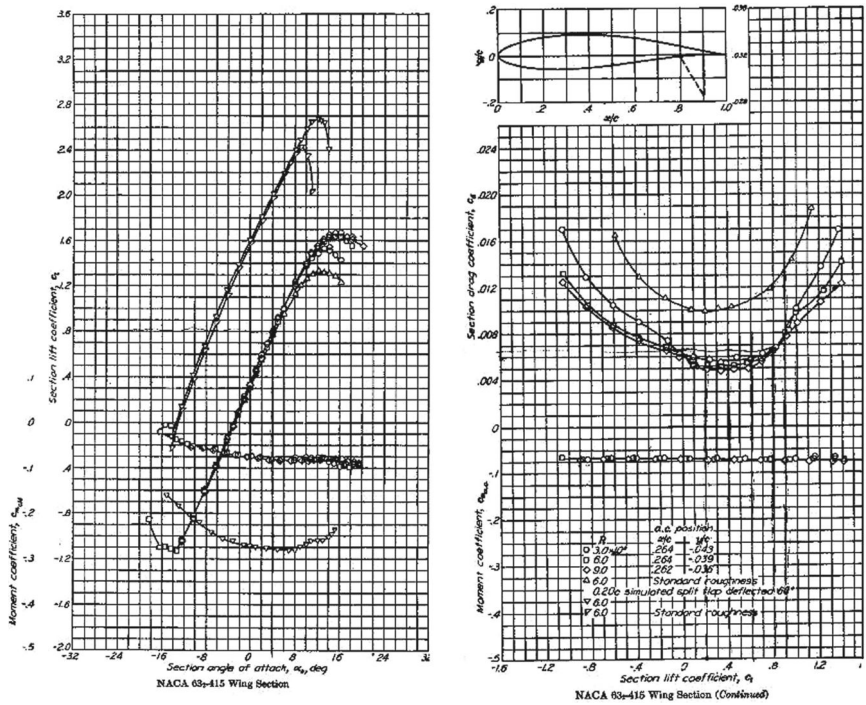

Figure 8.2 Airfoil data for the NACA63-415 airfoil (reproduced from Abbot and von Doenhoff, 1959, with permission)

optimization algorithm with appropriate constraints to optimize, e.g., the geometry of the blades. Of course it is imperative afterwards to verify that the calculated optimum design will also survive the entire design period taking both extreme and fatigue loads into account. It is possible to compute analytically the geometry of Design 1 in Figure 8.1 with the already derived equations as, for example, described in Glauert (1935). Such a design is more interesting for an airplane propeller, which is mainly operating at cruise speed. It could perhaps also be interesting for a wind turbine with variable rotational speed. Such a machine can ideally by a control mechanism be kept at the optimum tip speed ratio, λ_{opt}, and pitch angle, $\theta_{p,opt}$, as described in the section concerning control and regulation.

First, a good airfoil is chosen, which must be relatively roughness insensitive and possess an acceptable stall characteristic. Also noise considerations might influence the choice of airfoil. A possible choice is the NACA63-415 airfoil, which has proven to possess good stall characteristics on stall-regulated wind turbines. Since it is planned to operate in one point only, it is ensured that the effective angle of attack has an optimum value along the entire span. The optimum value is where the ratio between the lift to the drag is highest.

In Figure 8.2 is seen that the NACA63-415 airfoil at $Re=3\times10^6$ has a maximum value of C_l/C_d of approximately 120 at an angle of attack a of 4°. It is also seen that this maximum value drops to approximately 67 when standard

roughness is added to the airfoil, but at the same optimum angle of attack of 4°. In the following example the values with roughness are used, i.e. $C_{l,opt}(4^o)=0.8$ and $C_{d,opt}(4^o)=0.012$. Further, the number of blades B is chosen as three, and the design point to $\lambda=\omega R/V_o=6$. Since an angle of attack of 4° is chosen in the design point, the flow is attached to the blades and Equations 4.32 and 4.38 are valid and can be combined to give an optimum relationship between x and a:

$$16a^3 - 24a^2 + a(9 - 3x^2) - 1 + x^2 = 0. \tag{8.1}$$

The optimum value of a' is found using Equation 4.38 and the optimum local pitch angle can then be computed as:

$$\theta_{opt} = \phi - \alpha_{opt} \tag{8.2}$$

since it is recalled that the flow angle is computed as:

$$\tan\phi = \frac{(1-a)V_o}{(1+a')\omega r} = \frac{(1-a)}{(1+a')x}. \tag{8.3}$$

The optimum chord distribution is found from Equation 6.35 using the optimum values for a and a':

$$\frac{c(x)}{R} = \frac{8\pi F a x \sin^2\varphi}{(1-a)B\lambda C_n}, \tag{8.4}$$

where

$$C_n = C_{l,opt}\cos(\phi) + C_{d,opt}\sin(\phi). \tag{8.5}$$

For $\lambda=6$, $\alpha_{opt}=4$, $C_{l,opt}=0.8$, $C_{d,opt}=0.012$ and the number of blades $B=3$ the optimum chord and pitch distribution can now be computed and the solution is shown graphically in Figures 8.3 and 8.4.

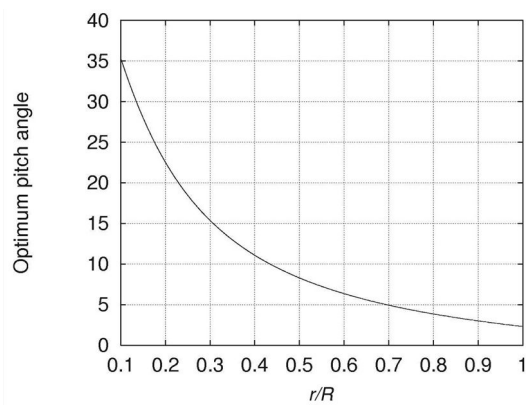

Figure 8.3 Optimum pitch distribution for $\lambda=6$, $\alpha_{opt}=4$, $C_{l,opt}=0.8$, $C_{d,opt}=0.012$ and $B=3$

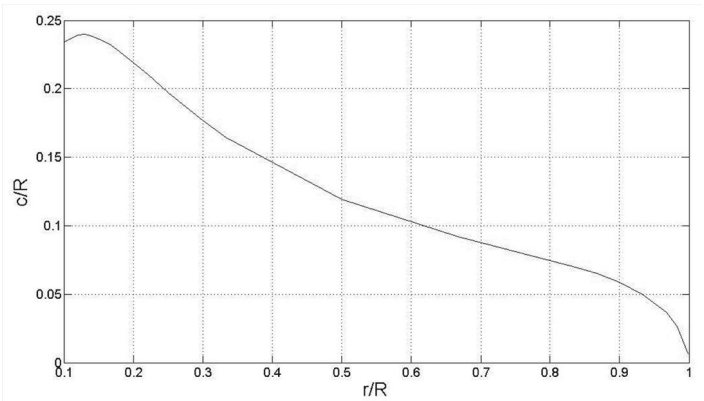

Figure 8.4 Optimum chord distribution for $\lambda=6$, $\alpha_{opt}=4$, $C_{l,opt}=0.8$, $C_{d,opt}=0.012$ and $B=3$

References

Abbot, H. and von Doenhoff, A.E. (1959) *Theory of Wing Sections*, New York: Dover Publications.

Glauert, H. (1935) 'Airplane propellers' in W.F. Durand (ed.) *Aerodynamic Theory*, vol. 4, pp. 169–360, New York: Springer.

9 Unsteady BEM model

To estimate the annual energy production from a wind turbine at a given site with known wind distribution it is sufficient to apply a steady BEM method as described in earlier chapters to compute the steady power curve. But due to the unsteadiness of the wind seen by the rotor from atmospheric turbulence, wind shear and the presence of the tower it is necessary to use an unsteady BEM method to compute realistically the aeroelastic behaviour of the wind turbine. To do this a complete structural model of the wind turbine is also required and must be coupled with the unsteady BEM method since the velocity of, for example, the vibrating blades and tower changes the apparent wind seen by the blades and thus also the aerodynamic loads.

Since the wind changes in time and space, it is important at any time to know the position relative to a fixed coordinate system of any section along a blade. The fixed or inertial coordinate system can be placed at the bottom of the tower. Depending on the complexity of the structural model a number of additional coordinate systems can be placed in the wind turbine. The following example illustrates a very simple model, where the wind turbine is described by four coordinate systems as shown in Figure 9.1.

First, an inertial system (coordinate system 1) is placed at the base of the tower. System 2 is non-rotating and placed in the nacelle, system 3 is fixed to the rotating shaft and system 4 is aligned with one of the blades. Note that due to the orientation of coordinate system 2, the tilt angle θ_{tilt} must be negative if the shaft is to be nose up as sketched in Figure 9.1.

A vector in one coordinate system $\mathbf{X}_A = (x_A, y_A, z_A)$ can be expressed in another coordinate system $\mathbf{X}_B = (x_B, y_B, z_B)$ through a transformation matrix $\mathbf{a}_{AB}$:

$$\mathbf{X}_B = \mathbf{a}_{AB}\mathbf{X}_A \tag{9.1}$$

The columns in the transformation matrix $\mathbf{a}_{AB}$ express the unit vectors of system A in system B. Further, the transformation from system B to system A can be found as $\mathbf{a}_{BA} = \mathbf{a}_{AB}^T$. The rules will now be applied on the coordinate systems shown in Figure 9.1. First the transformation matrix $\mathbf{a}_{12}$ will be constructed. To begin with system 1 and 2 are identical with exception of the position of the origin. System 2 is first rotated about the x-axis with the angle θ_{yaw}. This gives a transformation matrix:

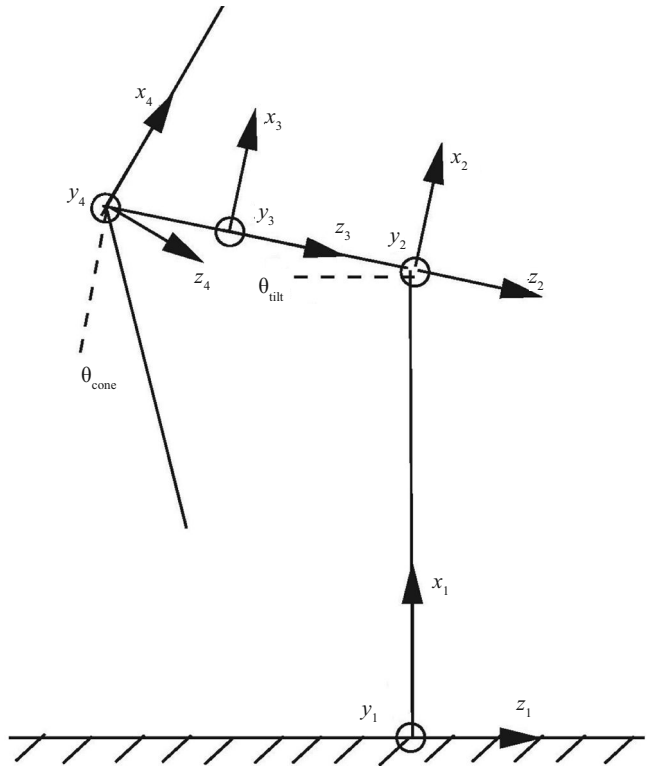

Figure 9.1 Wind turbine described by four coordinate systems

$$\mathbf{a}_1 = \begin{bmatrix} 1 & 0 & 0 \\ 0 & \cos\theta_{yaw} & \sin\theta_{yaw} \\ 0 & -\sin\theta_{yaw} & \cos\theta_{yaw} \end{bmatrix} \tag{9.2}$$

Hereafter system 2 is rotated along the *y*-axis with the angle θ_{tilt} yielding a transformation matrix:

$$\mathbf{a}_2 = \begin{bmatrix} \cos\theta_{tilt} & 0 & -\sin\theta_{tilt} \\ 0 & 1 & 0 \\ \sin\theta_{tilt} & 0 & \cos\theta_{tilt} \end{bmatrix} \tag{9.3}$$

Since system 2 is not rotated about the *z*-axis this transformation matrix then becomes:

$$\mathbf{a}_3 = \begin{bmatrix} 1 & 0 & 0 \\ 0 & 1 & 0 \\ 0 & 0 & 1 \end{bmatrix} \tag{9.4}$$

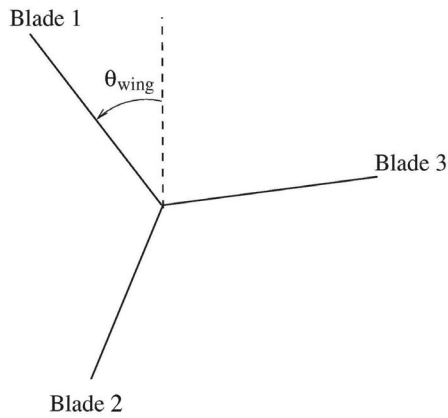

Figure 9.2 Rotor seen from downstream

The total transformation matrix, $\mathbf{X}_2 = \mathbf{a}_{12}\mathbf{X}_1$, between system 1 and system 2 is found as $\mathbf{a}_{12} = \mathbf{a}_3 \times \mathbf{a}_2 \times \mathbf{a}_1$.

Since the shaft in this simple model is assumed to be stiff, the only transformation between system 2 and system 3 is a rotation about the z-axis:

$$a_{23} = \begin{bmatrix} \cos\theta_{wing} & \sin\theta_{wing} & 0 \\ -\sin\theta_{wing} & \cos\theta_{wing} & 0 \\ 0 & 0 & 1 \end{bmatrix} \tag{9.5}$$

θ_{wing} is the rotation of blade 1 as shown in Figure 9.2.

System 4 is only rotated, θ_{cone}, about the y-axis and the transformation matrix is thus:

$$a_{34} = \begin{bmatrix} \cos\theta_{cone} & 0 & -\sin\theta_{cone} \\ 0 & 1 & 0 \\ \sin\theta_{cone} & 0 & \cos\theta_{cone} \end{bmatrix} \tag{9.6}$$

Note that in order to have the blades to cone as shown in Figure 9.1, the cone angle must be negative. A point along blade 1 is described in coordinate system 4 as $\mathbf{r}_4=(x,0,0)$, where x is the radial distance from the rotational axis to the point on the blade. To transform this vector from system 4 to the inertial system 1, the following transformations are thus required:

First the vector is transformed to system 3, which again can be transformed to system 2 and finally to system 1 as:

$$\mathbf{r}_3 = \mathbf{a}_{43} \times \mathbf{r}_4$$

$$\mathbf{r}_2 = \mathbf{a}_{32} \times \mathbf{r}_3$$

$$\mathbf{r}_1 = \mathbf{a}_{21} \times \mathbf{r}_2$$

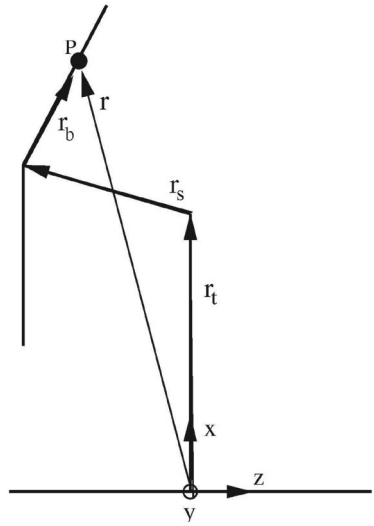

Figure 9.3 A point on the wing described by vectors

or directly as:

$$\mathbf{r}_1 = \mathbf{a}_{21} \times \mathbf{a}_{32} \times \mathbf{a}_{43} \times \mathbf{r}_4 = \mathbf{a}_{12}^{\mathrm{T}} \times \mathbf{a}_{23}^{\mathrm{T}} \times \mathbf{a}_{34}^{\mathrm{T}} \times \mathbf{r}_4.$$

To find the coordinates of the point on the blade in system 1 the vector addition shown in Figure 9.3 is applied:

$$\mathbf{r} = \begin{pmatrix} x_p \\ y_p \\ z_p \end{pmatrix} = \mathbf{r}_t + \mathbf{r}_s + \mathbf{r}_b \tag{9.7}$$

All the vectors in Equation 9.7, $\mathbf{r}_t$, $\mathbf{r}_s$ and $\mathbf{r}_b$, must be given in the same coordinate system. For a position on a blade the natural coordinate system is 1 because the wind velocity is given in the fixed system.

The undisturbed wind velocity seen by the blade is found by transforming this velocity $\mathbf{V}_1$ to system 4:

$$\mathbf{V}_o = \begin{pmatrix} V_x \\ V_y \\ V_z \end{pmatrix} = \mathbf{a}_{34} \cdot \mathbf{a}_{23} \cdot \mathbf{a}_{12} \mathbf{V}_1 = \mathbf{a}_{14} \mathbf{V}_1 \tag{9.8}$$

To find the relative velocity seen by the blade, $\mathbf{V}_{rel}$, the rotational velocity, $\mathbf{V}_{rot}$, plus the induced velocity, $\mathbf{W}$, must be added as vectors to $\mathbf{V}_o$ in system 4 as shown in Figure 9.4.

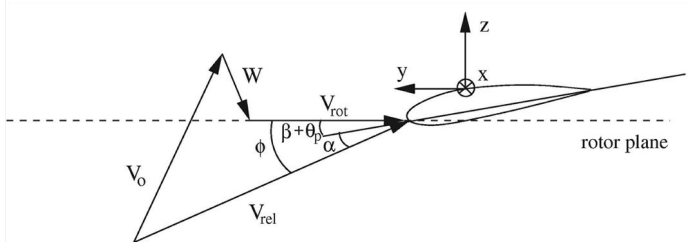

Figure 9.4 Velocity triangle seen locally on a blade

$$\mathbf{V}_{rel} = \mathbf{V}_o + \mathbf{V}_{rot} + \mathbf{W} \quad \Rightarrow$$

$$\begin{pmatrix} V_{rel,y} \\ V_{rel,z} \end{pmatrix} = \begin{pmatrix} V_y \\ V_z \end{pmatrix} + \begin{pmatrix} -\omega x \cos\theta_{cone} \\ 0 \end{pmatrix} + \begin{pmatrix} W_y \\ W_z \end{pmatrix} \tag{9.9}$$

The angle of attack, α, can be computed if the induced velocity, **W**, is known:

$$\alpha = \phi - (\beta + \theta_p), \tag{9.10}$$

where:

$$\tan\phi = \frac{V_{rel,z}}{-V_{rel,y}}. \tag{9.11}$$

Knowing, α, the lift and drag coefficients can be found from tabulated airfoil data.

The essence of the BEM method is to determine the induced velocity, **W**, and thus the local angles of attack.

From a global consideration the rotor acts as a disc with a discontinuous pressure drop across it. The thrust generated by this pressure drop induces a velocity normal to the rotorplane, W_n, that deflects the wake as shown in Figure 9.5.

From simple momentum theory it is known that the induced velocity in the far wake is twice the induced velocity in the rotorplane. From Bramwell (1976) it is stated that Glauert's relation between the thrust and this induced velocity for a gyrocopter in forward flight (similar to lifting line result for an elliptically loaded circular wing) is:

$$W_n = \mathbf{n} \cdot \mathbf{W} = \frac{T}{2\rho A |\mathbf{V}'|} \tag{9.12}$$

where $|\mathbf{V}'| = |\mathbf{V}_o + \mathbf{n}(\mathbf{n} \cdot \mathbf{W})|$.

n is the unit vector in the direction of the thrust, which in system 3 has the coordinates **n** = (0,0,–1).

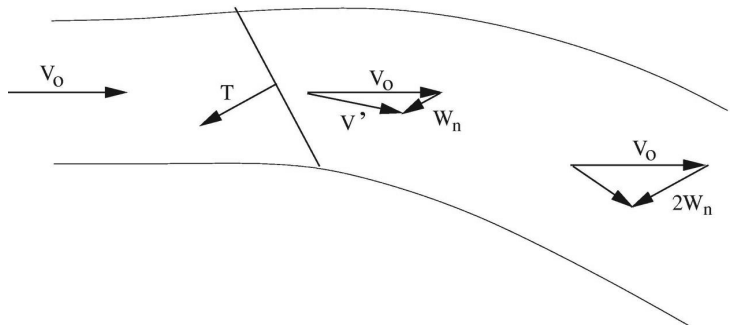

Figure 9.5 The wake behind a rotor disc seen from above

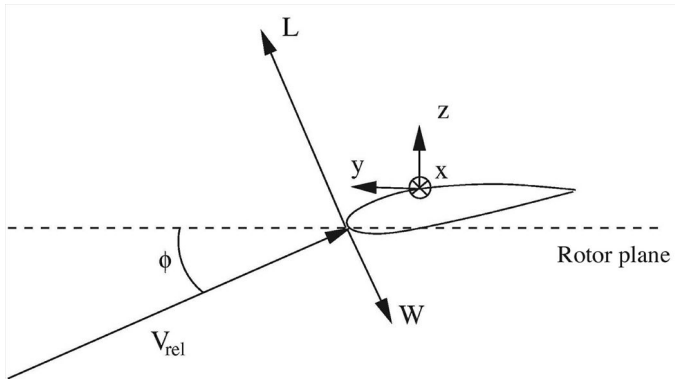

Figure 9.6 The local effect on an airfoil

Further, Equation 9.12 reduces to the classical BEM theory for zero yaw misalignment. A gyrocopter in forward flight corresponds to 90° yaw misalignment and it is therefore postulated that Equation 9.12 is valid for any yaw angle, which, in fact, is far from obvious.

Figure 9.6 is focused on the local effect close to a blade section. It is assumed that only the lift contributes to the induced velocity, and that the induced velocity acts in the opposite direction of the lift.

The force from this blade at this radial position is assumed to affect the air in the area $dA = 2\pi r dr / B$, so that all B blades cover the entire annulus of the rotor disc at radius r, see Figure 9.7.

Equation 9.13 is derived from Equation 9.12 and Figures 9.6 and 9.7.

$$W_n = W_z = \frac{-l\cos\phi \cdot dr}{2\rho \dfrac{2\pi r dr}{B} F\left|\mathbf{V}_o + f_g \mathbf{W}_n\right|} = \frac{-Bl\cos\phi}{4\pi\rho r F\left|\mathbf{V}_o + f_g \mathbf{W}_n\right|} \tag{9.13}$$

For the tangential component a similar expression is postulated:

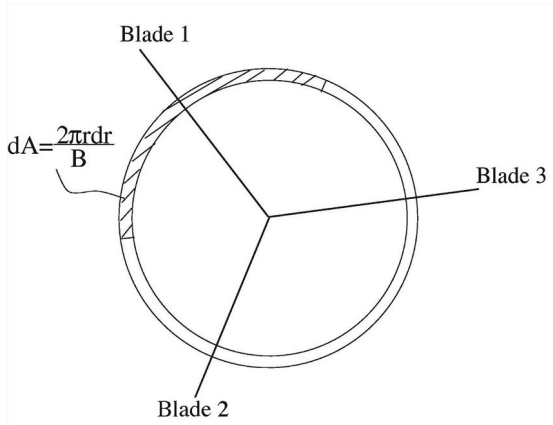

Figure 9.7 Annular strip

$$W_t = W_y = \frac{-Bl\sin\phi}{4\pi\rho rF\left|\mathbf{V}_o + f_g\mathbf{W}_n\right|} \tag{9.14}$$

F is Prandtl's tip loss factor. It is noted that the equations for the induced velocity are identical with the classical BEM method in case of zero yaw misalignment and can be reduced to the well-known expression:

$$C_T = 4aF(1 - f_g \cdot a), \tag{9.15}$$

where by definition for an annual element of infinitesimal thickness, dr,

$$C_T = \frac{dT}{\frac{1}{2}\rho V_o^2 dA} \tag{9.16}$$

f_g usually referred to as the Glauert correction is an empirical relationship between the thrust coefficient C_T and the axial induction factor a, in the turbulent wake state and if Equation 6.38 is used assumes the form:

$$f_g = \begin{cases} 1 & for\ a \le a_c \\ \frac{a_c}{a}(2 - \frac{a_c}{a}) & for\ a > a_c \end{cases} \tag{9.17}$$

a_c is around 0.2. Further, it is noted that the equations must be solved iteratively since the flow angle and thus also the angle of attack depend on the induced velocity itself. But the method described in this note is unsteady and thus time is used as relaxation, i.e. after the blades have in one time step moved an azimuthal angle of $\Delta\theta_{wing} = \omega\Delta t$ (assuming a small Δt), values from the previous time step are used on the right-hand side of Equations 9.13 and 9.14 for $\mathbf{W}$ when updating new values for the induced velocity. This can be done since the induced velocity changes relatively slowly in time due to dynamic wake model.

Dynamic wake model

To take into account the time delay before Equations 9.13 and 9.14 are in equilibrium with the aerodynamic loads, a dynamic inflow model must be applied. In two EU-sponsored projects (Snel and Schepers, 1995; Schepers and Snel, 1995) different engineering models were tested against measurements. One of these models, proposed by Øye, is a filter for the induced velocities consisting of two first order differential equations:

$$W_{\text{int}} + \tau_1 \frac{dW_{\text{int}}}{dt} = W_{qs} + k \cdot \tau_1 \frac{dW_{qs}}{dt} \tag{9.18}$$

$$W + \tau_2 \frac{dW}{dt} = W_{int} \tag{9.19}$$

W_{qs} is the quasi static value found by Equations 9.13 and 9.14, W_{int} an intermediate value and W the final filtered value to be used as the induced velocity. The two time constants are calibrated using a simple vortex method as:

$$\tau_1 = \frac{1.1}{(1-1.3a)} \cdot \frac{R}{V_o} \tag{9.20}$$

and:

$$\tau_2 = \left(0.39 - 0.26 \left(\frac{r}{R} \right)^2 \right) \cdot \tau_1 . \tag{9.21}$$

R is the rotor radius, k=0.6, and a is the axial induction factor defined for zero yaw as $a = W_n / |\mathbf{V_o}|$, or more generally can be estimated as:

$$a = \frac{|\mathbf{V_o}| - |\mathbf{V'}|}{|\mathbf{V_o}|} . \tag{9.22}$$

Using Equation 9.20, a is, however, not allowed to exceed 0.5. Equations 9.18 and 9.19 can be solved using different numerical techniques. The one suggested here is to assume that the right hand sides are constant, which allows them to be solved analytically, yielding the following algorithm

1 calculate W^i_{qs} using Equations 9.13 and 9.14;
2 estimate right hand side of Equation 9.18 using backward difference $H = W^i_{qs} + k \cdot \tau_1 \frac{W^i_{qs} - W^{i-1}_{qs}}{\Delta t}$;
3 solve Equation 9.18 analytically, $W^i_{\text{int}} = H + (W^{i-1}_{\text{int}} - H) \exp(\frac{-\Delta t}{\tau_1})$;
4 solve equation (9.19) analytically, $W^i = W^i_{\text{int}} + (W^{i-1} - W^i_{\text{int}}) \exp(\frac{-\Delta t}{\tau_2})$.

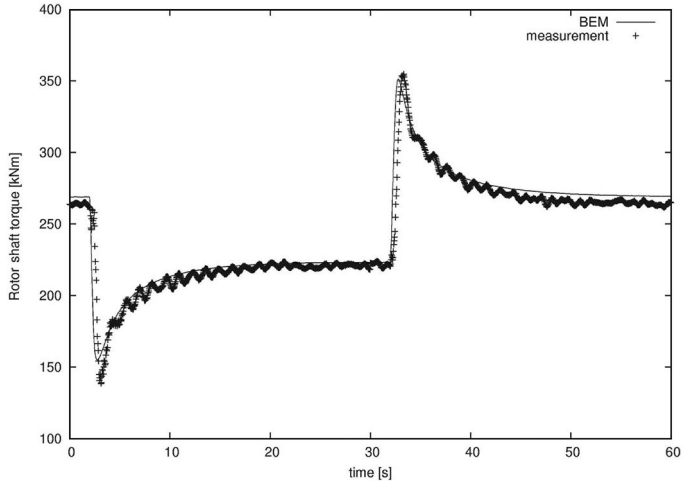

Figure 9.8 Comparison between measured and computed time series of the rotor-shaft torque for the Tjaereborg machine during a step input of the pitch for a wind speed of 8.7 m/s

Applying a dynamic filter for the induced velocity is necessary in order to capture the time behaviour of the loads and power when the thrust is changed by, e.g., pitching the blades. In Figure 9.8 the computed and measured response on the rotor-shaft torque for a sudden change of the pitch angle is shown for a 2MW machine. At t=2 s the pitch is increased from 0 to 3.7 degrees, decreasing the local angles of attack. First the torque drops from 260 kNm to 150 kNm and not until approximately 10 seconds later the induced velocities and thus the power has settled at a new equilibrium. At t=32 s the pitch is changed back to 0 degrees and a similar overshoot in the torque is observed. The decay of the spikes seen in Figure 9.8 can only be computed with a dynamic inflow model, and such a model is therefore of utmost importance for a pitch-regulated wind turbine.

Dynamic stall

The wind seen locally on a point on the blade changes constantly due to wind shear, yaw/tilt misalignment, tower passage and atmospheric turbulence. This has a direct impact on the angle of attack that changes dynamically during the revolution. The effect of changing the blades angle of attack will not appear instantaneously on the loads but will take place with a time delay proportional to the chord divided with the relative velocity seen at the blade section. The response on the aerodynamic load depends on whether the boundary layer is attached or partly separated. In the case of attached flow the time delay can be estimated using the Theodorsen theory for unsteady lift and aerodynamic moment (Theodorsen, 1935). For trailing-edge stall, i.e. when separation

starts at the trailing edge and gradually increases upstream at increasing angles of attack, the so-called dynamic stall can be modelled through a separation function, f_s, as described in (Øye, 1991), see later. The Beddoes–Leishman model (Leishman and Beddoes, 1989) further takes into account attached flow, leading edge separation and compressibility effects, and also corrects the drag and moment coefficients. For wind turbines, trailing edge separation is assumed to represent the most important phenomenon regarding dynamic airfoil data, but also effects in the linear region may be important (see Hansen et al. 2004). It has been shown by Øye (1991) that if a dynamic stall model is not used one might compute flapwise vibrations, especially for stall-regulated wind turbines, which do not exist on a real machine. For stability reasons it is thus highly recommended to at least include a dynamic stall model for the lift. For trailing-edge stall the degree of stall is described through f_s, as:

$$C_l = f_s C_{l,inv}(\alpha) + (1 - f_s) C_{l,fs}(\alpha), \tag{9.23}$$

where $C_{l,inv}$ denotes the lift coefficient for inviscid flow without any separation and $C_{l,fs}$ is the lift coefficient for fully separated flow, e.g., on a flat plate with a sharp leading edge. $C_{l,inv}$ is normally an extrapolation of the static airfoil data in the linear region, and in Hansen et al. (2004) one way of estimating $C_{l,fs}$ and f^{st}_s is shown. f^{st}_s is the value of f_s that reproduces the static airfoil data when applied in Equation 9.23. The assumption is that f_s always will try to get back to the static value as:

$$\frac{df_s}{dt} = \frac{f_s^{st} - f_s}{\tau} \tag{9.24}$$

that can be integrated analytically to give:

$$f_s(t + \Delta t) = f_s^{st} + (f_s(t) - f_s^{st}) \exp(-\frac{\Delta t}{\tau}). \tag{9.25}$$

τ is a time constant approximately equal to Ac/V_{rel}, where c denotes the local chord, and V_{rel} is the relative velocity seen by the blade section. A is a constant that typically takes a value about 4. Applying a dynamic stall model the airfoil data is always chasing the static value at a given angle of attack that is also changing in time. If, for example, the angle of attack is suddenly increased from below to above stall, the unsteady airfoil data contains for a short time some of the inviscid/unstalled value, $C_{l,inv}$, and an overshoot relative to the static data is seen. It can thus be seen as a model of the time needed for the viscous boundary layer to develop from one state to another. In Figure 9.9 is shown the result using the dynamic stall model for $\alpha = 15 + 2\sin(12.57 \cdot t)$ with a time constant t=0.08 s and the initial condition $f_s(0) = f_s^{st}$. It is seen that the mean slope of the lift curve, $dC_l / d\alpha$ becomes positive for the dynamic airfoil data in stall, which is beneficial for the stability.

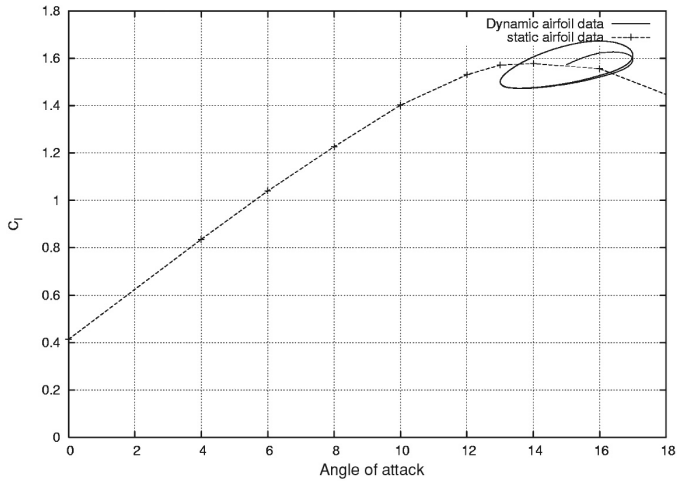

Figure 9.9 Example of the result using a dynamic stall model

Yaw/tilt model

If the rotor is yawed (and/or tilted), as shown in Figure 9.10, there will be an azimuthal variation of the induced velocity, so that the induced velocity is smaller when the blade is pointing upstream than when the same blade half a revolution later is pointing downstream.

The physical explanation of this is that a blade pointing downstream is deeper into the wake than a blade pointing upstream. This means that an upstream blade is subject to a higher wind and thus produces higher loads than the downstream blade, which produces a beneficial yawing moment that will try to turn the rotor more into the wind thus enhancing yaw stability. The yaw model describes the distribution of the induced velocity. If a yaw model is not included the BEM method will not be able to predict the restoring yaw moment. The following yaw model proposed by Glauert is also found in Snel and Schepers (1995).

$$\mathbf{W} = \mathbf{W}_o\left(1+\frac{r}{R}\tan\left(\frac{\chi}{2}\right)\cos(\theta_{wing}-\theta_o)\right), \tag{9.26}$$

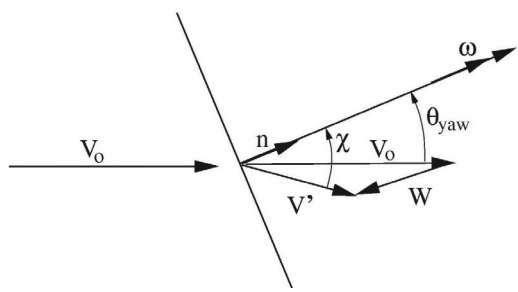

Figure 9.10 Yawed rotor disc in wind field

where the wake skew angle, χ, is defined as the angle between the wind velocity in the wake and the rotational axis of the rotor, see Figure 9.10. $\mathbf{W_0}$ is the mean induced velocity found by Equations 9.13 and 9.14 followed by 9.18 and 9.19. θ_o is the angle where the blade is deepest into the wake. The skew angle can be determined as:

$$\cos\chi = \frac{\mathbf{n}\cdot\mathbf{V}'}{|\mathbf{n}||\mathbf{V}'|}, \tag{9.27}$$

where $\mathbf{n}$ is the normal vector in the direction of the rotational axis, see Figure 9.10. The skew angle is assumed to be constant with the radius and can be computed at a radial position close to r/R=0.7.

The induced velocity is now known at the new azimuthal position at time $t+\Delta t$, $\theta_{wing}(t+\Delta t) = \theta_{wing}(t)+\omega\Delta t$. The angle of attack can thus be evaluated from Equation 9.10 and the lift, drag and moment coefficients can be determined from tabulated airfoil data. The normal, p_z, and tangential, p_y, loads can be determined from:

$$p_z = l\cos\phi + d\sin\phi \tag{9.28}$$

and:

$$p_y = l\sin\phi - d\cos\phi \tag{9.29}$$

where:

$$l = \tfrac{1}{2}\rho|\mathbf{V}_{\mathbf{rel}}|^2 cC_l \tag{9.30}$$

and

$$d = \tfrac{1}{2}\rho|\mathbf{V}_{\mathbf{rel}}|^2 cC_d \tag{9.31}$$

To summarize the unsteady BEM model:

- read geometry and run parameters;
- initialize the position and velocity of blades;
- discretize the blades into N elements;
- initialize the induced velocity;
  - for n=1 to max time step (t=$n\Delta t$);
  - for each blade;
  - for each element 1 to N.
- compute the relative velocity to the blade element from Equation 9.9 using old values for the induced velocity;
- calculate the flow angle and thus the angle of attack from Equations 9.10 and 9.11;
- determine static C_l and C_d from table look up;
- determine dynamic airfoil data using a dynamic stall model;
- calculate lift using Equation 9.30;
- compute the loads p_z and p_y using Equations 9.28 and 9.29;

- compute new equilibrium values for the induced velocity $W^{qs}{}_z$ and $W^{qs}{}_y$ using Equations 9.13 and 9.14;
- find the unsteady induced velocities, W_z and W_y, using a dynamic wake model;
- in case of yaw calculate the azimuthal variation from Equation 9.26 and compute the induced velocity for each blade.

In case of an aeroelastic computation, where the structure is not considered stiff, the loads p_z and p_y are used to determine a local blade velocity $\mathbf{V_b}$. This blade velocity must be taken into account when computing the relative velocity and Equation 9.9 should be extended to:

$$\begin{pmatrix} V_{rel,y} \\ V_{rel,z} \end{pmatrix} = \begin{pmatrix} V_y \\ V_z \end{pmatrix} + \begin{pmatrix} -\omega x \cos\theta_{cone} \\ 0 \end{pmatrix} + \begin{pmatrix} W_y \\ W_z \end{pmatrix} - \begin{pmatrix} V_{b,y} \\ V_{b,z} \end{pmatrix} \tag{9.32}$$

Deterministic model for wind

The time averaged atmospheric boundary layer shown in Figure 9.11 can be modelled as:

$$V_o(x) = V_o(H)\left(\frac{x}{H}\right)^{\nu}, \tag{9.33}$$

where H is the hub height, x the distance from the surface and ν a parameter giving the amount of shear. υ is typically in the range between 0.1 and 0.25.

The wind is also influenced by the presence of the tower. A simple model for the influence of the tower is to assume potential flow, see Figure 9.12.

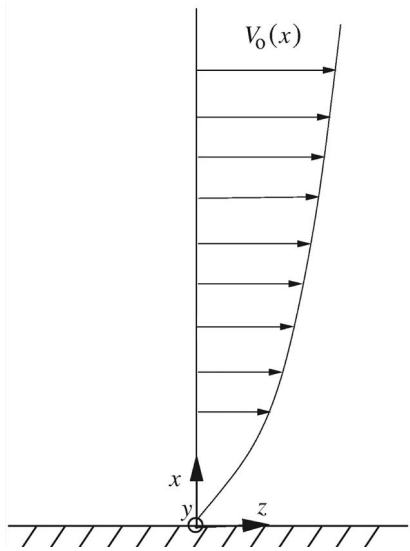

Figure 9.11 Deterministic wind velocity shear

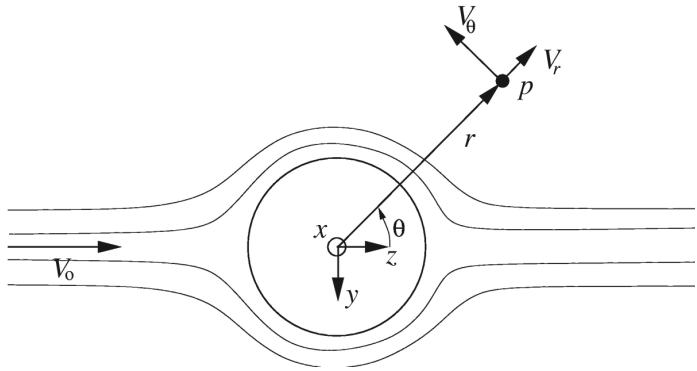

Figure 9.12 The effect of the tower

Coordinate system 1 is oriented so that the undisturbed wind velocity, V_o, is aligned with the z-axis. In a polar coordinate system as shown in Figure 9.12 the radial and tangential velocity components around the tower assuming potential flow can be computed as:

$$V_r = V_o\left(1-\left(\frac{a}{r}\right)^2\right)\cos\theta \tag{9.34}$$

and

$$V_\theta = -V_o\left(1+\left(\frac{a}{r}\right)^2\right)\sin\theta \tag{9.35}$$

where a here denotes the radius of the tower. Transforming the velocity to the Cartesian coordinate system 1 yields:

$$\begin{aligned} V_z &= V_r\cos\theta - V_\theta\sin\theta \\ V_y &= -V_r\sin\theta - V_\theta\cos\theta \end{aligned} \tag{9.36}$$

Following relation between r, θ and y, z can be used

$$\cos\theta = \frac{z}{r}$$

$$\sin\theta = -\frac{y}{r}$$

$$r = \sqrt{z^2+y^2}$$

It is noted that assuming potential flow is a bad approximation for a downwind machine, where each blade passes the tower wake once every evolution. Further, the turbulent part of the real atmosphere wind should be added for a realistic time simulation of a wind turbine.

References

Bramwell, A.R.S. (1976) *Helicopter Dynamics*, London: Edward Arnold.

Hansen, M.H., Gaunaa, M. and Madsen, H.A. (2004) *A Beddoes–Leishman Type Dynamic Stall Model in State-space and Indicial Formulations* Risø-R-1354(EN). Roskilde: Risø National Laboratory.

Leishman, J.G. and Beddoes, T.S. (1989) 'A semi-empirical model for dynamic stall' *Journal of the American Helicopter Society*, 34(3), pp 3–17.

Øye, S. (1991) 'Dynamic stall, simulated as a time lag of separation' in K.F. McAnulty (ed) *Proceedings of the 4th IEA Symposium on the Aerodynamics of Wind Turbines*, ETSU-N-118. Harwell: ETSU Harwell Laboratory.

Schepers, J.G. and Snel, H. (1995) *Dynamic Inflow: Yawed Conditions and Partial SpanPitch Control,* ECN-C-95-056. Internal ECN document.

Snel, H. and Schepers, J.G. (1995) *Joint Investigation of Dynamic Inflow Effects and Implementation of an Engineering Method,* ECN-C-94-107. Internal ECN document.

Theodorsen, T. (1935) *General Theory of Aerodynamic Instability and the Mechanism of Flutter,* NACA report 496. pp. 413–433. Hampton, VA: NACA.

10 Introduction to loads and structures

After having described in detail how to calculate the aerodynamic loads on a wind turbine, the following material concerns structural issues to ensure that the construction will not break down during its typical design lifetime of 20 years. Normally a breakdown is caused by an inadequate control system, extreme wind conditions, fatigue cracks or a defective safety system. A very dangerous breakdown may occur if the power to the generator is lost. There is then no braking torque on the rotor which, in the absence of a safety system such as mechanical or aerodynamic emergency brakes, is free to accelerate. Because the aerodynamic forces increase with the square of the rotor speed, the blades will bend more and more in the downwind direction and might end up hitting the tower or flying off due to centrifugal forces. It has been estimated (Sørensen, 1983) that blades sheared from an over-speeding wind turbine can land up to about 300 metres from the tower. Fortunately, violent failures are extremely rare and no humans have, to the author's knowledge, ever been reported to have suffered injuries from debris flying off a wind turbine. Safety standards, such as (IEC 61400, 2004), exist to ensure that wind turbines operate safely. The standards define load cases, such as extreme gusts, which a wind turbine must be able to survive. Lightning is also known to have caused disintegration of blades.

Fatigue is a very important issue in a wind turbine construction, which is built to run for a minimum of 20 years, and thus performs in the order of 10^9 revolutions. To estimate the loads on a wind turbine throughout its entire lifetime, the loads and hence the stresses in the material must either be computed using an aeroelastic code in a realistic wind field including turbulence or be measured directly on an existing turbine. Once the dynamic stresses are known, it is possible to calculate the fatigue damage using standard methods such as the Palmgren–Miner rule.

Description of main loads

In order that the following material can be better understood, a short description of the main loads on a horizontal-axis wind turbine is given. To extract energy from the wind it is necessary to slow down the wind speed using a force pointing

in the upwind direction. This force is called the thrust and is caused by an increase in the pressure over the rotor, induced by the flow past the individual rotor blades. The total load has not only a component normal to the flow, but also a tangential component in the rotational direction of the blades. The tangential load component delivers the shaft torque that turns the rotor. To characterize these loads it is common to state the flapwise and the edgewise bending moments at a position close to the root of the blades together with the tilt rotor moment and yaw rotor moment in the shaft between the rotor and the first bearing. The flapwise bending moment M_{flap}, see Figure 10.1, stems from the normal forces (thrust), which tend to deflect the blades out of the rotor plane in the downwind direction

$$M_{flap}(r_{pos}) = \int_{r_{pos}}^{R} r p_N(r) dr \tag{10.1}$$

where p_N is the normal force per length, r the local radius, R the total radius of the rotor and dr an incremental part of the blade. The edgewise bending moment is the bending moment in the rotor plane from the tangential force distribution. The edgewise bending moment is sometimes referred to as the lead-lag moment.

The tilt rotor moment in the main shaft, seen in Figure 10.1, tries to tilt the nacelle over the tower. The yaw rotor moment tries to turn the nacelle on the tower. Sometimes also the two bending moments at the root of the tower is stated. In Figure 10.2 is shown an example of computed loads using the aeroelastic code FLEX4 at a mean wind speed of 11m/s. The wind speed at hub height and the power output are seen on the first two graphs. The last four graphs show the corresponding time histories of the flapwise and edgewise

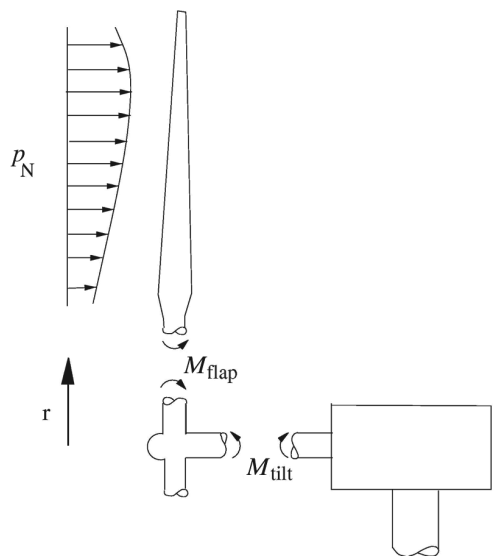

Figure 10.1 Some main loads on a horizontal-axis wind turbine

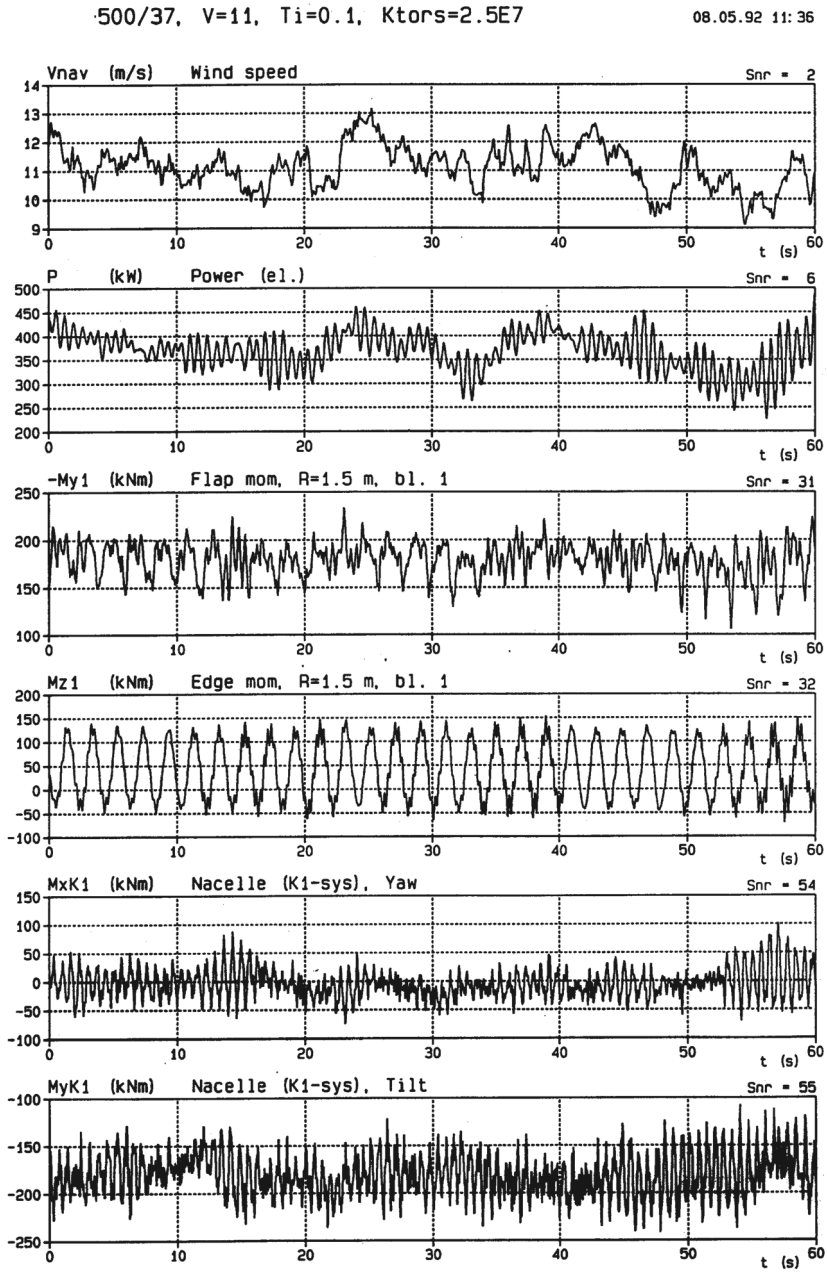

Figure 10.2 Example of computed loads using FLEX4 for a mean wind speed of 11m/s

bending moments and the tilt rotor and yaw rotor moments. The effect of gravity is clearly seen on the edgewise bending moment as a sinusoidal variation superimposed some small high frequency signal stemming from atmospheric turbulence. The flapwise bending is mostly influenced by the aerodynamic loads that vary with the turbulent wind field and this signal is therefore more stochastic.

References

IEC (2004) 'Wind Turbines. Part 1: Design requirements' 61400-1 Ed.3 CD. Second revision IEC TC88-MT1. Geneva: IEC.

Sørensen, J.N. (1983) 'Beregning af banekurver og kastelængder for afrevne vindmøllevinger' (in Danish), Department of Fluid Mechanics DTU, AFM83-06. Internal DTU report.

11 Beam theory for wind turbine blades

This chapter describes how a blade, where the outer contour is designed from aerodynamical considerations, is constructed to be sufficiently strong and stiff. In the past, materials like wood, steel, aluminium, glass-fibre reinforced plastics (GFRP) and carbon-fibre reinforced plastics (CFRP) have been used. The choice depends on many parameters such as strength, weight, stiffness, price, and – very important for wind turbines – fatigue properties. The majority of wind turbine blades are constructed using GRPs and, therefore, a short description of a manufacturing process using this material is given. A negative mould for the upper part (suction side) and lower part (pressure side) of the blade is made. A thin film of so-called gelcoat is first laid in the moulds. The gelcoat gives a smooth white finish to the blades and therefore it is not necessary to paint the blades afterwards. Then a number of glass fibre mats are laid in. On each mat a layer of epoxy or polyester is rolled on to bind the mats into a hard matrix of fibres. The number of mats gives the thickness of the shell and typically a thin shell is made around the leading and trailing edge and a thick shell is made in the middle of the airfoil. A section of such a blade is seen in Figure 11.1.

To make the blade stronger and stiffer, so-called webs are glued on between the two shells before they are glued together. To make the trailing edge stiffer, foam panels can also be glued on before assembling the upper and lower parts. Because such a construction consists of different layers it is often called a sandwich construction, and a principal sketch is drawn in Figure 11.2 which can readily be compared to the real section in Figure 11.1. It is seen that the thick layer of mats and epoxy in the middle of the skin and the webs form a boxlike structure. For structural analysis, the boxlike structure, which is the most important structural part of the blade, acts like a main beam on which a thin skin is glued defining the

Figure 11.1 Section of an actual blade

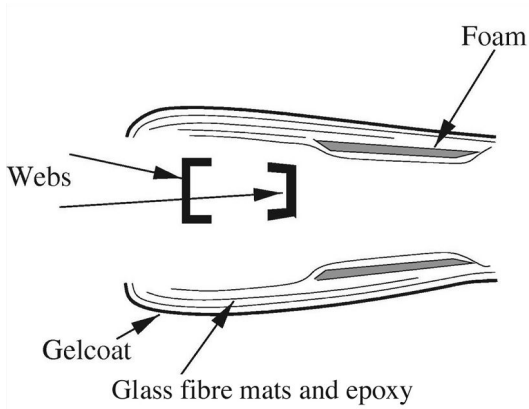

Figure 11.2 Schematic drawing of a section of a blade

geometry of the blade. Fixing a thin skin on a main beam is an alternative way, which is sometimes used, to construct a blade.

A blade can thus be modelled as a beam and when the stiffnesses EI and GI_v at different spanwise stations are computed, simple beam theory can be applied to compute the stresses and deflections of the blade. E is the modulus of elasticity, G is the modulus of elasticity for shear and I denote different moments of inertia. In the next section a more elaborate explanation is given for the moments of inertia and it is shown how the stiffnesses can be computed for a wind turbine blade as the one shown in Figure 11.1.

The simple beam theory described here is found in almost any basic book on mechanics of materials e.g. Timoshenko and Gere (1972). Further, it is outlined how to compute the important structural parameters shown in Figure 11.3. Values of these parameters are necessary to compute the deflection of a blade for a given load or as input to a dynamic simulation using an aeroelastic code.

EI_1	Bending stiffness about first principal axis.
EI_2	Bending stiffness about second principal axis.
GI_v	Torsional stiffness.
χ_E	The distance of the point of elasticity from the reference point.
χ_m	The distance of the centre of mass from the reference point.
χ_s	The distance of the shear centre from the reference point.
β	The twist of the airfoil section measured relative to the tip chordline.
υ	Angle between chordline and first principal axis.
$\beta+\upsilon$	Angle between tip chordline and first principal axis.

The point of elasticity is defined as the point where a normal force (out of the plane) will not give rise to a bending of the beam. The shear centre is the point where an in-plane force will not rotate the airfoil. If the beam is bent about one of the principal axes the beam will only bend about this axis. As

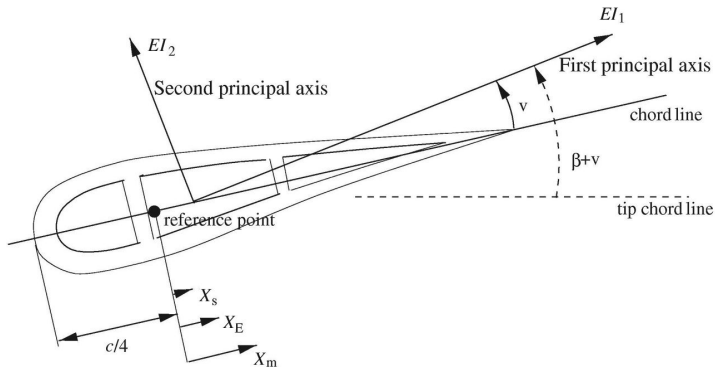

Figure 11.3 Section of a blade showing the main structural parameters; see the text for an explanation of the variables

shall be seen later, it is convenient to use the principal axes when calculating the blade deflection.

Before continuing, some necessary definitions must be introduced. The following quantities are defined in terms of the reference coordinate system (X_R, Y_R) in Figure 11.4:

Longitudinal stiffness: $[EA] = \int_A E dA$.

Moment of stiffness about the axis X_R: $\left[ES_{X_R}\right] = \int_A EY_R dA$.

Moment of stiffness about the axis Y_R: $\left[ES_{Y_R}\right] = \int_A EX_R dA$.

Moment of stiffness inertia about the axis X_R: $\left[EI_{X_R}\right] = \int_A EY_R^2 dA$.

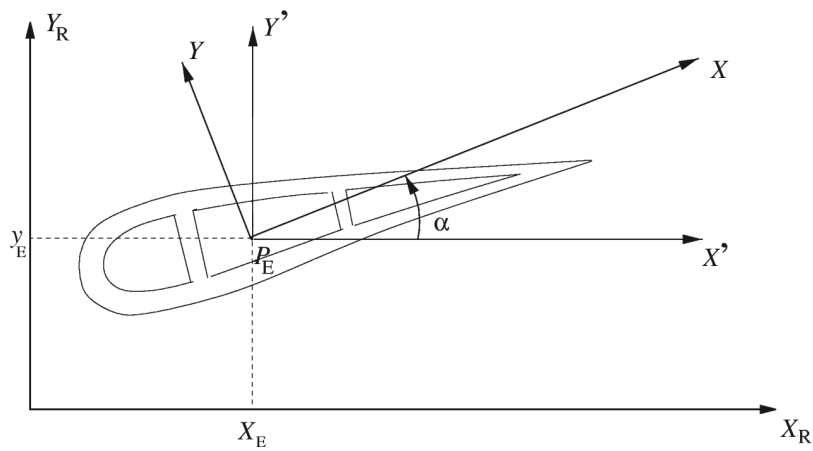

Figure 11.4 Section of a blade

Moment of stiffness inertia about the axis Y_R: $\left[EI_{Y_R}\right] = \int_A E\mathcal{X}_R^2 dA.$

Moment of centrifugal stiffness: $\left[ED_{\mathcal{X}Y_R}\right] = \int_A E\mathcal{X}_R Y_R dA.$

From these definitions, the point of elasticty P_E=($\mathcal{X}_E$,Y_E) can be computed in the reference system ($\mathcal{X}_R$,Y_R) as:

$$\mathcal{X}_E = \frac{\left[ES_{Y_R}\right]}{\left[EA\right]} \tag{11.1}$$

and:

$$Y_E = \frac{\left[ES_{\mathcal{X}_R}\right]}{\left[EA\right]} \tag{11.2}$$

For E and ρ constant the point ($\mathcal{X}_E$,Y_E) equals the centre of mass for the section, where ρ denotes the density of the material used. Now the moments of stiffness inertia and the moment of centrifugal stiffness are moved to the coordinate system ($\mathcal{X}$',Y'), which is parallel to the reference system ($\mathcal{X}_R$,Y_R) and has its origin in the point of elasticity, using the formulas:

$$\left[EI_{\mathcal{X}'}\right] = \int_A E(Y')^2 dA = \left[EI_{\mathcal{X}_R}\right] - Y_E^2\left[EA\right] \tag{11.3}$$

$$\left[EI_{Y'}\right] = \int_A E(\mathcal{X}')^2 dA = \left[EI_{Y_R}\right] - \mathcal{X}_E^2\left[EA\right] \tag{11.4}$$

$$\left[ED_{\mathcal{X}'Y'}\right] = \int_A E\mathcal{X}'Y' dA = \left[ED_{\mathcal{X}Y_R}\right] - \mathcal{X}_E Y_E\left[EA\right] \tag{11.5}$$

It is now possible to compute the angle α between $\mathcal{X}$' and the first principal axis and the bending stiffness about the principal axes. The second principal axis is perpendicular to the first principal axis:

$$\alpha = \tfrac{1}{2}\tan^{-1}\left(\frac{2\left[ED_{\mathcal{X}'Y'}\right]}{\left[EI_{Y'}\right] - \left[EI_{\mathcal{X}'}\right]}\right) \tag{11.6}$$

$$\left[EI_1\right] = \left[EI_{\mathcal{X}'}\right] - \left[ED_{\mathcal{X}'Y'}\right]\tan\alpha \tag{11.7}$$

$$\left[EI_2\right] = \left[EI_{Y'}\right] + \left[ED_{\mathcal{X}'Y'}\right]\tan\alpha \tag{11.8}$$

The stress σ(x,y) in the cross section from the bending moments about the two principal axes $M_{\mathcal{X}}$ and M_Y and the normal force N is found from:

$$\sigma(x,y) = E(x,y)\varepsilon(x,y), \tag{11.9}$$

where the strain ε is computed from:

Table 11.1 Main structural parameters for the Tjaereborg blade

r [m]	EA [GN]	EI_1 [MNm²]	EI_2 [MNm²]	GI_v [MNm²]	M [kg/m]	X_E [mm]	X_m [mm]	X_s [mm]	v [o]	β+v [o]
1.8	36.0	12000	12000	7500	1700	0	0	0	0	0
3.0	6.14	1630	1725	362	330	2	2	0	5.4	14.4
4.5	5.82	1080	1940	328	389	54	159	11	0.94	9.44
6.0	5.10	623	1490	207	347	59	165	13	1.30	9.30
9.0	4.06	255	905	92.8	283	63	170	18	1.09	8.09
12.0	3.33	129	557	47.7	235	58	158	15	0.86	6.86
15.0	2.76	64.8	349	24.7	196	51	137	15	0.86	5.86
18.0	2.33	32.4	221	12.9	166	45	121	16	0.91	4.91
21.0	1.83	15.2	131	6.23	172	41	110	17	0.83	3.83
24.0	1.21	6.04	65.7	2.57	90.3	40	102	16	0.63	2.63
27.0	0.63	1.82	28.1	0.84	52.6	47	108	14	0.16	1.16
30.0	0.21	0.32	9.5	0.18	24.2	82	136	10	–0.52	–0.52

$$\varepsilon(x,y) = \frac{M_1}{[EI_1]}y - \frac{M_2}{[EI_2]}x + \frac{N}{[EA]}. \tag{11.10}$$

σ, ε and N are positive for tension and negative for compression. The bending moments M_1 and M_2 and the normal force N are computed from the loading of the blade as is shown later.

The main structural data are now determined. Since a wind turbine blade is very stiff in torsion the torsional deflection is normally not considered. A complete description of how to compute the shear centre and the torsional rigidity is, however, given in Øye (1978). Example results from Øye (1988) for the 30m blade used at the 2MW Tjæreborg wind turbine is listed in Table 11.1.

Table 11.1 shows that the position of the first principal axis, described by the angle β+v, varies with the radius r. It is also seen that the position of the first principle axis is almost identical with the chord line since the angle v is small for most of the blade.

Deflections and bending moments

A wind turbine blade as in Figure 11.5 can be treated as a technical beam as shown in Figure 11.6.

If the external loadings p_y and p_z are known along the blade. the shear forces T_z and T_y and bending moments M_y and M_z can be found as:

$$\frac{dT_z}{dx} = -p_z(x) + m(x)\ddot{u}_z(x) \tag{11.11}$$

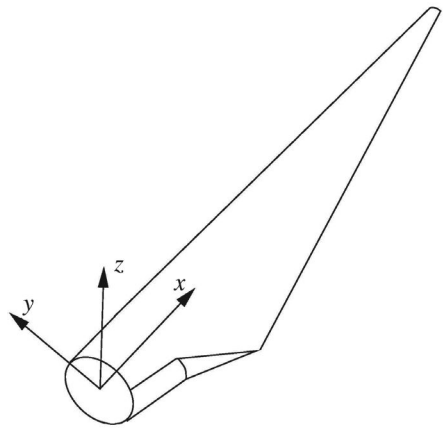

Figure 11.5 Wind turbine blade. Note that the coordinate system used for the blade is different from the one shown in Figure 11.4

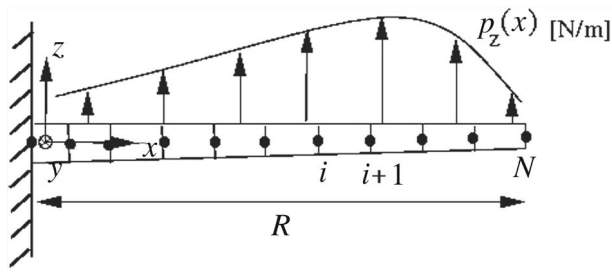

Figure 11.6 Technical beam

$$\frac{dT_y}{dx} = -p_y(x) + m(x)\ddot{u}_y(x) \tag{11.12}$$

$$\frac{dM_y}{dx} = T_z \tag{11.13}$$

$$\frac{dM_z}{dx} = -T_y \tag{11.14}$$

Equations 11.11 to 11.14 can be derived using Newton's second law on an infinitesimal piece of the beam as shown in Figure 11.7. $\ddot{u}$ is the acceleration and if the blade is in equilibrium the last term (inertia term) on the right hand side of Equations 11.11 and 11.12 are zero.

The bending moments can now be transformed to the principal axes as (here the y-axis is aligned with the tip chord):

$$M_1 = M_y \cos(\beta + v) - M_z \sin(\beta + v) \tag{11.15}$$

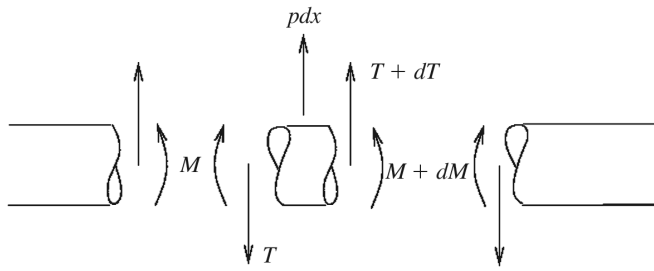

Figure 11.7 Infinitesimal piece of the beam

$$M_2 = M_y \sin(\beta + v) + M_z \cos(\beta + v) \tag{11.16}$$

where β+v is the angle between the *y*-axis and the first principal axis as shown in Figure 11.8. If nothing else is known it can be assumed that the first principal axis lies along the chordline, which is only true for a symmetric airfoil. Note that β is negative for a normally twisted blade, but is assumed positive in Equations 11.15, 11.16, 11.19 and 11.20.

The curvatures about the principal axes are from simple beam theory:

$$\kappa_1 = \frac{M_1}{EI_1} \tag{11.17}$$

$$\kappa_2 = \frac{M_2}{EI_2} \tag{11.18}$$

These curvatures are then transformed back to the *y*-axis and *z*-axis as:

$$\kappa_z = -\kappa_1 \sin(\beta + v) + \kappa_2 \cos(\beta + v) \tag{11.19}$$

$$\kappa_y = \kappa_1 \cos(\beta + v) + \kappa_2 \sin(\beta + v) \tag{11.20}$$

The angular deformations and thus the deflections are now calculated from:

$$\frac{d\theta_y}{dx} = \kappa_y \tag{11.21}$$

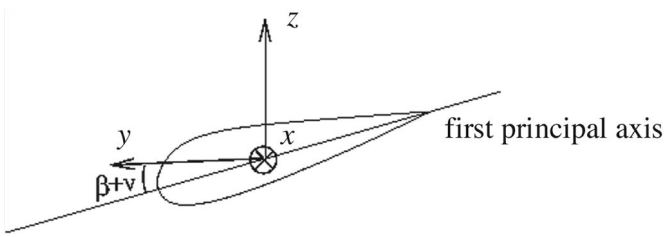

Figure 11.8 Orientation of principal axes

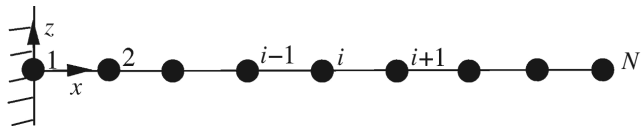

Figure 11.9 Discretized cantilever beam

$$\frac{d\theta_z}{dx} = \kappa_z \tag{11.22}$$

$$\frac{du_z}{dx} = -\theta_y \tag{11.23}$$

$$\frac{du_y}{dx} = \theta_z \tag{11.24}$$

If the loads are given in discrete points as shown in Figure 11.9 and the loads are assumed to vary linearly between two points i and i+1, then Equations 11.11 to 11.14 and Equations 11.21 to 11.24 can be integrated to give the following numerical algorithm to calculate bending moments and deflections.

Numerical algorithm for determining the bending moments and deflection

Boundary conditions: $T_y^N = 0$ and $T_z^N = 0$

For i=N to 2

$$T_y^{i-1} = T_y^i + \tfrac{1}{2}(p_y^{i-1} + p_y^i)(x^i - x^{i-1}) \tag{11.25}$$

$$T_z^{i-1} = T_z^i + \tfrac{1}{2}(p_z^{i-1} + p_z^i)(x^i - x^{i-1}) \tag{11.26}$$

Boundary conditions: $M_y^N = 0$ and $M_z^N = 0$

For i=N to 2

$$M_y^{i-1} = M_y^i - T_z^i(x^i - x^{i-1}) - (\tfrac{1}{6}p_z^{i-1} + \tfrac{1}{3}p_z^i)(x^i - x^{i-1})^2 \tag{11.27}$$

$$M_z^{i-1} = M_z^i + T_y^i(x^i - x^{i-1}) + (\tfrac{1}{6}p_y^{i-1} + \tfrac{1}{3}p_y^i)(x^i - x^{i-1})^2 \tag{11.28}$$

For all points calculate M_1 and M_2 using Equations 11.15 and 11.16. Then κ_y and $k\kappa_z$ are computed using Equations 11.17, 11.18, 11.19 and 11.20.

Boundary conditions: $\theta_y^1 = 0$ and $\theta_z^1 = 0$

For i=1, N–1

$$\theta_y^{i+1} = \theta_y^i + \tfrac{1}{2}(\kappa_y^{i+1} + \kappa_y^i)(x^{i+1} - x^i) \tag{11.29}$$

$$\theta_z^{i+1} = \theta_z^i + \tfrac{1}{2}(\kappa_z^{i+1} + \kappa_z^i)(x^{i+1} - x^i) \tag{11.30}$$

Boundary conditions: $u_y^1 = 0$ and $u_z^1 = 0$

For i=1, N–1

$$u_y^{i+1} = u_y^i + \theta_z^i(x^{i+1} - x^i) + (\tfrac{1}{6}\kappa_z^{i+1} + \tfrac{1}{3}\kappa_z^i)(x^{i+1} - x^i)^2 \tag{11.31}$$

$$u_z^{i+1} = u_z^i - \theta_y^i(x^{i+1} - x^i) - (\tfrac{1}{6}\kappa_y^{i+1} + \tfrac{1}{3}\kappa_y^i)(x^{i+1} - x^i)^2 \tag{11.32}$$

The boundary conditions are for a cantilever beam, and the inertia terms in Equations 11.11 and 11.12 have been neglected for simplicity, but must be added for an unsteady computation.

A method to estimate the first flapwise, first edgewise and second flapwise eigenmodes

Equations 11.25 to 11.32 can also be used to estimate the first few eigenmodes. An eigenmode is a free vibration without the presence of external loads, i.e. Equations 11.11 and 11.12 become:

$$\frac{dT_z}{dx} = m(x)\ddot{u}_z(x) \tag{11.33}$$

$$\frac{dT_y}{dx} = m(x)\ddot{u}_y(x) \tag{11.34}$$

Since for an eigenmode the deflection is of the type $u = A\sin(\omega t)$ the acceleration is proportional to the deflection as:

$$\ddot{u} = -\omega^2 u \tag{11.35}$$

where ω is the associated eigenfrequency. Using Equation 11.35, Equations 11.33 and 11.34 become:

$$\frac{dT_z}{dx} = -m(x)\omega^2 u_z(x) \tag{11.36}$$

$$\frac{dT_y}{dx} = -m(x)\omega^2 u_y(x) \tag{11.37}$$

Comparing Equations 11.11 and11.12 to Equations 11.36 and 11.37 it is seen that an eigenmode can be found using the static beam equations when putting the external loads to:

$$p_z = m(x)\omega^2 u_z(x) \tag{11.38}$$

$$p_y = m(x)\omega^2 u_y(x) \tag{11.39}$$

Since the deflections in Equations 11.38 and 11.39 are not known, the equations must be solved iteratively that will converge to the mode with the lowest eigenfrequency, which is denoted the first flapwise mode. First, an initial deflection can be found using, for example, a constant loading for both the z and y directions. With this deflection the eigenfrequency is estimated at the tip as:

$$\omega^2 = \frac{p_z^N}{u_z^N m^N} \tag{11.40}$$

and a new loading is computed in all discrete points as:

$$p_z^i = \omega^2 m^i \frac{u_z^i}{\sqrt{(u_z^N)^2 + (u_y^N)^2}} \tag{11.41}$$

$$p_y^i = \omega^2 m^i \frac{u_y^i}{\sqrt{(u_z^N)^2 + (u_y^N)^2}} \tag{11.42}$$

Note that the loading is normalized with the tip deflection to ensure that the tip deflection becomes 1 in the next iteration. A new deflection is now computed using the loading from Equations 11.41 and 11.42. The procedure is repeated a few times until the eigenfrequency ω becomes constant. Now the deflection shape, u_z^{1f} and u_y^{1f} of the first flapwise eigenmode as shown in Figure 11.10 is known.

To find the first edgewise deflection the same procedure can be used again. However, some modification is needed to enforce the method *not* to converge towards the first flapwise mode. Every time a new deflection, $u_y(x)$ and $u_z(x)$, is computed it is necessary to subtract the part that contains the first flapwise mode:

$$u_z^{1e} = u_z - const_1 \cdot u_z^{1f} \tag{11.43}$$

$$u_y^{1e} = u_y - const_1 \cdot u_y^{1f} \tag{11.44}$$

To determine the constant, the following orthogonality constraint must be satisfied:

$$\int_0^R u_z^{1f} m u_z^{1e} dx + \int_0^R u_y^{1f} m u_y^{1e} dx = 0 \tag{11.45}$$

Combining Equations 11.43 and 11.44 with Equation 11.45 yields an expression for the constant:

$$const_1 = \frac{\int_0^R u_z^{1f} m u_z dx + \int_0^R u_y^{1f} m u_y dx}{\int_0^R u_z^{1f} m u_z^{1f} dx + \int_0^R u_y^{1f} m u_y^{1f} dx} \tag{11.46}$$

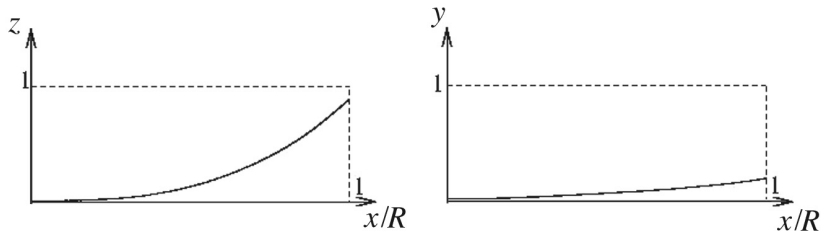

Figure 11.10 First flapwise eigenmode (1f)

Thus to enforce the method to converge to the first edgewise eigenmode it is necessary each time a new deflection has been computed to remove the part from the first flapwise eigenmode using Equations 11.43, 11.44 and 11.46. After a few iterations the deflection shape of the first edgewise eigenmode, u_z^{1e} and u_y^{1e}, as shown in Figure 11.11, is known.

Finally, the second flapwise eigenmode can be found in the same way. Now it is also necessary to subtract not only the part that contains the first flapwise eigenmode but also the part from the first edgewise eigenmode, using the following orthogonality constraint:

$$\int_0^R u_z^{1e} m u_z^{2f} dx + \int_0^R u_y^{1e} m u_y^{2f} dx = 0 \tag{11.47}$$

Each time a new deflection has been computed, Equations 11.43, 11.44 and 11.46 are used to remove the part from the first flapwise eigenmode. Next, Equations 11.48, 11.49 and 11.50 are applied to remove the part from the first edgewise eigenmode fulfilling constraint Equation 11.47:

$$u_z^{2f} = u_z - const_2 \cdot u_z^{1e} \tag{11.48}$$

$$u_y^{2f} = u_y - const_2 \cdot u_y^{1e} \tag{11.49}$$

$$const_2 = \frac{\int_0^R u_z^{1e} m u_z dx + \int_0^R u_y^{1e} m u_y dx}{\int_0^R u_z^{1e} m u_z^{1e} dx + \int_0^R u_y^{1e} m u_y^{1e} dx} \tag{11.50}$$

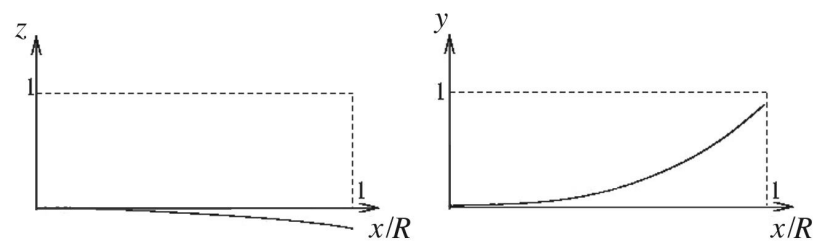

Figure 11.11 First edgewise eigenmode (1e)

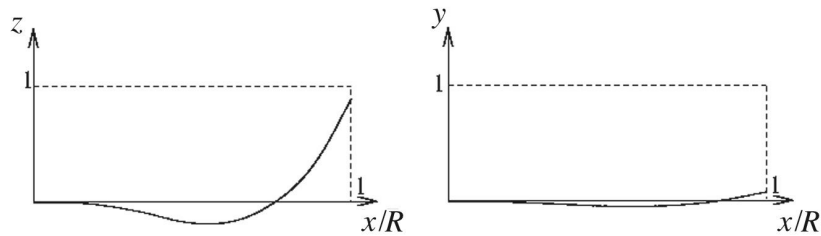

Figure 11.12 Second flapwise eigenmode (2f)

After a few iterations the deflection shape of the second flapwise eigenmode, u_z^{2f} and u_y^{2f}, as shown in Figure 11.12, is known.

The eigenmode estimation can be checked by comparing with the analytical solutions for a cantilever beam with constant values along the beam as given. for example, in Craig (1981):

$$\omega_1 = \frac{3.516}{L^2}\left(\frac{EI}{m}\right)^{1/2} \tag{11.51}$$

$$\omega_2 = \frac{22.03}{L^2}\left(\frac{EI}{m}\right)^{1/2} \tag{11.52}$$

ω_1, and ω_2 are the first and second eigenfrequencies respectively, and L is the length of the beam. Applying this algorithm on a beam with constant stiffness EI=1Nm^2, a mass distribution m=1kg/m, a length L=1m and using 11 points yields: ω_1=3.513 rad/s, which is close to the analytical solution of 3.516 rad/s. Using 11 points, the second eigenfrequency becomes 22.273 rad/s and 22.044 rad/s for 51 points, which should be compared to the analytical value of 22.03 rad/s. The solution for 51 points is shown in Figure 11.13.

In an accurate computation the effect of the centrifugal force on a deflected blade must be included. In Figure 11.14, the total force F_x from the centrifugal acceleration at r=x is shown.

F_x can be computed by integrating the incremental contribution dF_x from x to the tip of the blade R.

$$F_x = \int_x^R dF_x = \int_x^R x'\omega^2 m dx' \tag{11.53}$$

where ω is the angular velocity of the rotor, m the mass per length, dx' an incremental part of the blade and x' the radial distance to the incremental part. The projection of F_x normal to the rotor blade (see Figure 11.14) is:

$$F_c = F_x \sin\theta \approx F_x\theta \tag{11.54}$$

This force corresponds to a loading p_c (force per length)

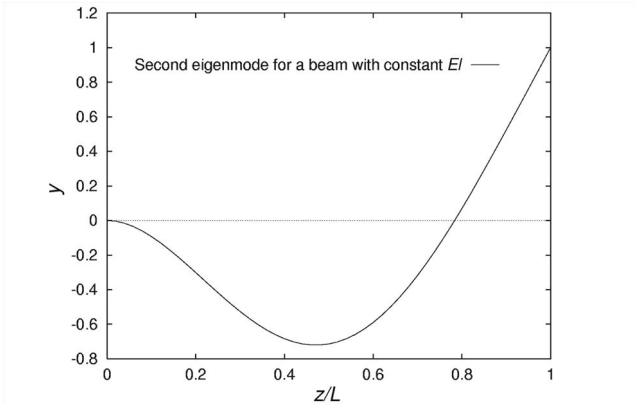

Figure 11.13 Second eigenmode using 50 elements

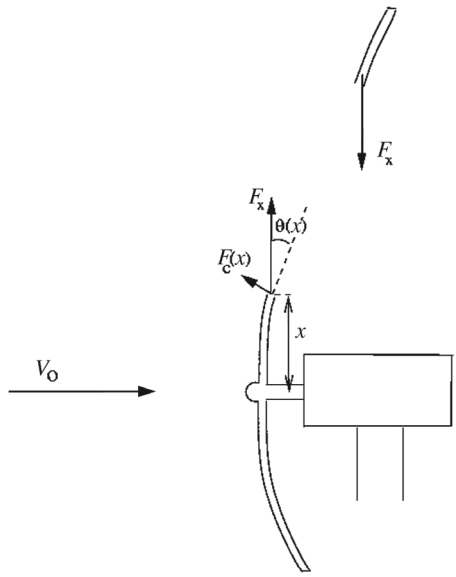

Figure 11.14 Total centrifugal force F_x at a spanwise position x

$$p_c = \frac{dF_c}{dx} = F_x \frac{d\theta}{dx} + \theta \frac{dF_x}{dx} \tag{11.55}$$

F_x decreases for increasing x, thus $dF_x / dx = -x\omega^2 m$ and Equation 11.55 becomes

$$p_c = F_x \frac{d\theta}{dx} - mx\omega^2\theta \tag{11.56}$$

The extra loading from Equation 11.56 should be added to the load calculated from the aerodynamics, and the net result is a redistribution of the loading, which

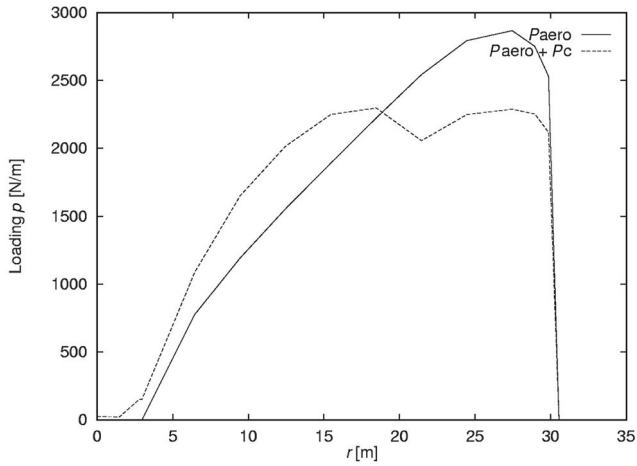

Figure 11.15 The computed load about the first principal axis for the 2MW Tjæreborg machine at V_o=10m/s with and without the centrifugal loading. p_{aero} is the aerodynamic load computed by BEM method and p_{aero} +p_c is the aerodynamic plus the centrifugal load

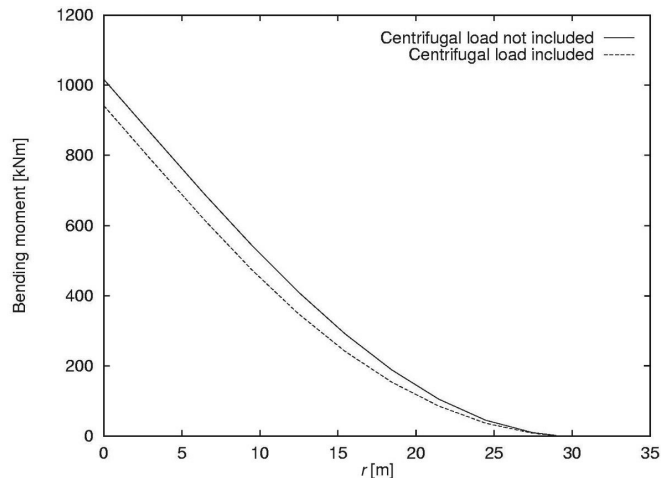

Figure 11.16 The computed bending moment about the first principal axis for the 2MW Tjæreborg machine at V_o =10m/s with and without the centrifugal loading

results in a reduction in the flapwise bending moment. Since p_c is a function of the angular deformation θ and the curvature $d\theta/dx$, which again is a function of the loads, it is necessary to iterate a few times in order to have the deflection including the effect of the centrifugal acceleration. That is, first the deflections and the angular deformations are computed by using only the aerodynamic loads. Then the extra loading is computed using Equations 11.53 and 11.56. A new loading is found by adding this extra loading to the original aerodynamic loading,

and a new set of deflections and angular deformations are computed. Hereafter the centrifugal loading is calculated again using Equation 11.56 and the procedure is repeated a few times until a stationary solution is found. In Figure 11.15 the effect of including the centrifugal loading on the 2MW Tjæreborg machine at a wind speed of 10m/s is shown. It is seen that the centrifugal loading reduces the loads at the tip but increases the loads at the root. The corresponding reduction in the bending moments is seen in Figure 11.16.

References

Craig, R.R. (1981) *Structural Dynamics*, Chichester: John Wiley & Sons.

Øye, S. (1978) 'Beregning af tværsnitskonstanter for bjælker med inhomogent tværsnit' (in Danish), AFM notat VK-45-781201. Internal DTU report.

Øye, S. (1988) 'Projekt K 30m Glasfibervinge, Teknisk beskrivelse' (in Danish), AFM 88-12. Internal DTU report.

Timoshenko, S.T. and Gere, J.M. (1972) *Mechanics of Materials*, New York: van Nostrand Reinhold Company.

12 Dynamic structural model of wind turbines

The main purpose of a structural model of a wind turbine is to be able to determine the temporal variation of the material loads in the various components to estimate the fatigue damage. Further, a dynamic system is used when analysing the stability of the wind turbine design, including perhaps the control system. To calculate in the time domain the deflections and velocities of the various components in the wind turbine a structural model including the inertia terms is needed. Then the dynamic structural response of the entire construction can be solved subject to the time-dependent load found using an aerodynamic model, such as the BEM method. For offshore wind turbines wave loads and perhaps ice loads on the bottom of the tower must also be estimated. One way of setting up the structural model based on the principle of virtual work is presented in detail. However, more formal finite element methods have also been used in different aeroelastic codes. The velocity of the vibrating wind turbine construction must be subtracted when calculating the relative velocity seen locally by the blade as shown in Equation 9.32. The loads therefore depend on the deflections and velocities of the structure, which again depends on the loads. The structural and aerodynamic models are therefore highly coupled and must be solved together in what is known as an aeroelastic problem.

Principle of virtual work and use of modal shape functions

The principle of virtual work is a method to set up the correct mass matrix, **M**, stiffness matrix, **K**, and damping matrix, **C**, for a discretized mechanical system as:

$$\mathbf{M}\ddot{\mathbf{x}} + \mathbf{C}\dot{\mathbf{x}} + \mathbf{K}\mathbf{x} = \mathbf{F}_g, \tag{12.1}$$

where, $\mathbf{F}_g$, denotes the generalized force vector associated with the external loads, **p**. Equation 12.1 is, of course, nothing but Newton's second law assuming linear stiffness and damping, and the method of virtual work is nothing but a method that helps set this up for a multibody system and that is especially suited for a chain system. Knowing the loads and appropriate conditions for the velocities and the deformations, Equation 12.1 can be solved for the accelerations from which the velocities and deformations can be estimated for the next time step. The number of elements in **x** is called the number of degrees of freedom (DOF) and the higher this number the more computational time is needed in each time step to solve the matrix

system. The use of modal shape functions is a tool to reduce the number of degrees of freedom and thus reduce the size of the matrices to make calculating each time step quicker. A modal shape function is a physical deflection shape, and in this method the actual deflection is found in each time step as a linear combination of a few modal shape functions. For a wind turbine such an approach is suitable to describe the deflection of the rotor blades, and the assumption is that the combination of the power spectral density of the loads and the damping of the system do not excite eigenmodes associated with higher frequencies. In the commercially available and widely used aeroelastic simulation tool, FLEX, see for example Øye (1996), only the first 3 or 4 (2 flapwise and 1 or 2 edgewise) eigenmodes are used for the blades, and results are in good agreement with measurements, indicating the validity of the assumption. First one has to decide on the degrees of freedom necessary to describe a realistic deformation of a wind turbine. For instance in FLEX4, 17–20 DOFs are used for a three-bladed wind turbine, i.e. 3–4 DOFs per blade as described above, the deformation of the shaft is described using 4 DOFs (1 for torsion, 2 hinges just before the first bearing with associated angular stiffness to describe bending and 1 for pure rotation), 1 DOF to describe the tilt stiffness of the nacelle and finally 3 DOFs for the tower (1 for torsion, 1 mode in the direction of the rotor normal and in the lateral direction).

The values in the vector, $\mathbf{x}$, describing the deformation of the construction, x_i, are denoted the general coordinates. To each generalized coordinate is associated a deflection shape, $\mathbf{u}_i$, that describes the deformation of the construction when only x_i is different from zero and typically has a unit value. The element i in the generalized force corresponding to a small displacement in DOF number i, dx_i, is calculated such that the work done by the generalized force equals the work done on the construction by the distributed external loads on the associated deflection shape

$$F_{g,i}dx_i = \int_S \mathbf{p}\cdot\mathbf{u}_i dS\,, \tag{12.2}$$

where S denotes the entire system. Please note that the generalized force can be a moment and that the displacement can be angular. All loads must be included, that is, gravity and inertial loads such as Coriolis, centrifugal and gyroscopic loads as well. The non-linear centrifugal stiffening can be modelled as equivalent loads calculated from the local centrifugal force and the actual deflection shape as shown in the previous chapter. The elements in the mass matrix, $m_{i,j}$, can be evaluated as the generalized force from the inertia loads from an unit acceleration of DOF j for a unit displacement of DOF i. The elements in the stiffness matrix, $k_{i,j}$, correspond to the generalized force from an external force field which keeps the system in equilibrium for a unit displacement in DOF j and which then is displaced x_i=1. The elements in the damping matrix can be found similarly. For a chain system the method of virtual work as described here normally gives a full mass matrix and diagonal matrices for the stiffness and damping. For one blade rigidly clamped at the root (cantilever beam) it is relatively easy to estimate the lowest eigenmodes (first flapwise $\mathbf{u}^{1f}(x)$, first edgewise $\mathbf{u}^{1e}(x)$ and second flapwise $\mathbf{u}^{2f}(x)$) for example

by using the iterative procedure from the previous chapter. The description of the principle of virtual work might seem very abstract, but will hopefully be clearer after using it on two examples: one of two discrete masses connected by springs and dampers, and another for an isolated blade, see the end of this chapter.

If the structural system comprises a system of continuous mass distributions as, for example, a system of beams, Equation 12.1 is the result from discretizing the system, since, in reality, such a system has an infinite number of DOFs. The elements in the mass, stiffness and damping matrices depend on the system and in case of a continuous system also of the discretization. If the right hand side of Equation 12.1 is 0 the system is said to perform its natural motion.

Provided that the deflections, $\mathbf{x}$, and velocities, $\dot{\mathbf{x}}$, are known, Equation 12.1 can alternatively be written as:

$$\mathbf{M}\ddot{\mathbf{x}} = \mathbf{F}_g - \mathbf{C}\dot{\mathbf{x}} - \mathbf{K}\mathbf{x} = \mathbf{f}(\dot{\mathbf{x}}, \mathbf{x}, t) \tag{12.3}$$

where the function $\mathbf{f}$ in general is non-linear. Non-linearity can, for example, come from non-linear loads $\mathbf{p}$ or from aerodynamic damping. A non-linear system can be treated as a linearized eigenvalue approach or as a full non-linear time domain approach. Only the latter method is treated in this text.

Knowing the right hand side of Equation 12.3 at time $t^n = n\Delta t$, the acceleration, $\ddot{\mathbf{x}}^n$, at time t^n is found solving the linear system of equations:

$$\ddot{\mathbf{x}}^n = \mathbf{M}^{-1}\mathbf{f}(\dot{\mathbf{x}}^n, \mathbf{x}^n, t^n) \tag{12.4}$$

Knowing the accelerations, $\ddot{\mathbf{x}}^n$, the velocities, $\dot{\mathbf{x}}^n$, and positions, $\mathbf{x}^n$, at time t^n a Runge–Kutta–Nyström scheme can be used to estimate the velocities, $\dot{\mathbf{x}}^{n+1}$, and positions, $\mathbf{x}^{n+1}$, at t^{n+1}. New loads, $\mathbf{p}^{n+1}(\dot{\mathbf{x}}^{n+1}, \mathbf{x}^{n+1}, t^{n+1})$ can be calculated using for example, an unsteady BEM method, and thus Equation 12.4 can be updated and a new time step can be performed. This can be continued until a sufficient time period has been simulated.

The Runge–Kutta–Nyström integration scheme of $\ddot{\mathbf{x}} = \mathbf{g}(t, \dot{\mathbf{x}}, \mathbf{x})$

$$\mathbf{A} = \frac{\Delta t}{2}\ddot{\mathbf{x}}^n$$

$$\mathbf{b} = \frac{\Delta t}{2}(\dot{\mathbf{x}}^n + \tfrac{1}{2}\mathbf{A})$$

$$\mathbf{B} = \frac{\Delta t}{2}\mathbf{g}(t^{n+\frac{1}{2}}, \mathbf{x}^n + \mathbf{b}, \dot{\mathbf{x}}^n + \mathbf{A})$$

$$\mathbf{C} = \frac{\Delta t}{2}\mathbf{g}(t^{n+\frac{1}{2}}, \mathbf{x}^n + \mathbf{b}, \dot{\mathbf{x}}^n + \mathbf{B})$$

$$\mathbf{d} = \Delta t(\dot{\mathbf{x}}^n + \mathbf{C})$$

$$\mathbf{D} = \frac{\Delta t}{2}\mathbf{g}(t^{n+1}, \mathbf{x}^n + \mathbf{d}, \dot{\mathbf{x}}^n + 2\mathbf{C})$$

and the final update:

$$t^{n+1} = t^n + \Delta t$$

$$\mathbf{x}^{n+1} = \mathbf{x}^n + \Delta t(\dot{\mathbf{x}}^n + \tfrac{1}{3}(\mathbf{A} + \mathbf{B} + \mathbf{C}))$$

$$\dot{\mathbf{x}}^{n+1} = \dot{\mathbf{x}}^n + \tfrac{1}{3}(\mathbf{A} + 2\mathbf{B} + 2\mathbf{C} + \mathbf{D})$$

$$\ddot{\mathbf{x}}^{n+1} = \mathbf{g}(t^{n+1}, \mathbf{x}^{n+1}, \dot{\mathbf{x}}^{n+1})$$

Single degree of freedon

The simplest dynamic system is called single degree of freedom (SDOF) and comprises only one concentrated mass. Imagine, for example, a mass which is hung on a spring as shown in Figure 12.1.

Statically the spring will be stretched until the spring force equals the weight *Mg*. The dynamic equation is:

$$M\ddot{u} + ku = 0\,, \tag{12.5}$$

where k is the spring constant and u the displacement from the equilibrium position. The well known analytical solution to this system is:

$$u = u_o \cos(\omega_N t) + \frac{\dot{u}_o}{\omega_N}\sin(\omega_N t) \tag{12.6}$$

u_o is the pertubation at t=0, $\dot{u}_o$ is the velocity at t=0 and $\omega_N = \sqrt{k/M}$ is the eigenfrequency of the system. The system performs a simple harmonic vibration and the time for one cycle is $T = 2\pi/\omega_N$. This simple SDOF system can, for example, be used to check the implementation, accuracy and stability of the Runge–Kutta–Nyström method.

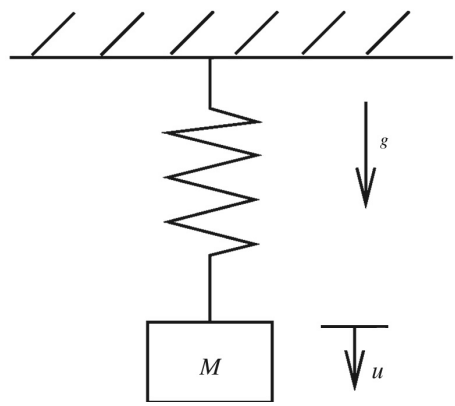

Figure 12.1 SDOF system with no damping

Aerodynamic damping

The aerodynamic forces from the flow past a structure can cause damping that may be negative and thus amplify vibrations. Below is a description of the aerodynamic damping using a simple SDOF system, but now including aerodynamic forces, as shown in Figure 12.2. The system comprises an airfoil in a wind tunnel, which is mounted with a geometrical angle of attack α_g on a spring that allows the airfoil to move up and down. Imagine now that the blade is moving downwards with a velocity $\dot{x}$. The airfoil then feels an extra velocity, equal to $\dot{x}$ but in the opposite direction, giving a component from below that, when added to the velocity in the wind tunnel V_o, gives the relative velocity, see Figure 12.2. Provided that the airfoil data, $C_l(\alpha)$, are known, the flow angle ϕ, the angle of attack and the force in the *x*-direction can be estimated as:

$$\tan\phi = \frac{\dot{x}}{V_o} \tag{12.7}$$

$$\alpha = \alpha_g + \phi \tag{12.8}$$

$$F_x = \tfrac{1}{2}\rho V_{rel}^2 A C_l(\alpha)\cos\phi \tag{12.9}$$

When the airfoil moves downwards the angle of attack increases, and when moving upwards the angle of attack is decreased according to Equations 12.7 and 12.8. This changes the lift coefficient:

$$C_l = C_{l,o} + \frac{\partial C_l}{\partial \alpha}\Delta\alpha, \tag{12.10}$$

where $C_{l,o}$ is the previous value of the lift coefficient and C_l the new lift coefficient at the higher angle of attack. If the airfoil is moving downwards and the slope $\partial C_l / \partial \alpha$ is positive, the lift coefficient and thus the aerodynamic force is increased and since this increased force is in the opposite direction as the motion, the vibration is damped. The same argument is valid when the blade

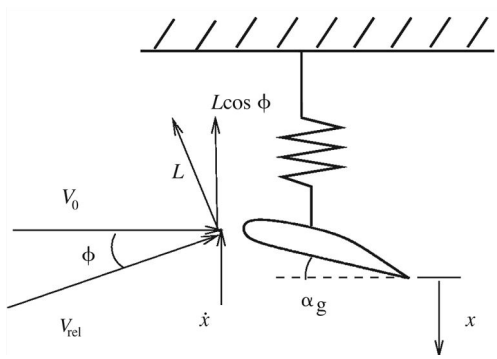

Figure 12.2 SDOF with lift

is moving upwards. If the slope, however, is negative as in stalled conditions, the aerodynamic damping is negative. More formally the work done by the aerodynamic forces on the section during one cycle can be calculated as:

$$W = -\oint \mathbf{F} \cdot \mathbf{dx} \tag{12.11}$$

F is the aerodynamic force on the airfoil and **x** the displacement. If the work is positive the section is positively damped, and if the work is negative the section is negatively damped. To have the correct slopes for the lift and drag coefficients is therefore essential for correctly predicting the stability. For these types of vibrations, dynamic-stall models as described in Chapter 9 are thus very important. In some cases the dynamic-stall model effectively increases the slope $\partial C_l / \partial \alpha$, and thus the stability. In other words, computations may over-predict the oscillations if static airfoil data are used.

Examples of using the principle of virtual work

Two examples will be shown how to use the principle of virtual work to create the mass, stiffness and damping matrices in Equation 12.1. The first example is a 2-DOF system comprising two masses connected by springs and dampers as shown in Figure 12.3. The second example is a wind turbine blade using modal shapes in order to reduce the number of DOFs.

2-DOF system

The mass and stiffness matrices together with the generalized force vector for the 2-DOF system shown in Figure 12.3 will be set up using the principle of virtual work and generalized coordinates.

The methodology is as follows: first the generalized coordinates, (x_1,x_2), are defined, for example, as the relative displacements between the two masses:

$$\begin{aligned} x_1 &= u_1 \\ x_2 &= u_2 - u_1 \end{aligned} \tag{12.12}$$

where u_1 and u_2 are the displacements of mass 1 and 2, respectively. The generalized force vector, $\mathbf{F}_g$, is found by the principle of virtual work as the work done by the external forces, F_1 and F_2, for a displacement of one of the generalized

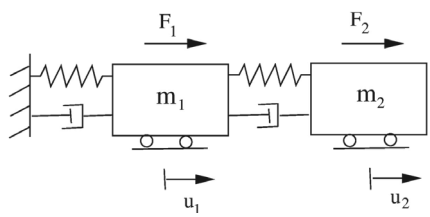

Figure 12.3 Example of a 2-DOF system

coordinates keeping the other(s) zero. The first component is found for x_1=1 and x_2=0 as $F_{g,1}$=F_1+F_2 since in this case both masses move a unit length. The second component is found putting x_1=0 and x_2=1 as $F_{g,2}$=F_2 since in this case only mass 2 moves a unit length. The mass matrix is found specifying a unit acceleration of one of the generalized coordinates keeping the other(s) zero and replacing the external forces by inertia forces, i.e. mass times acceleration. For $\ddot{x}_1$ =1 and $\ddot{x}_2$ =0 both masses 1 and 2 accelerate with a unit acceleration, i.e. the corresponding inertial forces become, F_1=m_1 and F_2=m_2, and the generalized force based on these become $F_{g,1}$=m_1+m_2 and $F_{g,2}$=m_2. This gives the first column in the mass matrix as shown below:

$$\begin{bmatrix} m_{11} & m_{12} \\ m_{21} & m_{22} \end{bmatrix} \begin{bmatrix} 1 \\ 0 \end{bmatrix} = \begin{bmatrix} m_{11} \\ m_{21} \end{bmatrix} = \begin{bmatrix} m_1 + m_2 \\ m_2 \end{bmatrix} \tag{12.13}$$

The second column is found specifying $\ddot{x}_1$ =0 and $\ddot{x}_2$ =1, i.e. only mass 2 accelerates and the inertia forces become F_1=0 and F_2= m_2. The generalized force based on these inertia forces yield $F_{g,1}$=m_2 and $F_{g,2}$=m_2 yielding:

$$\begin{bmatrix} m_{11} & m_{12} \\ m_{21} & m_{22} \end{bmatrix} \begin{bmatrix} 0 \\ 1 \end{bmatrix} = \begin{bmatrix} m_{12} \\ m_{22} \end{bmatrix} = \begin{bmatrix} m_2 \\ m_2 \end{bmatrix} \tag{12.14}$$

The mass matrix therefore becomes:

$$\mathbf{M} = \begin{bmatrix} m_1 + m_2 & m_2 \\ m_2 & m_2 \end{bmatrix} \tag{12.15}$$

The first column in the stiffness matrix can be found using the necessary generalized force to obtain a unit static displacement of the first generalized coordinate, i.e. x_1=1 and x_2=0. The necessary external forces for this unit displacement are F_1=k_1 and F_2=0, where k_1 is the spring constant for spring 1. The corresponding generalized force is $F_{g,1}$=F_1+F_2= k_1 and $F_{g,2}$=F_2=0, and the first column in the stiffness matrix becomes:

$$\begin{bmatrix} k_{11} & k_{12} \\ k_{21} & k_{22} \end{bmatrix} \begin{bmatrix} 1 \\ 0 \end{bmatrix} = \begin{bmatrix} k_{11} \\ k_{21} \end{bmatrix} = \begin{bmatrix} k_1 \\ 0 \end{bmatrix} \tag{12.16}$$

The second column is found as the necessary generalized force to obtain a unit static displacement of the second generalized coordinate, i.e. x_1=0 and x_2=1. The necessary external forces for this unit displacement are F_1=–k_2 and F_2= k_2, where k_2 is the spring constant for spring 2. The corresponding generalized force is $F_{g,1}$=F_1+F_2=0 and $F_{g,2}$=F_2= k_2 yielding:

$$\begin{bmatrix} k_{11} & k_{12} \\ k_{21} & k_{22} \end{bmatrix} \begin{bmatrix} 0 \\ 1 \end{bmatrix} = \begin{bmatrix} k_{12} \\ k_{22} \end{bmatrix} = \begin{bmatrix} 0 \\ k_2 \end{bmatrix} \tag{12.17}$$

The stiffness matrix therefore becomes:

$$\mathbf{K} = \begin{bmatrix} k_1 & 0 \\ 0 & k_2 \end{bmatrix} \tag{12.18}$$

The damping matrix can be found similarly. The first column is the necessary generalized force to obtain a unit velocity of the first generalized coordinate, i.e. $\dot{x}_1 = 1$ and $\dot{x}_2 = 0$. The result is similar to the stiffness matrix and the damping matrix becomes:

$$\mathbf{C} = \begin{bmatrix} d_1 & 0 \\ 0 & d_2 \end{bmatrix} \tag{12.19}$$

where d_1 and d_2 are the coefficients of viscous damping for the two dampers. In a chain formulation as the above example, the stiffness and damping matrices become diagonal matrices, whereas the mass matrix becomes full.

The full system is thus determined as:

$$\begin{bmatrix} m_1 + m_2 & m_2 \\ m_2 & m_2 \end{bmatrix} \begin{bmatrix} \ddot{x}_1 \\ \ddot{x}_2 \end{bmatrix} + \begin{bmatrix} d_1 & 0 \\ 0 & d_2 \end{bmatrix} \begin{bmatrix} \dot{x}_1 \\ \dot{x}_2 \end{bmatrix} + \begin{bmatrix} k_1 & 0 \\ 0 & k_2 \end{bmatrix} \begin{bmatrix} x_1 \\ x_2 \end{bmatrix} = \begin{bmatrix} F_1 + F_2 \\ F_2 \end{bmatrix} \tag{12.20}$$

To verify the described method, Newton's second law is applied on each mass:

$$m_1 \ddot{u}_1 = -k_1 u_1 - d_1 \dot{u}_1 + k_2 (u_2 - u_1) + d_2 (\dot{u}_2 - \dot{u}_1) + F_1 \tag{12.21}$$

$$m_2 \ddot{u}_2 = -k_2 (u_2 - u_1) - d_2 (\dot{u}_2 - \dot{u}_1) + F_2 \tag{12.22}$$

Replacing u_1 by x_1 and u_2 by $x_1 + x_2$ and replacing Equation 12.21 with Equation 12.21 plus Equation 12.22, make Equations 12.21 and 12.22 identical to Equation system 12.20. It is straightforward to add more masses.

Dynamic system for blade

The methodology of generalized coordinates is now applied on a wind turbine blade as shown in Figure 11.5. Assume that we know the normalized eigenmodes, i.e. with a maximum tip deflection of 1 m. The first eigenmodes can be calculated as for example shown in the previous chapter and are shown in Figures 11.10 to 11.12.

It is assumed that a deformation of a blade can be described as a linear combination of these three modes as:

$$u_z(x) = x_1 \cdot u_z^{1f}(x) + x_2 \cdot u_z^{1e}(x) + x_3 \cdot u_z^{2f}(x) \tag{12.23}$$

and

$$u_y(x) = x_1 \cdot u_y^{1f}(x) + x_2 \cdot u_y^{1e}(x) + x_3 \cdot u_y^{2f}(x) \tag{12.24}$$

The deflection shape can thus be described by three parameters only, which are denoted by the generalized coordinates, x_1, x_2 and x_3. Since the modes are constant the velocities and accelerations along the blade are:

$$\dot{u}_z(x) = \dot{x}_1 \cdot u_z^{1f}(x) + \dot{x}_2 \cdot u_z^{1e}(x) + \dot{x}_3 \cdot u_z^{2f}(x) \tag{12.25}$$

$$\dot{u}_y(x) = \dot{x}_1 \cdot u_y^{1f}(x) + \dot{x}_2 \cdot u_y^{1e}(x) + \dot{x}_3 \cdot u_y^{2f}(x) \tag{12.26}$$

and

$$\ddot{u}_z(x) = \ddot{x}_1 \cdot u_z^{1f}(x) + \ddot{x}_2 \cdot u_z^{1e}(x) + \ddot{x}_3 \cdot u_z^{2f}(x) \tag{12.27}$$

$$\ddot{u}_y(x) = \ddot{x}_1 \cdot u_y^{1f}(x) + \ddot{x}_2 \cdot u_y^{1e}(x) + \ddot{x}_3 \cdot u_y^{2f}(x) \tag{12.28}$$

As indicated by Equation 12.2, the generalized force for each mode is the work done on this mode by the external loads, $p_z(x)$ and $p_y(x)$, without the contribution from the other modes, that is:

$$F_{g,1} = \int p_z(x) u_z^{1f}(x) dx + \int p_y(x) u_y^{1f}(x) dx \tag{12.29}$$

$$F_{g,2} = \int p_z(x) u_z^{1e}(x) dx + \int p_y(x) u_y^{1e}(x) dx \tag{12.30}$$

and

$$F_{g,3} = \int p_z(x) u_z^{2f}(x) dx + \int p_y(x) u_y^{2f}(x) dx \tag{12.31}$$

The first column of the mass matrix is found by evaluating the generalized force from external forces that correspond to the inertia forces for a unit acceleration of the first degree of freedom and the others are set to 0, that is $(\ddot{x}_1, \ddot{x}_2, \ddot{x}_3) = (1,0,0)$. Using Equations 12.27 and 12.28, the inertia loads become $(p_y, p_z) = (m\ddot{u}_y, m\ddot{u}_z) = (mu_y^{1f}, mu_z^{1f})$ and thus

$$\begin{bmatrix} m_{11} \\ m_{21} \\ m_{31} \end{bmatrix} = \begin{bmatrix} \int u_z^{1f}(x) m(x) u_z^{1f}(x) dx + \int u_y^{1f}(x) m(x) u_y^{1f}(x) dx \\ \int u_z^{1f}(x) m(x) u_z^{1e}(x) dx + \int u_y^{1f}(x) m(x) u_y^{1e}(x) dx \\ \int u_z^{1f}(x) m(x) u_z^{2f}(x) dx + \int u_y^{1f}(x) m(x) u_y^{2f}(x) dx \end{bmatrix} = \begin{bmatrix} \mathrm{GM}_1 \\ 0 \\ 0 \end{bmatrix} \tag{12.32}$$

The first element is sometimes termed the first generalized mass (GM_1), and the two other integrals are 0 due to the orthogonality constraints between eigenmodes.

The second column of the mass matrix is found by evaluating the generalized force from external forces corresponding to the inertia forces for a unit acceleration of the second degree of freedom and the others 0, that is $(\ddot{x}_1, \ddot{x}_2, \ddot{x}_3) = (0,1,0)$. Using Equations 12.27 and 12.28, the inertia loads become $(p_y, p_z) = (m\ddot{u}_y, m\ddot{u}_z) = (mu_y^{1e}, mu_z^{1e})$ and thus

$$\begin{bmatrix} m_{12} \\ m_{22} \\ m_{32} \end{bmatrix} = \begin{bmatrix} \int u_z^{1e}(x)m(x)u_z^{1f}(x)dx + \int u_y^{1e}(x)m(x)u_y^{1f}(x)dx \\ \int u_z^{1e}(x)m(x)u_z^{1e}(x)dx + \int u_y^{1e}(x)m(x)u_y^{1e}(x)dx \\ \int u_z^{1e}(x)m(x)u_z^{2f}(x)dx + \int u_y^{1e}(x)m(x)u_y^{2f}(x)dx \end{bmatrix} = \begin{bmatrix} 0 \\ GM_2 \\ 0 \end{bmatrix} \tag{12.33}$$

The second element is sometimes termed the second generalized mass, and the two other integrals are 0 due to the orthogonality constraints between eigenmodes.

The third column of the mass matrix is found by evaluating the generalized force from external forces corresponding to the inertia forces for a unit acceleration of the third degree of freedom and the others 0, that is $(\ddot{x}_1, \ddot{x}_2, \ddot{x}_3) = (0,0,1)$. Using Equations 12.27 and 12.28, the inertia loads become $(p_y, p_z) = (m\ddot{u}_y, m\ddot{u}_z) = (mu_y^{2f}, mu_z^{2f})$ and thus:

$$\begin{bmatrix} m_{13} \\ m_{23} \\ m_{33} \end{bmatrix} = \begin{bmatrix} \int u_z^{2f}(x)m(x)u_z^{1f}(x)dx + \int u_y^{2f}(x)m(x)u_y^{1f}(x)dx \\ \int u_z^{2f}(x)m(x)u_z^{1e}(x)dx + \int u_y^{2f}(x)m(x)u_y^{1e}(x)dx \\ \int u_z^{2f}(x)m(x)u_z^{2f}(x)dx + \int u_y^{2f}(x)m(x)u_y^{2f}(x)dx \end{bmatrix} = \begin{bmatrix} 0 \\ 0 \\ GM_3 \end{bmatrix} \tag{12.34}$$

The third element is sometimes termed the third generalized mass, and the two other integrals are 0 due to the orthogonality constraints between eigenmodes.

The first column in the stiffness matrix can be found using the necessary generalized force to obtain a unit static displacement of the first generalized coordinate, i.e. $(x_1, x_2, x_3) = (1,0,0)$. In this case the deflection is according to Equations 12.23 and 12.24 identical to u_y^{1f}, u_z^{1f}. The loads yielding this deflection is according to Equations 11.38 and 11.39 $(p_y, p_z) = (m\omega_1^2 u_y^{1f}, m\omega_1^2 u_z^{1f})$ where ω_1 is the eigenfrequency associated with the first flapwise eigenmode, and applying this in the equations for the generalized force (12.29–12.31) yields:

$$\begin{bmatrix} k_{11} \\ k_{21} \\ k_{31} \end{bmatrix} = \begin{bmatrix} \int \omega_1^2 u_z^{1f} m u_z^{1f} dx + \int \omega_1^2 u_y^{1f} m u_y^{1f} dx \\ \int \omega_1^2 u_z^{1f} m u_z^{1e} dx + \int \omega_1^2 u_y^{1f} m u_y^{1e} dx \\ \int \omega_1^2 u_z^{1f} m u_z^{2f} dx + \int \omega_1^2 u_y^{1f} m u_y^{2f} dx \end{bmatrix} = \begin{bmatrix} \omega_1^2 GM_1 \\ 0 \\ 0 \end{bmatrix} \tag{12.35}$$

The two last integrals are 0 due to the orthogonality constraint of the eigenmodes. Similarly it can be shown:

$$\begin{bmatrix} k_{12} \\ k_{22} \\ k_{32} \end{bmatrix} = \begin{bmatrix} 0 \\ \omega_2^2 GM_2 \\ 0 \end{bmatrix} \tag{12.36}$$

and

$$\begin{bmatrix} k_{13} \\ k_{23} \\ k_{33} \end{bmatrix} = \begin{bmatrix} 0 \\ 0 \\ \omega_3^2 GM_3 \end{bmatrix} \tag{12.37}$$

ω_2 and ω_3 are the eigenfrequencies associated with the first edgewise and second flapwise eigenmode, respectively. The generalized masses GM_1, GM_2 and GM_3 are defined in Equations 12.32–12.34.

Ignoring the structural damping, the equation for one blade becomes:

$$\begin{bmatrix} GM_1 & 0 & 0 \\ 0 & GM_2 & 0 \\ 0 & 0 & GM_3 \end{bmatrix} \begin{bmatrix} \ddot{x}_1 \\ \ddot{x}_2 \\ \ddot{x}_3 \end{bmatrix} + \begin{bmatrix} \omega_1^2 GM_1 & 0 & 0 \\ 0 & \omega_2^2 GM_2 & 0 \\ 0 & 0 & \omega_3^2 GM_3 \end{bmatrix} \begin{bmatrix} x_1 \\ x_2 \\ x_3 \end{bmatrix} = \begin{bmatrix} F_{g,1} \\ F_{g,2} \\ F_{g,3} \end{bmatrix} \tag{12.38}$$

Structural damping terms can be modelled as:

$$\mathbf{C} = \begin{bmatrix} \omega_1 GM_1 \frac{\delta_1}{\pi} & 0 & 0 \\ 0 & \omega_2 GM_2 \frac{\delta_2}{\pi} & 0 \\ 0 & 0 & \omega_2 GM_2 \frac{\delta_3}{\pi} \end{bmatrix} \tag{12.39}$$

where δ_i is logarithmic decrement associated with mode *i*. The system for the beam in Equation 12.38 comprises three uncoupled differential equations. This is a result of the orthogonality constraints on the used eigenmodes, and is not a general result of the principle of virtual work. For instance when the method is used on a whole wind turbine construction the equation of motion becomes coupled.

Finite element method models

Alternatively a more formal finite element method (FEM) can be used to set up the dynamic structural model in the form of Equation 12.1. In Ahlström (2005) and Schepers (2002) can be found a long list of various aeroelastic codes, and many of the recently developed codes has used the FEM approach. However, the number of DOFs will in a FEM discretization be considerably larger than when combining the principle of virtual work with mode shapes as shown, for example, in the section above dealing with a single blade. Therefore the computational time to calculate a time history of a certain length is much larger when a FEM approach is taken. In this book there will be no attempt to use the FEM approach for modelling a wind turbine, but more details and further reference can be found in Hansen et al. (2006).

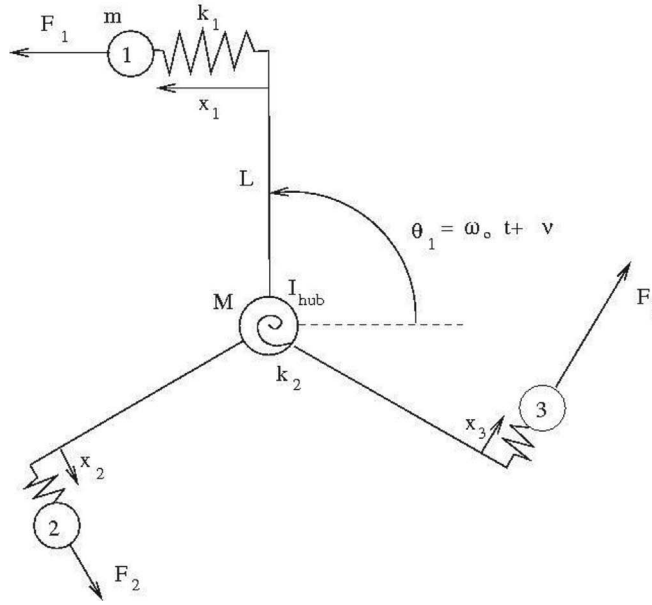

Figure 12.4 Simple 4 DOF mechanical system

A simplified structural rotor model

Some issues related to the choice of eigenfrequencies on a wind turbine blade will be illuminated by the simplified mechanical 4-DOF system shown in Figure 12.4. First, the system will be exposed to a periodic forced excitation and, second, the free vibrations are treated.

Forced excitation of simplified structural wind turbine model

The system comprises three rotating rods attached to a common hub, that has an inertia moment, I_{hub}. On the end of each rod of length, L, is attached a mass, m, a linear spring, k_1 and a damper. The mass, spring and damper on the rods are modelling the edgewise vibrations of a wind turbine blade and the ratio between the spring constant and the mass is set to satisfy, $\omega_{edge} = \sqrt{k_1 / m}$, where ω_{edge} is the edgewise eigenfrequency of the blade. The total moment inertia about the hub is $I_{tot}=I_{hub}+3mL^2$. The blades are fixed to a shaft, which is flexible in torsion, and which in the opposite end of the blades is rotated with a constant angular velocity ω_o, so that the azimuthal position of blade number one is $\theta_1= \omega_o t+\upsilon$, where υ is the torsional deformation of the shaft. The azimuthal positions of blades number 2 and 3 are $\theta_2= \theta_1+2\pi/3$ and $\theta_3= \theta_1+4\pi/3$, respectively. The shaft torsion is modelled as a stiff shaft on which is mounted a torsional spring on which the blades are mounted. The spring constant for the torsional spring is, k_2 and the ratio between the total inertia moment and

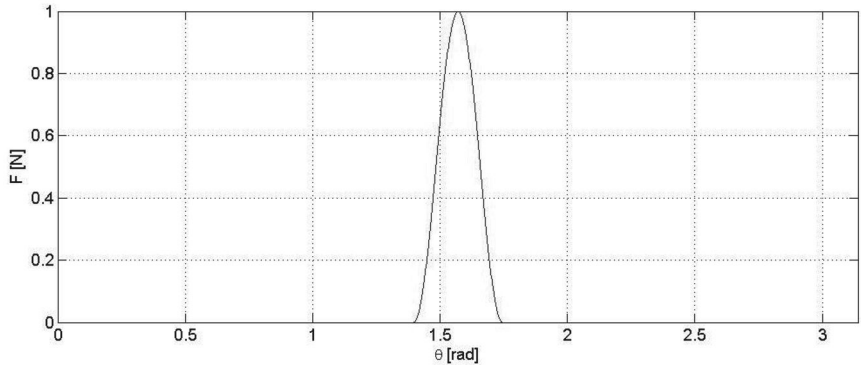

Figure 12.5 The shape of the force for p_o=1, b=18 and θ_o=π/2

the torsional spring constant is set to model the torsional eigenfrequency of a wind turbine shaft as $\omega_s = \sqrt{k_2 / I_{tot}}$. The degrees of freedom of the mechanical system are the three displacements of the masses relative to the rods, x_1, x_2 and x_3 and the torsional displacement of the shaft, v. The external loads are three forces acting on the masses, F_1, F_2 and F_3 and an external moment acting on the shaft, M. M is set to 0 N/m and the external force field is fixed in space at an azimuthal position of θ_o, and the strength is determined by following equation where, θ, is the azimuthal position in space.

$$F = \begin{cases} \frac{1}{2} p_o (1 + \cos(b \cdot (\theta - \theta_o))) & \text{for } \left|\frac{b}{\pi}(\theta - \theta_o)\right| \le 1 \\ 0 & \text{for } \left|\frac{b}{\pi}(\theta - \theta_o)\right| > 1 \end{cases} \tag{12.40}$$

Figure 12.5 shows a plot of the force, F, as function of the azimuthal position in space for p_o=1, b=18 and θ_o=π/2. The azimuthal positions where the force is non zero is for θ between $\theta_o \pm \pi/b$, i.e. $\theta_o \pm 10$ degrees for b=18.

Every time a rod passes the azimuthal position of the force, the attached mass is exposed to this field for a short time and a vibration is excited. The angular velocity of a wind turbine rotor, ω_o, is often denoted as 1P (one per revolution). The shape of the external force field simulates the impulsive load experienced by a wind turbine blade as it passes the tower once per revolution, or repeatedly sweeps through an area of the rotor plane with a high or low wind speed due to atmospheric turbulence. The temporal duration of these high or low wind speed areas from atmospheric turbulence is often higher than the rotational time of the rotor, T=2π/ω_o (depending on the length scale of the turbulent eddy and the wind speed), so that a blade passes such an area during several revolutions.

Figures 12.6 and 12.7 show the time history of the force experienced by one blade rotating with constant angular velocity (that is a stiff shaft) and its corresponding Fourier transform, respectively. It is seen in Figure 12.7 that the repeating impulse-like force as described by Equation 12.40 shown in Figure 12.6

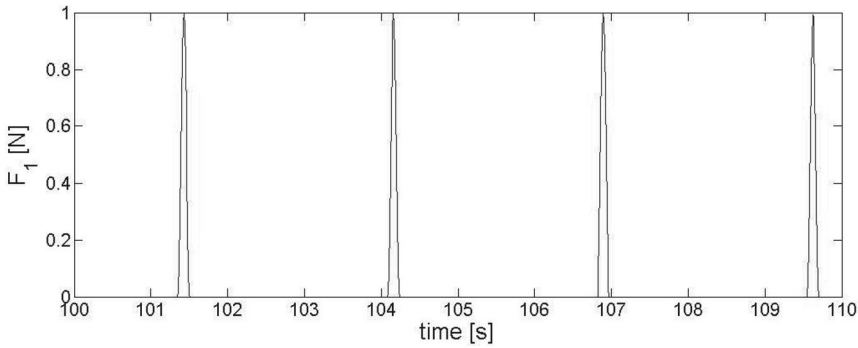

Figure 12.6 Time series of the force experienced by one rod ω_o=2.3 rad/s, p_o=1 and b=18.

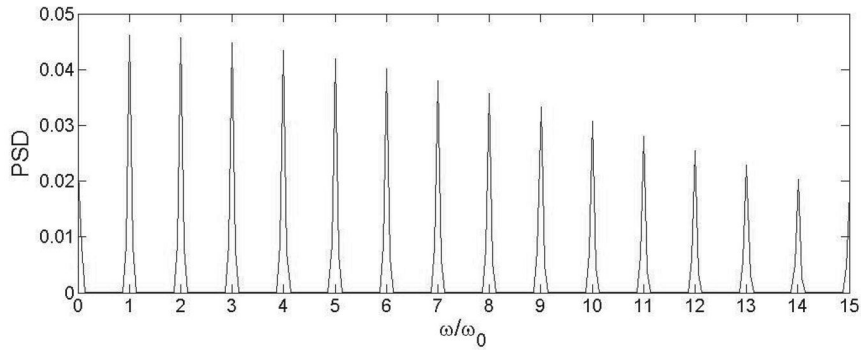

Figure 12.7 The Fourier transform of the time signal of the force experienced by one rod shown in Figure 12.6

is composed by a series of sinusoidal signals with discrete frequencies, $n\cdot\ \omega_{0;}$ n=1,2,3,….

The response of mass number one will be a periodic motion that can be decomposed as a Fourier series as

$$x_1 = \sum_{n=1}^{\infty} a_n \sin(n\omega_o t) + b_n \cos(n\omega_o t) \tag{12.41}$$

If the time series for the motion of mass one is differentiated twice with respect to time it can be seen that the acceleration and thus the inertia force also has the form of Equation 12.41. As can be seen from Figure 12.8 the contribution to the torque at the shaft from rod number one is for a torsional stiff shaft

$$M_1(t) = -mL\ddot{x}_1 + L\cdot F_1(t) \tag{12.42}$$

It should be mentioned that, in the more general case also including shaft deformation, the acceleration of the mass becomes $a = \ddot{x}_1 + L\ddot{v}$, The torque from rod number 2 will have the same time series, but delayed in time T/3 and

the time series of the torque from rod number three will also be the same but delayed $2T/3$. The time series for the total torque at the shaft from the three rods will thus have the form

$$\begin{aligned}
M_{shaft} &= M_1 + M_2 + M_3 \\
&= \sum_{n=1}^{\infty} c_n \sin(n\omega_o t) + d_n \cos(n\omega_o t) \\
&+ \sum_{n=1}^{\infty} c_n \sin(n\omega_o (t - \tfrac{T}{3})) + d_n \cos(n\omega_o (t - \tfrac{T}{3})) \\
&+ \sum_{n=1}^{\infty} c_n \sin(n\omega_o (t - \tfrac{2T}{3})) + d_n \cos(n\omega_o (t - \tfrac{2T}{3})) \\
&= \sum_{n=1}^{\infty} c_n \sin(n\omega_o t) + d_n \cos(n\omega_o t) \\
&+ \sum_{n=1}^{\infty} c_n \sin(n\omega_o t - \tfrac{n2\pi}{3}) + d_n \cos(n\omega_o t - \tfrac{n2\pi}{3}) \\
&+ \sum_{n=1}^{\infty} c_n \sin(n\omega_o t - \tfrac{n4\pi}{3}) + d_n \cos(n\omega_o t - \tfrac{n4\pi}{3})
\end{aligned} \tag{12.43}$$

From Equation 12.43 it can be seen that the combined rods only give a non-zero shaft torque for n=3, 6, 9, … since for all other values the sin and cos terms are phase-shifted 120 degrees. That means that the motion of the shaft will be very low for n=1, 2, 4, 5, 7, 8,… and that the three rods are decoupled and cannot feel each other's vibrations and that it would be as if each rod is rigidly clamped at one end and that the mass, spring and damper will be a classical 1-DOF mechanical system excited at resonance if $\omega_{edge} = \sqrt{k_1 / m}$ equals $n \cdot \omega_o$ for n=1, 2, 4, 5, 7, 8, … For n=3, 6, 9, … the torque at the shaft will be nonzero and torsional vibrations will be excited and absorb energy from the oscillation of the masses at the end of rods decreasing their amplitude.

The dynamics of the 4-DOF mechanical system in Figure 12.4 is governed by

$$\mathbf{M}\ddot{\mathbf{x}} + \mathbf{K}\mathbf{x} + \mathbf{C}\dot{\mathbf{x}} = \mathbf{F} \tag{12.44}$$

where

$$\mathbf{M} = \begin{bmatrix} m & 0 & 0 & mL \\ 0 & m & 0 & mL \\ 0 & 0 & m & mL \\ mL & mL & mL & I_{tot} \end{bmatrix}, \quad \mathbf{K} = \begin{bmatrix} k_1 & 0 & 0 & 0 \\ 0 & k_1 & 0 & 0 \\ 0 & 0 & k_1 & 0 \\ 0 & 0 & 0 & k_2 \end{bmatrix}$$

$$\mathbf{C} = \begin{bmatrix} c_1 & 0 & 0 & 0 \\ 0 & c_1 & 0 & 0 \\ 0 & 0 & c_1 & 0 \\ 0 & 0 & 0 & c_2 \end{bmatrix}, \quad \mathbf{F} = \begin{bmatrix} F_1 \\ F_2 \\ F_3 \\ (F_1 + F_2 + F_3)L + M \end{bmatrix}, \quad \mathbf{x} = \begin{bmatrix} x_1 \\ x_2 \\ x_3 \\ \upsilon \end{bmatrix}$$

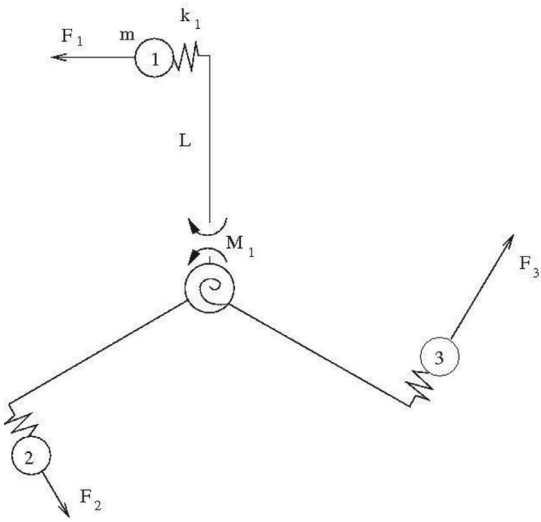

Figure 12.8 The forces acting on rod number one

and the system can be solved numerically using, for example a fourth-order Runge–Kutta–Nyström integration scheme for a force field as described above. By keeping the angular velocity of the rotating rods, ω_o, constant and by varying the edgewise frequency, ω_{edge}, one can for each ratio ω_{edge}/ω_o estimate the dynamic amplification as the ratio between the amplitude of the edgewise vibration, x_1, divided by the steady deflection, $x_s=p_o/k_1$ corresponding to a steady force $F=p_o$ in Equation 12.40. The result is plotted in Figure 12.9 for ω_o =2.3rad/s, ω_s =5.7rad/s=2.48P, L=30m, m=1kg, $k_1=m\omega^2_{edge}$, $k_2=I_{tot}\omega^2_s$, $I_{hub}=0.2I_{rotor}=0.2(3mL^2)$, δ_1=1% and δ_2=10% similar to the Tjaereborg wind turbine. The high damping of the shaft is not due to structural damping, but simulates the damping from a generator. That an asynchronous generator has an effective damping proportional to the generator slip is shown in Øye (1989). In the simulations shown in Figure 12.9 the damping c_1 and c_2 are modelled as $c_1=m\omega_{edge}\,\delta_1/\pi$ and $c_2=I_{tot}\omega_s\,\delta_2/\pi$, respectively.

From the arguments above and the numerical result in Figure 12.9 it is evident that one should aim at an edgewise blade frequency around $3\omega_o$, $6\omega_o$ or $9\omega_o$ when minimizing the effect from an impulsive blade loading at 1P from, for example, tower passage or atmospheric turbulence.

Free vibrations of the simplified structural wind turbine model

The eigenfrequencies and the corresponding eigenvectors for the free vibrations of the 4-DOF system can be solved analytically as a formal eigenvalue problem by setting $\ddot{\mathbf{x}}_{ev}=-\omega^2\mathbf{x}_{ev}$, $\mathbf{F}=0$ and assuming zero damping in Equation 12.41 yielding

$$\mathbf{M}\cdot\mathbf{x}_{ev}=\lambda\mathbf{K}\cdot\mathbf{x}_{ev}, \text{ where } \lambda=1/\omega^2 \tag{12.45}$$

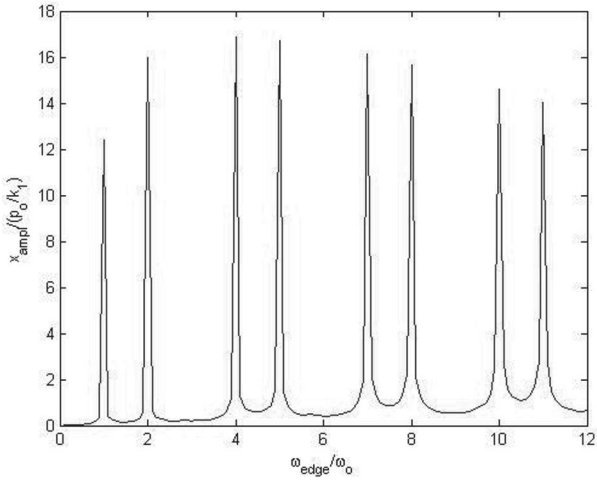

Figure 12.9 Computed dynamic amplification for the mechanical system shown in Figure 12.4 for varying ratios ω_{edge}/ω_o

The result is two symmetric and two asymmetric solutions (see Figure 12.10) where the spring, rod and masses have been replaced by a beam with distributed mass to look more like a wind turbine rotor.

In mode A all masses are in phase with the torsional spring and each other. In mode B, with a higher eigenfrequency, all masses are in phase but out of phase

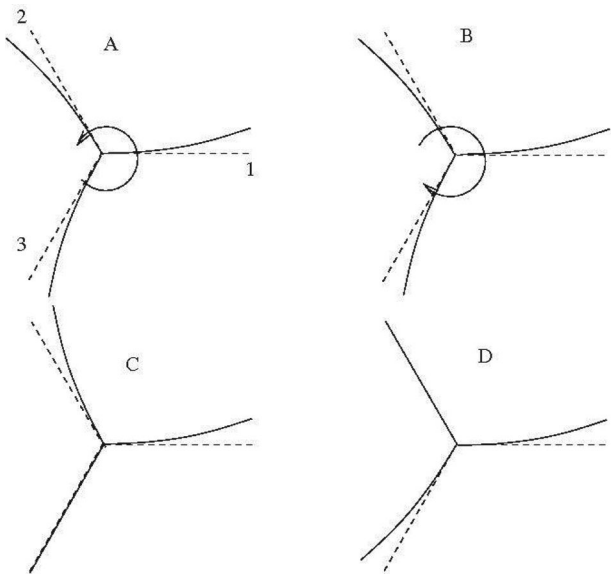

Figure 12.10 A schematic drawing of the four modes computed by solving the eigenvalue problem

with the torsional spring. The two asymmetric modes, C and D, have the same eigenfrequency and are characterized by the torsional degree of freedom being zero at all times, i.e. no shaft torsional deformation. Since mode C and D have the same frequency a new valid mode can be made as a linear combination of the two modes.

The formal solution to the eigenvalue problem is

Mode A

$$\mathbf{x}_{ev} = \begin{bmatrix} -mL \\ \dfrac{I_{tot}k_1 + mk_2 + (12L^2k_1k_2m^2 + I_{tot}^2k_1^2 - 2I_{tot}k_1k_2m + k_2^2m^2)^{0.5}}{-2k_2} + m \\ -mL \\ \dfrac{I_{tot}k_1 + mk_2 + (12L^2k_1k_2m^2 + I_{tot}^2k_1^2 - 2I_{tot}k_1k_2\mathbf{m} + k_2^2m^2)^{0.5}}{-2k_2} + m \\ -mL \\ \dfrac{I_{tot}k_1 + mk_2 + (12L^2k_1k_2m^2 + I_{tot}^2k_1^2 - 2I_{tot}\mathbf{k}_1k_2m + k_2^2m^2)^{0.5}}{-2k_2} + m \\ 1 \end{bmatrix}$$

$$\omega^2 = \frac{2k_1k_2}{I_{tot}k_1 + mk_2 + (12L^2k_1k_2m^2 + I_{tot}^2k_1^2 - 2I_{tot}k_1k_2m + k_2^2m^2)^{0.5}} \tag{12.46}$$

Mode B

$$\mathbf{x}_{ev} = \begin{bmatrix} -mL \\ \dfrac{I_{tot}k_1 + mk_2 - (12L^2k_1k_2m^2 + I_{tot}^2k_1^2 - 2I_{tot}k_1k_2m + k_2^2m^2)^{0.5}}{-2k_2} + m \\ -mL \\ \dfrac{I_{tot}k_1 + mk_2 - (12L^2k_1k_2m^2 + I_{tot}^2k_1^2 - 2I_{tot}k_1k_2\mathbf{m} + k_2^2m^2)^{0.5}}{-2k_2} + m \\ -mL \\ \dfrac{I_{tot}k_1 + mk_2 - (12L^2k_1k_2m^2 + I_{tot}^2k_1^2 - 2I_{tot}\mathbf{k}_1k_2m + k_2^2m^2)^{0.5}}{-2k_2} + m \\ 1 \end{bmatrix}$$

$$\omega^2 = \frac{2k_1k_2}{I_{tot}k_1 + mk_2 - (12L^2k_1k_2m^2 + I_{tot}^2k_1^2 - 2I_{tot}k_1k_2m + k_2^2m^2)^{0.5}}$$

Mode C

$$\mathbf{x}_{ev} = \begin{bmatrix} 1 \\ -1 \\ 0 \\ 0 \end{bmatrix}, \quad \omega^2 = \frac{k_1}{m}$$

Mode D

$$\mathbf{x}_{ev} = \begin{bmatrix} -1 \\ 0 \\ 1 \\ 0 \end{bmatrix}, \quad \omega^2 = \frac{k_1}{m}$$

Since modes C and D have the same eigenfrequency, any linear combination of the two will also be a valid solution to the eigenvalue problem. Also the linear combination can include a phase angle between the two modes. A special case is when the phase angle is 60 degrees plus or minus, where the solution for the vibrations becomes for a unit amplitude

$$\begin{aligned} x_1 &= \cos(\omega t) - \cos(\omega t \pm \pi / 3) \\ x_2 &= -\cos(\omega t) \\ x_3 &= \cos(\omega t \pm \pi / 3) \\ x_4 &= 0 \end{aligned} \tag{12.47}$$

ω is the eigenfrequency of modes C and D, which for a wind turbine blade will be the edgewise eigenfrequency of rigidly clamped blade. This gives three periodic solutions for x_1, x_2 and x_3, respectively, with the same amplitude but shifted 120 degrees. If the phase angle is $\pi/3$ then the motion is called forward whirl and if the phase angle is $-\pi/3$ it is called backward whirl as will be explained below. Since the acceleration of the shaft is zero the shear force between the rods (blades) and the shaft can be found as (see Figure 12.11)

$$\mathbf{T}_i = m\ddot{\mathbf{x}}_i \quad \text{where } i \text{ indicates the blade number} \tag{12.48}$$

The three shear forces can be added as vectors in the coordinate system attached to blade number 1 as shown in Figure 12.11

$$\begin{aligned} T_x &= T_2 \cos 30^o - T_3 \cos 30^o = m(\ddot{x}_2 - \ddot{x}_3)\cos 30^o \\ T_y &= -T_1 + T_2 \cos 60^o + T_3 \cos 60^o = m(-\ddot{x}_1 + \ddot{x}_2 \cos 60^o + \ddot{x}_3 \cos 60^o) \end{aligned} \tag{12.49}$$

Combining Equations 12.47 and 12.49 it is observed that the size of the total shear force seen by the shaft, $T = \sqrt{T_x^2 + T_y^2}$, is constant. For the case of a phase angle of $\pi/3$ in Equation 12.47 the shear force seen by the rotating shaft is rotating in the positive direction with an angular velocity equal to the edgewise eigenfrequency and is thus denoted forward whirl. Seen from the rotating shaft, blade number 1 will have its maximum deflection first, then blade number 2, and finally blade 3. If the phase angle in Equation 12.47 is $-\pi/3$, the size of the shear force will be the same, but now it rotates in the negative direction, that is opposite to the rotation of the rotor with an angular velocity of the edgewise eigenfrequency. For the backward whirl mode seen from the rotating shaft, blade number 3 will have

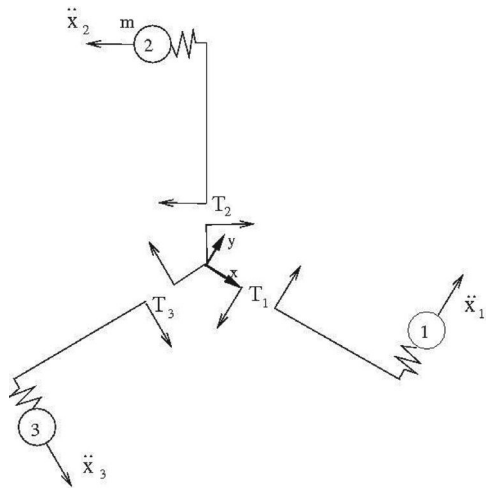

Figure 12.11 Shear force at the root of the blades from pure inertia loads and zero acceleration of shaft

its maximum deflection first, then blade number 2, and finally blade 1. Seen from a non-rotating coordinate system on, for example, the nacelle of a wind turbine, a forward whirl mode is experienced as a constant force acting on the shaft at the rotor position and rotating with an angular velocity of $\omega+\omega_o$, where ω_o is the angular velocity of the rotor (1P) and ω the edgewise eigenfrequency of the blades. A backward whirl will be experienced in the non-rotating system as a constant force acting on the shaft at the rotor position and rotating with an angular velocity of $\omega-\omega_o$. Such a force is felt just as a rotating imbalance acting at the centre of the rotor and can induce vibrations on the nacelle and tower if one of the two modes (forward or backward whirl) is excited. The whirl modes are primarily caused by edgewise vibrations, but also non-symmetric flapwise vibrations of the blades may induce rotating moments at the shaft. An analysis of the whirling modes including a Coleman transformation can be found in Hansen (2003).

References

Ahlström, A, (2005) *Aeroelastic Simulation Of Wind Turbine Dynamics*, doctoral thesis, Kungliga Tekniska Högskolan, Sweden.

Hansen, M.H. (2003) 'Improved modal dynamics of wind turbines to avoid stall-induced vibrations', *Wind Energy*, 6: 179–195.

Hansen, M.O.L., Sørensen, J.N., Voutsinas, S., Sørensen, N. and Madsen, H.A. (2006) 'State of the art in wind turbine aerodynamics and aeroelasticity', *Progress in Aerospace Sciences*, 42(4): 285–330.

Øye, S. (1989) *Transmissionsrespons for vindmølle med asynkrongenerator* AFM notat VK-162, Department of Fluid Mechanics, Technical University of Denmark (DTU) (in Danish).

Schepers, J.G. (2002) *Verification of European wind turbine design codes, VEWTDC; final report*, Technical report ECN-C-01-055. Internal ECN report.

13 Sources for loads on a wind turbine

The three most important sources for the loading of a wind turbine are

- gravitational loading
- inertial loading
- aerodynamic loading.

Gravitational loading

The earth's gravitational field causes a sinusoidal gravitational loading on each blade as indicated in Figure 13.1.

When the blade is in position 1 (downrotating), the blade root at the trailing edge side is exposed to tensile stress and the leading edge side of the blade root is exposed to compressive stress. In position 2 (uprotating), the trailing edge side of the blade root is exposed to compressive stress and the leading edge side of the blade root is exposed to tensile stress. Thus gravity is responsible for a sinusoidal loading of the blades with a frequency corresponding to the rotation of the rotor 1P. This loading is easily recognized in Figure 10.2 in the time series of the edgewise bending moment. Note that a wind turbine is designed to operate for 20 years, i.e. a machine operating at 25RPM will be exposed to $20 \times 365 \times 24 \times 60 \times 25 = 2.6 \times 10^8$ stress cycles from gravity. Since a wind turbine blade might weigh some tons and be more than 30m long, the stresses from the gravity loading are very important in the fatigue analysis.

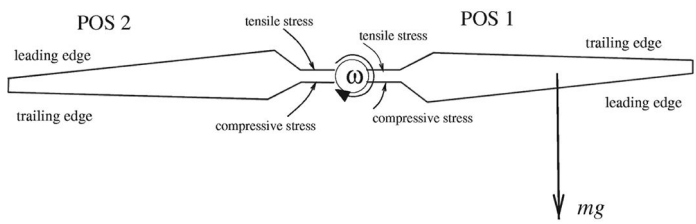

Figure 13.1 The loading caused by the earth's gravitational field

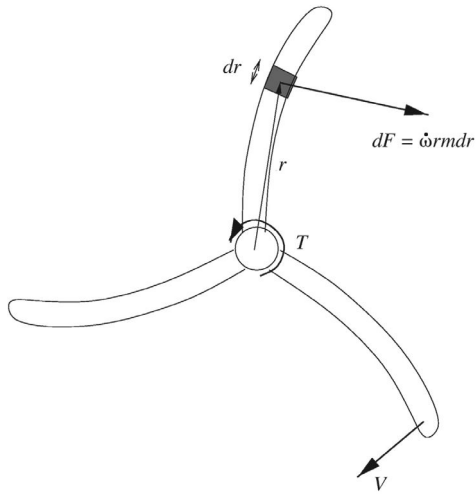

Figure 13.2 Loading caused by braking the rotor

Inertial loading

Inertial loading occurs, for example, when the turbine is accelerated or decelerated. An example is the braking of the rotor, where a breaking torque T is applied at the rotor shaft. A small section of the blade will be exposed to a force dF in the direction of the rotation as indicated in Figure 13.2.

The size of dF is found from:

$$dF = \dot{\omega} r m dr \tag{13.1}$$

where m is the mass per length of the blade, r is the radius from the rotational axis to the section, dr the size of the small section and $\dot{\omega} = d\omega / dt$ can be found from:

$$I\frac{d\omega}{dt} = T \tag{13.2}$$

where I is the moment of inertia of the rotor. The terms $m\ddot{u}$ in Equations 11.11 and 11.12 are also inertia loads stemming from local accelerations. Another inertial loading stems from the centrifugal force on the blades. In order to reduce the flapwise bending moment the rotor can be coned backwards with a cone angle of θ_{cone} as shown in Figure 13.3.

The centrifugal force acting on the incremental part of the blade at a radius r from the rotational axis as shown in Figure 13.3 is $F_c = \omega^2 r m dr$, where mdr is the mass of the incremental part and ω the angular velocity of the rotor. Due to the coning, the centrifugal force has a component in the spanwise direction of the blade $F_c \cos\theta_{cone}$ and a component normal to the blade $F_c \sin\theta_{cone}$ as shown in Figure 13.3. The normal component gives a flapwise bending moment in the opposite direction of the bending moment caused by the thrust and thus reduces the total flapwise bending moment.

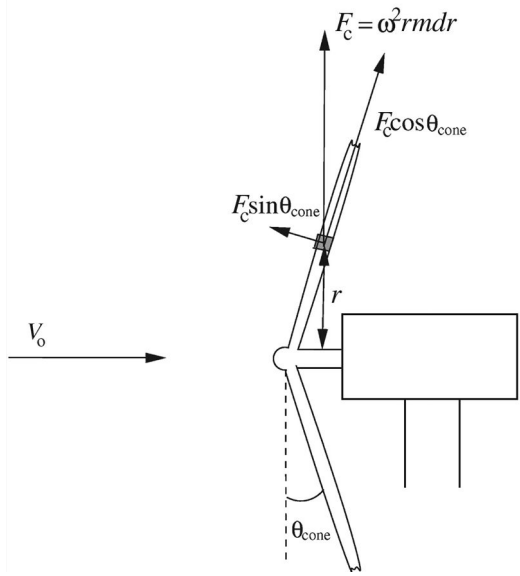

Figure 13.3 Effect of coning the rotor

Aerodynamic loading

The aerodynamic loading is caused by the flow past the structure, i.e. the blades and the tower. The wind field seen by the rotor varies in space and time due to atmospheric turbulence as shown in Figure 13.4.

As also seen in Figure 13.4, the wind field is characterized by shear; that is the mean wind speed increases with the height above the ground. For neutral stability this shear may be estimated as:

$$\frac{V_{10\,\mathrm{min}}(x)}{V_{10\,\mathrm{min}}(h)} = \frac{\ln(x/z_o)}{\ln(h/z_o)} \tag{13.3}$$

$V_{10\,\mathrm{min}}(x)$ is the time averaged value for a period of 10 minutes at a height x above the ground. $V_{10\,\mathrm{min}}(h)$ is the time averaged value at a fixed height h, and z_o is the so-called roughness length. Alternatively the wind shear can be given by an exponent as in Equation 9.33. The roughness length depends on the surface characteristics and varies from 10^{-4}m over water to approximately 1 m in cities. Values of z_o can be found in Troen and Petersen (1989) and is summarized in Table 13.1.

Wind shear gives a sinusoidal variation of the wind speed on a blade with a frequency corresponding to the rotation of the rotor 1P. The turbulent fluctuations superimposed on the mean wind speed also give a time variation in the wind speed and thus in the angle of attack. In order to simulate the behaviour of a wind turbine using an aeroelastic code, it is therefore necessary first to

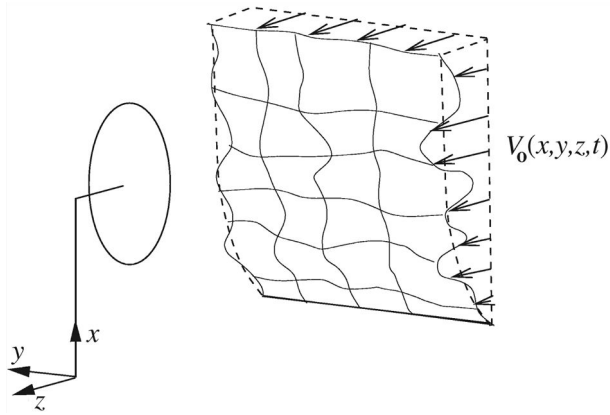

Figure 13.4 Sketch of turbulent inflow seen by wind turbine rotor.

Table 13.1 Roughness length table from Troen and Petersen (1989)

z_o [m]	*Terrain surface characteristics*
1.0	City
0.8	Forest
0.2	Many trees and bushes
0.1	Farmland with closed appearance
0.05	Farmland with open appearance
0.03	Farmland with very few buildings, trees, etc.
5×10^{-3}	Bare soil
1×10^{-3}	Snow surface
3×10^{-4}	Sand surface (smooth)
1×10^{-4}	Areas of water

generate a realistic wind field as for example shown in Chapter 14. Also the tower gives a variation of the inflow that for an upwind rotor can be calculated using Equations 9.34 to 9.36.

A wind turbine might operate in yaw, for example if the direction of the wind is not measured correctly or in the case of a malfunctioning yaw system. In this case, the reduced wind speed u at the rotor plane has a component normal to the rotor $u\cos\theta_{yaw}$ and tangential to the rotor $u\sin\theta_{yaw}$. If the blade at the top position corresponding to $\theta_{wing}=0^{o}$ in Figure 13.5 moves in same direction as the wind, the relative rotational speed $\omega r(1+a')$ is reduced by $u\sin\theta_{yaw}$, and at the bottom position $\theta_{wing}=180^{o}$ it will move against the wind speed, and the relative rotational speed is increased with $u\sin\theta_{yaw}$. Further, the axial-induced velocity, and thus the axial velocity u, is not constant in an annular element of the rotor disc, see Equation 9.26.

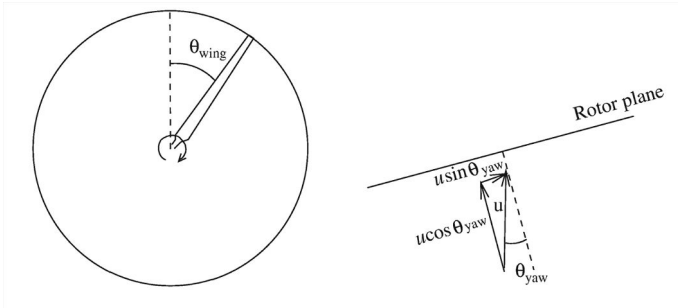

Figure 13.5 Rotor plane showing the azimuthal position of a blade and a yawed rotor plane seen from the top

For pure yaw the relative rotational speed varies sinusoidally as $\omega r(1+a') - u\sin\theta_{yaw}\cos\theta_{wing}$. Therefore both the relative velocity seen by the blade and the angle of attack varies with the frequency of the rotor, ω. The loads therefore also vary in yaw and will therefore contribute to the fatigue loads and thus influence the expected lifetime of the rotor. It should now be clear that the rotor blades experience a variation of the angle of attack due to turbulence, wind shear, tower passage and yaw/tilt. The forces and moments on the blades and thus on the entire structure will therefore also vary in time. Since a wind turbine is designed to last at least 20 years it is very important to quantify the loads in order to be able to perform a reliable fatigue analysis.

To make a wind turbine last in the design period, one must also take situations like extreme wind speeds into account. In this case the blades are parked or idling and, for example, in the Danish standard (DS412, 1992) is described how to compute the extreme loads as:

$$p(r) = q_{2s} C_f c(r) \tag{13.4}$$

where C_f is a force coefficient, $c(r)$ the chord and q_{2s}=½ρV^2_{2s} the dynamic pressure from an extreme wind speed time averaged over 2 seconds. For a Danish homogeneous terrain V_{2s} can be computed using:

$$V_{2s} = V_b k_t (\ln(\frac{h}{z_o}) + 3) = V_{10\min} + 3\sigma \tag{13.5}$$

where V_b=27m/s is a basis wind speed, h the height above the ground (minimum 4m), z_o the roughness length and k_t a terrain factor. σ is the standard deviation in a 10-minute time series. The terrain factor k_t is related to the roughness length z_o as in Table 3.2.

The extreme wind speed time averaged over 10 minutes can be estimated from:

$$V_{10\min} = V_b k_t \ln(\frac{h}{z_o}) \tag{13.6}$$

Table 13.2 Terrain factor as a function of roughness height

z_o [m]	k_t
0.004	0.16
0.010	0.17
0.050	0.19
0.300	0.22

In the following simplified example is shown how to quantify extreme loads on wind turbine blades. In the Danish standard DS472 (1992) for loads and safety of a wind turbine construction it is stated that for the blades the extreme wind speed V_{2s} must be calculated at $h=h_{hub}+2/3R$ using $C_f=1.5$. For a wind turbine with a hub height of 40m and a rotor radius of 20m this corresponds to $h=40+2/3\times20=53.3$m. If the surrounding landscape has no nearby obstacles such as houses and has very low-growing vegetation, the roughness length is approximately 0.01m and the terrain factor $k_t=0.17$. In this case $V_{2s}=27\times0.17\ (\ln(53.3/0.01)+3)=53.2$m/s. Assuming that the chord, c, is constant 1.3m and the density is 1.28kg/m^3, the load is according to equation (13.4) $p=½\times1.28\times53.2^2\times1.3\times1.5=3532$ N/m. The root bending moment at $r=3$m for the constant load then becomes:

$$M=\int_r^R rp(r)dr=\tfrac{1}{2}p(R^2-r^2)=\tfrac{1}{2}3532(20^2-3^2)=690533\text{Nm} \tag{13.7}$$

For a simplified structural cross section as the one shown in Figure 13.6 the moment of inertia about the flapwise axis is:

$$I=\frac{1}{12}a((2b_1)^3-(2b_2)^3)=\frac{2}{3}a(b_1^3-b_2^3) \tag{13.8}$$

Further it is assumed that $E=14$Gpa$=14\times10^9$ N/m^2 and that the thickness of the airfoil is $t/c=35\%$. The thickness is thus $t=(t/c)\times c=0.35\times1.3$m $=0.455$m and $b_1=t/2=0.228$m.

Given the extreme wind speed, the thickness of the airfoil and E, it is possible to estimate the necessary shell thickness $t_s=b_1-b_2$ so that the blade does not break off in this section.

Since the force in the tangential direction is small, Equation 11.10 reduces to:

$$\varepsilon=\frac{M}{EI}y \tag{13.9}$$

and it is clear that the maximum strain occurs for $y=b_1$. From testing it has been found that the material used in this example fails for $\varepsilon=\varepsilon_{fail}=0.02$. The necessary moment of inertia can now be estimated from Equation 13.9 as:

$$I=\frac{M}{E\varepsilon_{fail}}b_1=\frac{690533}{14\cdot10^9\cdot0.02}0.228=5.62\cdot10^{-4}m^4 \tag{13.10}$$

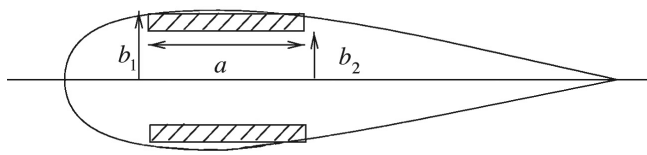

Figure 13.6 Simplified structural model

Using this necessary moment of inertia in Equation 13.8, b_2 can be found for a=0.5m:

$$b_2 = (b_1^3 - \frac{3I}{2a})^{1/3} = (0.228^3 - \frac{3 \cdot 5.62 \cdot 10^{-4}}{2 \cdot 0.5})^{1/3} = 0.217m \qquad (13.11)$$

The necessary shell thickness is thus t_s=b_1–b_2=0.228–0.217=0.011m=1.1cm. In the standard DS472 (1992) is stated that the method outlined above can only be applied if the construction is assumed not to auto-vibrate. The ultimate and fatigue load cases that must be verified for modern large wind turbines are described in standards/norms such as IEC 61400 (2004) or DNV-OS-J101 (2010).

References:

DNV-OS-J101 (2010) *Design of Offshore Wind Turbine Structures*, Det Norske Veritas.

DS 472 (1992) Dansk Ingeniørforenings og ingeniørsammenslutningens *Norm for, 'Last og sikkerhed for vindmøllekonstruktioner'* (in Danish).

IEC (2004) 'Wind Turbines. Part 1: Design requirements', 61400-1 Ed.3 CD. Second revision IEC TC88-MT1. Geneva: IEC.

Troen, I. and Petersen, E.L. (1989) *European Wind Atlas*, Roskilde: Risø National Laboratory.

14 Wind simulation

To calculate realistic time series of the loads on a wind turbine construction, as shown in Figure 10.2 for example, it is important to have as input a wind field with a correct spatial and temporal variation as shown in Figure 13.4. This variation should include turbulence, wind shear and the effect on the wind from the tower .The following describes some of the statistical properties of atmospheric turbulence and how to model a 3-D wind field.

Wind simulation in one point in space

A simple anemometer measures the wind speed in one point with a sample frequency of $f_s = 1/\Delta t$, where Δt is the time between two measurements. The output is a list of numbers, u_i i=1, …, N, where the corresponding time is $t = 1 \cdot \Delta t, 2 \cdot \Delta t, \ldots, N \cdot \Delta t$. The total time is T=$\Delta t \cdot N$ and the sample frequency is f_s=N/T. An example of such a time history is shown in Figure 14.1.

Figure 14.1 shows that the highest frequency that can be resolved is f_h=$f_s/2$=$(N/2)/T$ since three discrete points are needed as a minimum to describe a vibration. The lowest frequency that can be resolved is f_{low}=$1/T$. If the signal is assumed to be periodical, the time history can be decomposed using a discrete Fourier transformation as:

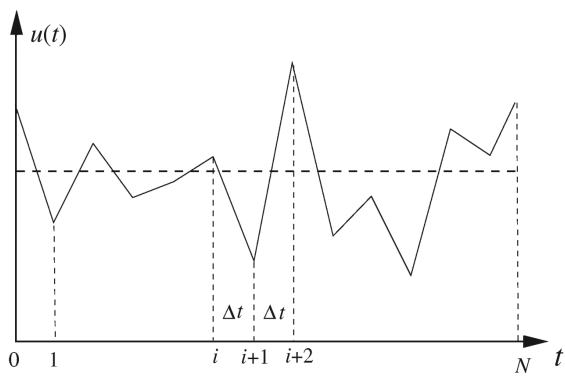

Figure 14.1 Time history of discrete sampled wind speed at 1 point

$$u(t) = a_o + \sum_{n=1}^{N/2} a_n \cos(\omega_n t) + b_n \sin(\omega_n t), \quad \omega_n = \frac{2\pi n}{T} \tag{14.1}$$

The coefficients are found as:

$$a_o = \frac{1}{N}\sum_{i=1}^{N} u_i \quad \text{(mean wind speed)} \tag{14.2}$$

$$a_n = \frac{2}{N}\sum_{i=1}^{N} u_i \cos(\frac{2\pi n}{N} i), \quad n = 1, \frac{N}{2} - 1 \tag{14.3}$$

$$b_n = \frac{2}{N}\sum_{i=1}^{N} u_i \sin(\frac{2\pi n}{N} i), \quad n = 1, \frac{N}{2} - 1 \tag{14.4}$$

$$a_{\frac{N}{2}} = \frac{1}{N}\sum_{i=1}^{N} u_i \cos(\pi i) \tag{14.5}$$

$$b_{\frac{N}{2}} = 0 \tag{14.6}$$

Putting Equation 14.1 into the definition of the variance, the following relationship can be proved:

$$\sigma^2 = \frac{1}{N}\sum_{i=1}^{N} (u_i - \overline{u})^2 = \frac{1}{2}\sum_{n=1}^{N/2-1} (a_n^2 + b_n^2) + a_{\frac{N}{2}}^2 \tag{14.7}$$

For the power spectral density function $PSD(f)$ the variance is

$$\sigma^2 = \int_0^\infty PSD(f)df \tag{14.8}$$

where f is the frequency. Discretizing the integral 14.8, knowing that the frequencies lie between $f_{low}=1/T$ and $f_{N/2}=(N/2)/T$, yields (see Figure 14.2):

$$\sigma^2 \approx \sum_{n=1}^{N/2} PSD(f_n)\Delta f, \quad f_n = \frac{\omega_n}{2\pi} = \frac{n}{T} \tag{14.9}$$

Comparing Equations 14.9 and 14.7, it can be seen that the power spectral density function $PSD(f)$ can be evaluated as:

$$PSD(f_n) = \frac{1}{2\Delta f}(a_n^2 + b_n^2) = \frac{T}{2}(a_n^2 + b_n^2) \tag{14.10}$$

From a measured time series, u_1, …, u_N, the Fourier coefficients and thus the power spectral density function can be determined from Equations 14.3, 14.4 and 14.10. This method is called the discrete Fourier transform (DFT).

Constructing a time series from a known *PSD* function is known as the inverse DFT. For the atmospheric boundary layer different analytical expressions to approximate measured *PSD* functions exist, e.g. a Kaimal spectrum as stated in DS472 (1992):

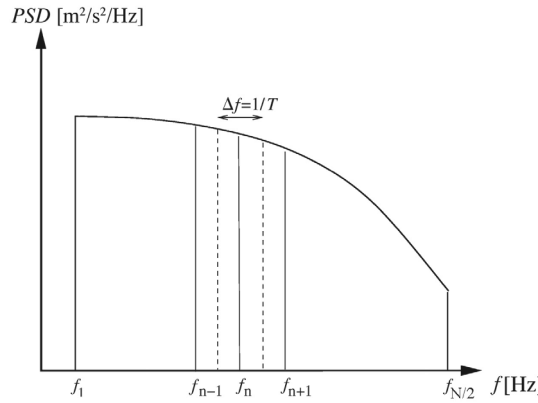

Figure 14.2 Power spectral density function

$$PSD(f) = \frac{I^2 V_{10\min} l}{(1+1.5\frac{f \cdot l}{V_{10\min}})^{5/3}} \tag{14.11}$$

$I=\sigma/V_{10min}$ is the turbulence intensity, f is the frequency [Hz], V_{10min} is the 10 minutes averaged wind speed, l is a length scale, $l=20\,h$ for $h<30$ m and $l=600$ m for $h>30$ m, where h is the height above ground level. The inverse DFT should provide a Fourier transform as shown below which satisfies the prescribed *PSD* function:

$$u(t) = \overline{u} + \sum_{n=1}^{N/2} a_n \cos(\omega_n t) + b_n \sin(\omega_n t) \tag{14.12}$$

Equation 14.12 can be rewritten as:

$$u(t) = \overline{u} + \sum_{n=1}^{N/2} \sqrt{a_n^2 + b_n^2} \cos(\omega_n t - \varphi_n) \tag{14.13}$$

where φ_n is the phase angle at frequency ω_n. Replacing the term $\sqrt{a_n^2 + b_n^2}$ by $\sqrt{2PSD(f_n)/T}$ in Equation 14.13 using, for example, Equation 14.11 for the spectrum yields a Fourier transform that exactly satisfies the prescribed *PSD* function:

$$u(t) = \overline{u} + \sum_{n=1}^{N/2} \sqrt{\frac{2PSD(\omega_n)}{T}} \cos(\omega_n t - \varphi_n) \tag{14.14}$$
$$t = i \cdot \Delta t \text{ for } i = 1,\ldots,N$$

The phase angle φ_n is not reflected in the *PSD* function and can be modelled using a random number generator yielding a value between 0 and 2π.

Using Equation 14.14 it is very easy to compute a discrete time series having exactly the prescribed *PSD* function. These functions assume that all frequencies between 0 and ∞ are present, but, as described earlier, only frequencies between $1/T$ and $(N/2)/T$ are present for the discrete time series. It is therefore practical to scale the *PSD* function as:

$$\int_{f=1/T}^{f=(N/2)/T} PSD(f)df = 1 \tag{14.15}$$

corresponding to a standard deviation of 1, i.e. a turbulent intensity of $I=1/V_{10\text{min}}$. A standard deviation of S and thus a turbulent intensity of $I=S/V_{10min}$ can be found simply as:

$$u_i - \overline{u} = S(u_i - \overline{u}) \tag{14.16}$$

or

$$u_i = Su_i + (1 - S)\overline{u} \tag{14.17}$$

In Burton et al. (2001) and Rohatgi and Nelson (1994), more information can be found on different spectrums such as the Kaimal and von Karman spectrums.

3D wind simulation

To simulate a time history of the wind speed in two or more points in space, it must also be considered that the time histories are not independent. This dependency is of course related to the physical distance between two points, but also on the frequency. The high frequency content of the time series is a result of small vortices, which have small spatial influence. Similarly the low frequency part is related to large-scale vortices covering a bigger volume of the flow. A coherence function must therefore take into account both the distance, L, between points j and k and the frequency, and one possible choice is stated in DS472 (1992):

$$coh_{jk}(L, f) = \exp(-12(fL / V_{10\,\text{min}})) \tag{14.18}$$

Veers (1988) shows a method that will generate a 3D wind field with a prescribed *PSD* function and coherence function. In the following, the method will not be proved but only given as an algorithm.

First a matrix, S_{jk}, is created:

$$S_{jk} = coh_{jk}\sqrt{S_{jj} \cdot S_{kk}} \tag{14.19}$$

where S_{jj} and S_{kk} are the *PSD* functions of points j and k, respectively. The off-diagonal terms are the magnitudes of the cross spectrums. If the number of points in space is NP, S_{jk} is an $NP \times NP$ matrix.

Second a lower triangular **H** matrix is computed through following recursive formulae:

$$
\begin{aligned}
H_{11} &= S_{11}^{1/2} \\
H_{21} &= S_{21} / H_{11} \\
H_{22} &= (S_{22} - H_{21}^2)^{1/2} \\
H_{31} &= S_{31} / H_{11} \\
&\vdots \\
H_{jk} &= (S_{jk} - \sum_{l=1}^{k-1} H_{jl} H_{kl}) / H_{kk} \\
H_{kk} &= (S_{kk} - \sum_{l=1}^{k-1} H_{kl}^2)^{1/2}
\end{aligned}
\tag{14.20}
$$

For each point indexed by k and for each discrete frequency, $f_m = m/T$, a random number, φ_{km}, between 0 and 2π is found to represent the phase as in Equation 14.14. m varies between 1 and $N/2$, where N is the number of discrete points in the time histories ($t = i \cdot \Delta t$, $i = 1, \ldots, N$).

A vector with imaginary components of length equal to the number of points in space $\mathbf{V} = V_j(f_m)$ is now calculated as:

$$
\begin{aligned}
\mathrm{Re}(V_j(f_m)) &= \sum_{k=1}^{j} H_{jk} \cos(\varphi_{km}) \\
\mathrm{Im}(V_j(f_m)) &= \sum_{k=1}^{j} H_{jk} \sin(\varphi_{km})
\end{aligned}
\tag{14.21}
$$

$\mathrm{Re}(V_j(f_m))$ and $\mathrm{Im}(V_j(f_m))$ is transformed to an amplitude, $Amp_j(f_m)$, and a phase $\Phi_j(f_m)$ as:

$$
\begin{aligned}
Amp_j(f_m) &= \sqrt{\mathrm{Re}(V_j(f_m))^2 + \mathrm{Im}(V_j(f_m))^2} \\
\tan \Phi_j(f_m) &= \frac{\mathrm{Re}(V_j(f_m))}{\mathrm{Im}(V_j(f_m))}
\end{aligned}
\tag{14.22}
$$

Finally the time histories in the points $j = 1, NP$ can be computed as:

$$
\begin{aligned}
U_j(t) &= \bar{U} + \sum_{m=1}^{N/2} 2 Amp_j(f_m) \cos(2\pi f_m \cdot t - \Phi_j(f_m)) \\
t &= i \cdot \Delta t \; for \; i = 1, \ldots, N
\end{aligned}
\tag{14.23}
$$

In Figure 14.3 the time series of two points spaced 1 m apart is plotted. The mean wind speed is 10 m/s and the turbulence intensity is 0.1. It is clearly seen that the two curves are well correlated for the lower frequencies. In Figure 14.4 the coherence function computed from the two time series shown in Figure 14.3 is plotted together with the input given by Equation 14.18.

Using Equation 14.23, together with appropriate *PSD* and coherence functions, the time histoies in all points are computed for each velocity component

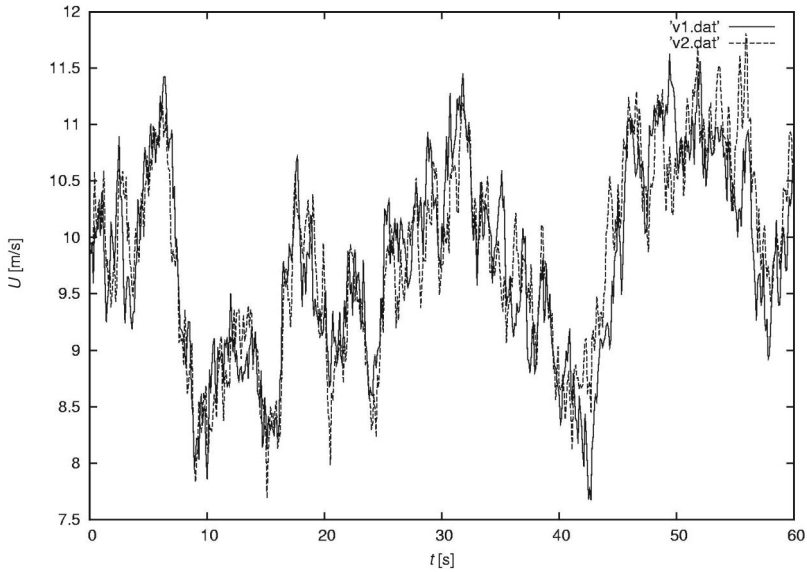

Figure 14.3 Computed time series of wind speed in two points separated 1 m. The mean wind speed is 10 m/s and the turbulence intensity is 0.1

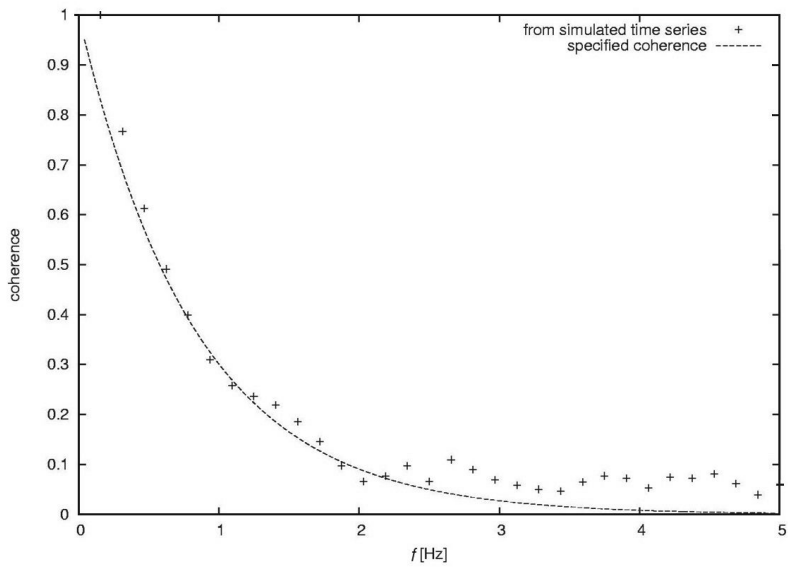

Figure 14.4 Comparison of actual coherence from the two time series shown in Figure 14.3 and specified by Equation 14.18

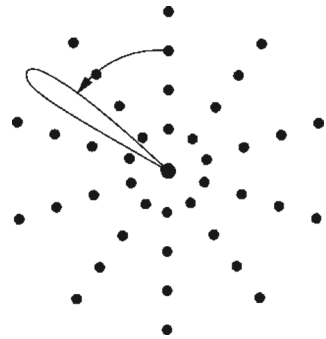

Figure 14.5 Point distribution for time histories of wind speed for aeroelastic calculation of wind turbine construction

$U=(u,v,w)$ independently. Therefore there is no guarantee for obtaining correct cross-correlations. In Mann (1998) a method ensuring this is developed on the basis of the linearized Navier–Stokes equations. In the future, wind fields are expected to be generated numerically from large eddy simulations (LES) or direct numerical simulations (DNS) of the Navier–Stokes equations for the flow on a landscape similar to the actual siting of a specific wind turbine.

For an aeroelastic calculation of a wind turbine construction it is natural to construct the time histories in a series of points arranged as indicated in Figure 14.5. The velocities on the blade sweeping through the grid must, in general, be found by spatial interpolation. It should be mentioned that the time history of the wind seen by a point on the blade is different from the time history of a point fixed in space. A time history for a point on the rotating blade is called rotational sampling and in Veers (1988) is shown how this can directly be calculated for a blade with a constant rotational speed.

To illustrate rotational sampling a number of time series is created for a constant radius of r= 5 m and azimuthally spaced 7.5 degrees. The velocity a blade at the same radius and rotating with ω=13.1 rad/s is found by interpolation from the time series. In Figure 14.6 the calculated *PSD* from the rotational sampling is plotted together with the *PSD* from a stationary point in space. The *PSD* for the rotating blade shows clear spikes at multiples of the rotational frequency 1P, 2P, … (The frequency in Figure 14.6 is non-dimensionalized with the rotational frequency of the rotor, $f_0=\omega/2\pi$.) These spikes that will contribute greatly to the fatigue damage to the wind turbine construction are due to the spatial coherence, since for a frozen time there exist areas of the rotor disc where the velocity is relatively high or low, see for example Figure 13.4, and a blade will pass these areas once per revolution.

Finally, it should be noted that simulated time series not only depend on the prescribed *PSD* and coherence functions, but also on the random numbers for the phases. Therefore it is recommended to calculate at least three different time series for each case and perform for each series a run with the aeroelastic code to have an idea of the uncertainty from the different time series.

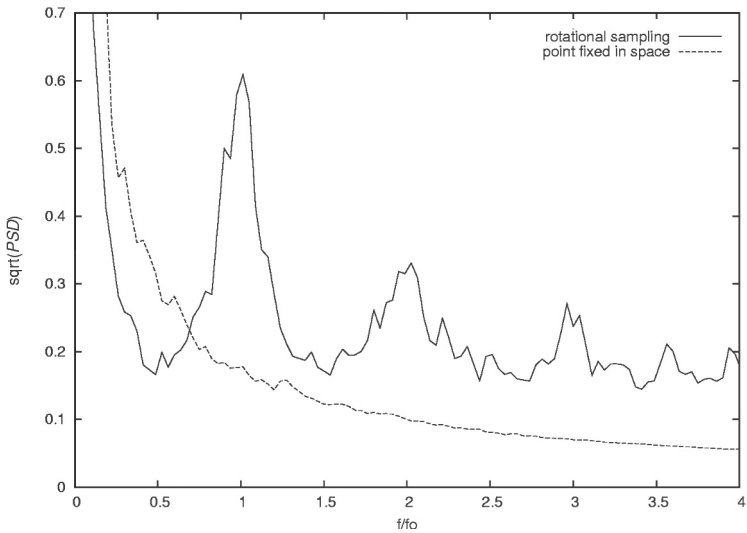

Figure 14.6 Comparison between specified PSD and the PSD acting on the rotating blade

References

Burton, T., Sharpe, D., Jenkins, N. and Bossanyi, E. (2001) *Wind Energy Handbook*, Chichester: John Wiley.

DS 472(1992) Dansk Ingeniørforenings og ingeniørsammenslutningens *Norm for, 'Last og sikkerhed for vindmøllekonstruktioner'* (in Danish).

Mann, J. (1998) 'Wind field simulation', *Problems in Engineering Mechanics*, 13: 269–282.

Rohatgi, J.S. and Nelson, V. (1994) *Wind Characteristics*, Canyon, TX: West Texas A&M University.

Veers, P. (1988) 'Three-Dimensional Wind Simulation', Sandia Report SAND88-0152 UC-261. Livermore, CA: Sandia National Laboratories.

15 Fatigue

From earlier chapters it is clear that the loads on a wind turbine vary constantly with time, giving rise to a possible breakdown due to accumulated fatigue damage. In Madsen et al. (1990), a recommended practice to estimate the fatigue damage, and thus the lifetime of a wind turbine, is outlined. In this chapter a summary of this practice is given.

First, the loads must be obtained from either computations using an aeroelastic code or directly from measurements. For normal operation the loads are monitored for 10 minutes for each wind speed interval $V_p<V_o<V_{p+1}$. An example of such a time history for $V_{10\text{min}}$=11m/s and a turbulence intensity I=0.1 is seen in Figure 10.2, which is a result of a simulation using the aeroelastic code FLEX. The turbulence intensity, I, is defined as $\sigma/V_{10\text{min}}$, where σ is the standard deviation of the wind speed within the 10-minute time series. Knowing the loads, the stresses at critical points on the wind turbine are computed using Equations 11.9 (Hooke's law) and Equation 11.10. As a minimum, it is recommended by Madsen et al. (1990) to monitor the blade bending moments, the yaw and tilt rotor moments, the axial thrust, the torque in the main shaft, the bending moments of the tower and the torsional moment in the tower. From each 10-minute time history the stresses are sorted in a matrix, where the elements m_{ij}($V_p<V_o<V_{p+1}$) denote the number of cycles in the mean stress interval $\sigma_{m,i} < \sigma_m < \sigma_{m,i+1}$ and range interval $\sigma_{r,j} < \sigma_r < \sigma_{r,j+1}$ for the wind speed interval $V_p<V_o<V_{p+1}$. In Figure 15.1 one cycle with a mean stress value σ_m and a range σ_r is shown and it is seen that the range is twice the amplitude σ_a.

To count the number of cycles from an actual time series such as the one shown in Figure 10.2, a technique called 'Rain flow counting' is used. For a complete description of this algorithm see Madsen et al. (1990). Then knowing the annual wind distribution $h_W(V_o)$, the probability, f, of the wind speed to be in the interval $V_p<V_o<V_{p+1}$ is computed from Equation 6.48. The actual number of annual 10-minute periods where the wind speed is in this interval is $6\times8760\times f$. The number of cycles per year n_{ij} in the mean stress interval $\sigma_{m,i} < \sigma_m < \sigma_{m,i+1}$ and in the range interval $\sigma_{r,j} < \sigma_r < \sigma_{r,j+1}$ is found by adding together the contributions from each wind speed interval:

$$n_{ij} = \sum_{p=1}^{N-1} m_{ij}(V_p < V_o < V_{p+1}) \cdot 6 \cdot 8760 \cdot f(V_p < V_o < V_{p+1}) \tag{15.1}$$

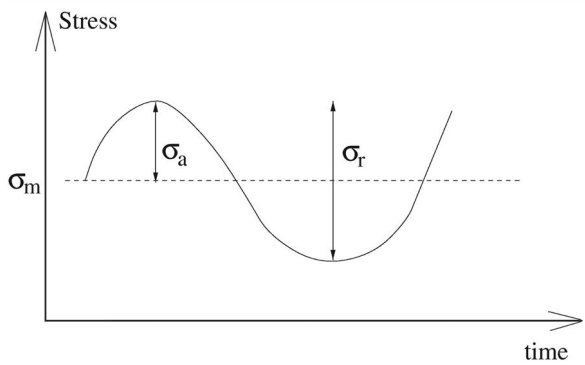

Figure 15.1 Definition of mean stress s_m and range s_r for one cycle

where N–1 is number of wind speed intervals. The matrix **M** with the elements n_{ij} is called the Markov matrix. A wind turbine also experiences loads when starting and stopping and when running under abnormal conditions such as operating at high yaw angles. Before a lifetime analysis can be performed, it is necessary also to estimate these loads with respect to the annual number of occurrences with a given mean stress interval $\sigma_{m,i} < \sigma_m < \sigma_{m,i+1}$ and range interval $\sigma_{r,j} < \sigma_r < \sigma_{r,j+1}$ and adding this to the Markov matrix n_{ij}. Doing this one has to distinguish between starting and stopping at high wind speed and low wind speed, since the loads are different in these two cases. In IEC 61400 (2004) a complete list of the different load cases needed for certification is stated. The total number of cycles in the entire lifetime within the mean stress interval $\sigma_{m,i} < \sigma_m < \sigma_{m,i+1}$ and range interval $\sigma_{r,j} < \sigma_r < \sigma_{r,j+1}$ is:

$$n_{tot,ij} = T \cdot n_{ij} \tag{15.2}$$

where the lifetime T is measured in years. To estimate T, the Palmgren–Miner rule, Equation 15.3, for cumulative damage during cyclic loading is used. This rule assumes that the ratio between the number of applied stress cycles n_{ij}, with a given mean stress level $\sigma_{m,i}$ and range $\sigma_{r,j}$, and the number of cycles N_{ij}, which with same mean stress and range would lead to failure, constitutes the expended part of the useful fatigue life, and the sum of these ratios are thus the damage D. So the criteria for not failing is that D is less than 1:

$$\sum \frac{n_{tot,ij}}{N_{ij}} = D < 1 \tag{15.3}$$

Combining Equation 15.2 with Equation 15.3 yields the following equation to estimate the lifetime T:

$$T = \frac{1}{\sum \frac{n_{ij}}{N_{ij}}} \tag{15.4}$$

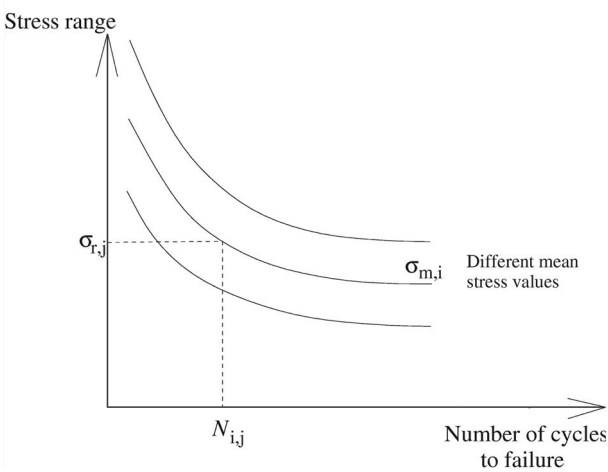

Figure 15.2 An *S–N* curve

The number of cycles N_{ij} leading to failure for a cyclic loading with a given mean stress level $\sigma_{m,i}$ and range $\sigma_{r,j}$ for a given material is found in an *S–N* curve or Wöhler curve such as that shown in Figure 15.2.

Sometimes only the range $\sigma_{r,j}$ is taken into account and the influence of the mean stress level $\sigma_{m,i}$ is ignored. The *S–N* curve can, under this assumption, be approximated by:

$$N = N^* \left(\frac{\sigma_r(N^*)}{\sigma_r} \right)^m \tag{15.5}$$

where m is a material constant and $\sigma_r(N^*)$ is the stress range giving failure for N^* cycles. For steel, m is according to DS 412 (1983) approximately 4.0. For glass fibre, m is approximately 8–12.

The damage D can be estimated using the Palmgren–Miner rule. To compare the contribution from the different wind speeds to the total fatigue damage, an equivalent, $\sigma_{r,eq}$, load can be used. The equivalent load is defined as the cyclic load which when applied n_{eq} times gives the same fatigue damage on the wind turbine as the real turbulent flow at the considered wind speed. Since the total damage, D, is known, the equivalent load can be calculated as using Equation 15.5 for the *S–N* curve:

$$D = \frac{n_{eq}}{N_{eq}} = \frac{n_{eq}}{N^* \left(\dfrac{\sigma_r(N^*)}{\sigma_{r,eq}} \right)^m}$$

$$\Downarrow \tag{15.6}$$

$$\sigma_{r,eq} = \sigma_r(N^*) \left(\frac{N^* D}{n_{eq}} \right)^{1/m}$$

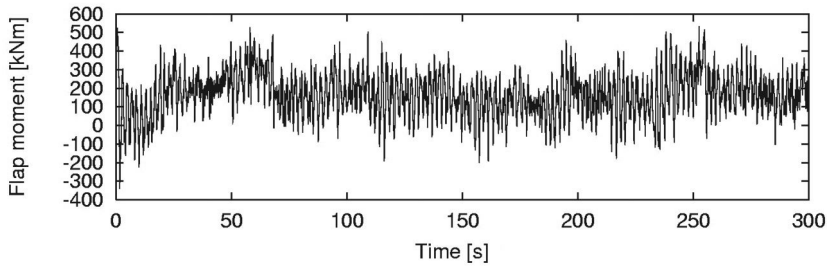

Figure 15.3 An example of a time history of a flapwise bending moment

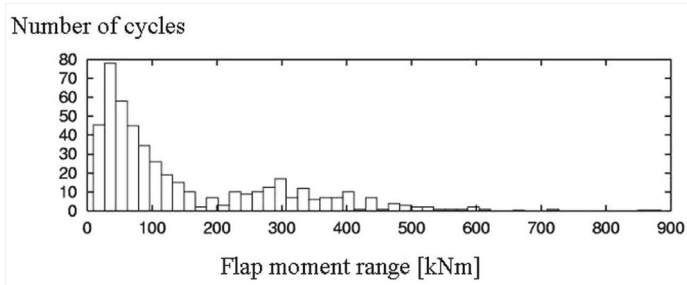

Figure 15.4 Result of using rain-flow counting on the time series from Figure 15.3.

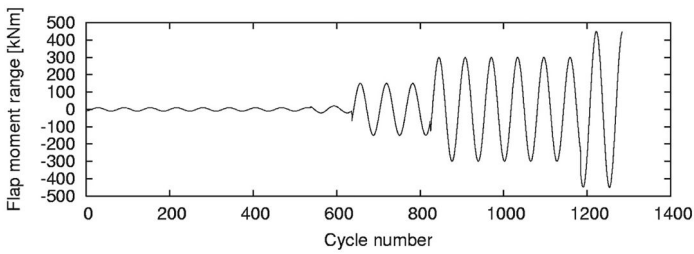

Figure 15.5 Sequence of cyclic loads with increasing range that gives the same fatigue damage as the original time series

In Figure 15.3 a time series of 300 s of a flapwise bending moment is plotted and in Figure 15.4 the result of using rain-flow counting on this signal, i.e. of the number of cycles with a given range, is shown.

A time series consisting of a sequence of cyclic loads with increasing range can be made that, assuming the Palmgren–Miner rule is correct, will give the same fatigue damage as the original time series. Such a time series is shown in Figure 15.5.

References

DS 412 (1983) *Dansk Ingeniørforenings norm for stålkonstruktioner* (*Danish standard for steel constructions*).

IEC (2004) 'Wind Turbines. Part 1: Design requirements', 61400-1 Ed.3 CD. Second revision IEC TC88-MT1. Geneva: IEC.

Madsen, P.H., Dekker, J.W.M., Thor, S.E., McAnulty, K., Matthies, H. and Thresher, R.W. (1990) *Expert Group Study on Recommended Practices for Wind Turbine Testing and Evaluation 3. Fatigue Loads*, 2nd edn, IEA Wind Energy Conversion Systems. Available online at https://www.ieawind.org/publications/Archive/recPract/1990%20Recommended%20Practice%20Fatigue%20Loads.pdf (last accessed 3 January 2015).

16 Vertical-axis wind turbines

Even though most installed large wind turbines are of the propeller type horizontal-axis wind turbine, this chapter is, for completeness, devoted to explaining some of the aerodynamics of vertical-axis wind turbines (VAWTs). The geometry of VAWTs is a shaft placed vertically on which is attached rotating blades (Figure 16.1). If the blades are mounted as in Figure 16.1a it is called a Darrieus wind turbine and if it is as in Figure 16.1b it is often called a Gyro wind turbine.

In Figure 16.1 is also drawn a section A–A, in the equatorial plane of the Darrieus rotor. Figure 16.2 shows this section as seen from above for a one-bladed rotor together with the velocity triangle of the rotating blade, when the induced velocity is ignored. Also a global and fixed coordinate system x–y is shown and the blade position is given by the azimuthal angle θ.

The relative velocity experienced by the blade when ignoring the induced velocity is the vector sum of the rotational velocity tangent to the path of the blade and the incoming free wind and in the x–y coordinate systems becomes

$$\begin{aligned} V_{rel,x} &= V_o + \omega r \cos\theta \\ V_{rel,y} &= \omega r \sin\theta \end{aligned} \tag{16.1}$$

The relative wind may also be composed normal to and tangential to the blade path as

$$\begin{aligned} V_{rel,t} &= r\omega + V_o \cos\theta \\ V_{rel,n} &= V_o \sin\theta \end{aligned} \tag{16.2}$$

And from these the angle of attack can be calculated as

$$\begin{aligned} \tan\alpha &= \frac{V_{rel,n}}{V_{rel,t}} = \frac{\sin\theta}{\lambda + \cos\theta} \\ \lambda &= \frac{\omega r}{V_o} \end{aligned} \tag{16.3}$$

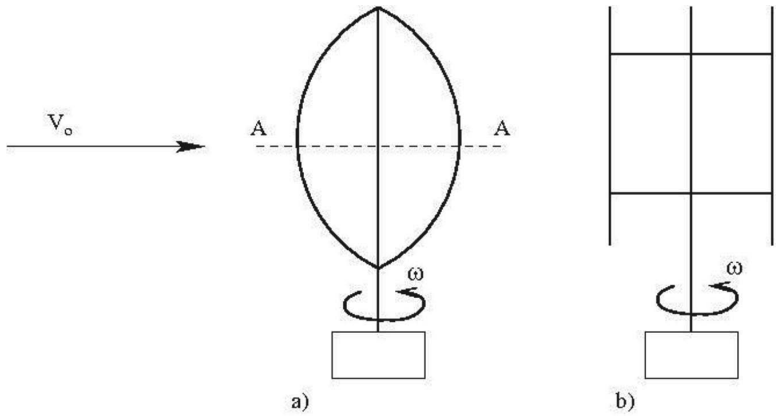

Figure 16.1 Two different VAWT geometries: a) Darrieus type, b) Gyro wind turbine

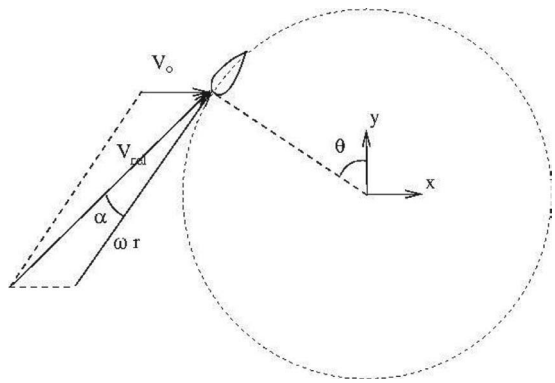

Figure 16.2 The section A–A from Figure 16.1 seen from above for a one-bladed VAWT and the relative velocity of a blade when ignoring the induced wind

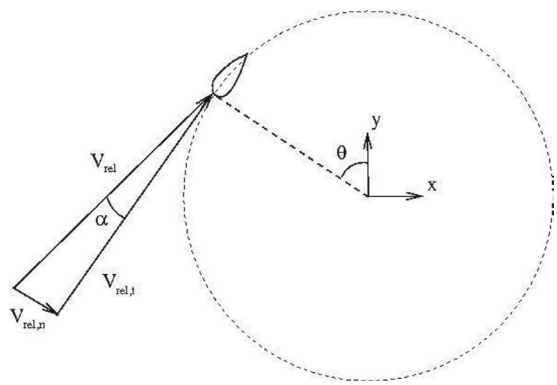

Figure 16.3 The section A–A from Figure 16.1 seen from above for a one-bladed VAWT showing the normal and tangential components of the relative wind ignoring the induced wind speed

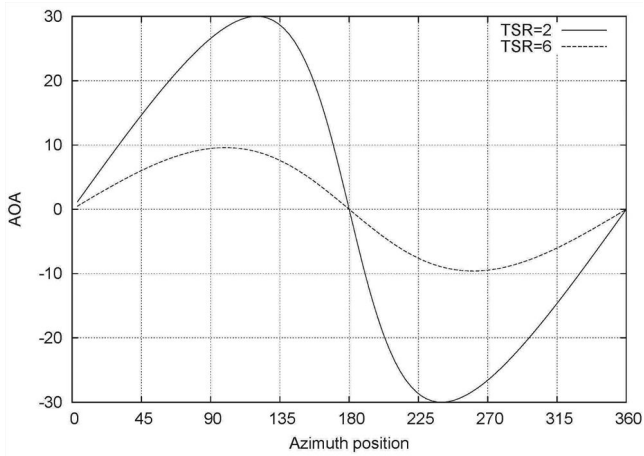

Figure 16.4 The variation of the angle of attack as function of the azimuthal blade position for tip speed ratio 2 and 6 ignoring the induced velocity.

In Figure 16.4 the angle of attack calculated from Equation 16.3 for different tip speed ratios is plotted and one can easily see that the variation of the angle of attack per revolution is quite large depending on the tip speed ratio, λ, and varies between positive and negative values.

These periodically changing angles of attack are one of the main drawbacks of VAWTs since this gives rise to large and numerous load cycles during the expected lifetime, and the design must be carefully designed to withstand these fatigue loads. Further, to design a mechanism that can pitch the blades so to stop the rotor in high wind speeds or in the case of lost generator torque is challenging. However, on the positive side it should be mentioned that VAWTs work for all wind directions; that is, no yaw mechanism is needed.

Also a VAWT must slow down the incoming wind speed in order to transform kinetic energy in the wind to useful power. That is, a thrust force must exist with a direction opposite to the wind, and this force will be responsible for an induced velocity at the rotor that must also be considered when setting up the velocity triangle. Assuming that the wind direction is along the positive x-direction in the global coordinate system shown in Figure 16.3 and that the induced velocity only has a component in the thrust direction, the relative velocity at a blade section is determined as

$$\begin{aligned} V_{rel,x} &= V_o + \omega \cdot y - W_x \\ V_{rel,y} &= -\omega \cdot x \\ V_{rel}^2 &= V_{rel,x}^2 + V_{rel,y}^2 \end{aligned} \tag{16.4}$$

If the position of the blade is given by the azimuthal angle θ, as shown in Figure 16.5, the relative wind speed can be decomposed into a direction normal to and tangential to the rotor plane as

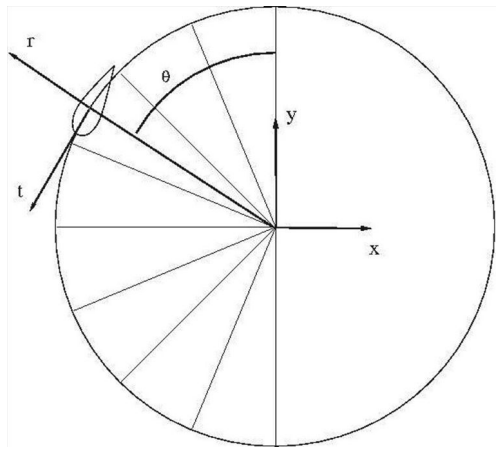

Figure 16.5 Azimuthal blade position and global coordinate system for a VAWT

$$\begin{aligned} V_t &= -V_{rel,y}\sin\theta - V_{rel,x}\cos\theta = r\omega + (V_o - W_x)\cos\theta \\ V_r &= V_{rel,y}\cos\theta - V_{rel,x}\sin\theta = (V_o - W_x)\sin\theta \end{aligned} \tag{16.5}$$

In Equation 16.5 W_x is assumed to be a positive value.

The flow angle and thus also the angle of attack can now be calculated as

$$\begin{aligned} \tan\phi &= \frac{V_r}{V_t} \\ \alpha &= \phi - \theta_p \quad \text{(for most VAWTs } \theta_p = 0\text{)} \end{aligned} \tag{16.6}$$

And finally the aerodynamic loads (lift, drag and tangential) can be found from the size of the relative wind speed and tabulated airfoil data for the applied airfoil data

$$\begin{aligned} l &= \tfrac{1}{2}\rho V_{rel}^2 c C_l(\alpha, \mathrm{Re}) \\ d &= \tfrac{1}{2}\rho V_{rel}^2 c C_d(\alpha, \mathrm{Re}) \\ p_t &= l\sin\phi - d\cos\phi \end{aligned} \tag{16.7}$$

The tangential loads yields for the blade considered in Figure 16.5 at an azimuthal position, θ, an aerodynamic torque on the shaft per unit length of $M=p_t \cdot r$, where r is the distance from the rotating shaft to the blade and, to find the total torque, the contribution from all the other blades must added. Finding the torque using Equations 16.4–16.7 requires, however, that the axial induced velocity W_x in Equation 16.4 is known and to do so the axial momentum equation is used. First the rotor is divided into N streamtubes indicated with the dashed lines in Figure 16.6 specified through a division of the upstream part of the rotor in slices of equal angular size $\Delta\theta=180^o/N$.

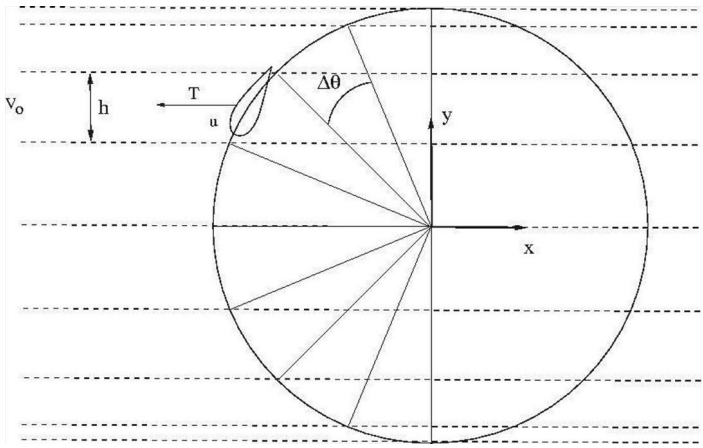

Figure 16.6 Distribution and size of streamtubes (area between dashed lines) on a VAWT. The way the streamtubes are distributed, the width, *h*, is small at the edge of the rotor and largest directly upstream

The total loading in the *x*-direction is the sum of the loading from both the upstream and downstream intersection of the rotor path with the streamtube. The force in the *x*-direction gives the total thrust and can be found as the loading in the *x*-direction multiplied with length of the blades Δz as

$$T = \overline{p}_x \Delta z \tag{16.8}$$

The bar over the axial loading indicates that it is a mean value since a blade is only inside the section a fraction of the time per revolution. The loading when a blade is inside a section is (see also Figure 16.7)

$$\begin{aligned} p_x &= l\cos\beta + d\sin\beta = l\frac{V_{rel,y}}{V_{rel}} + d\frac{V_{rel,x}}{V_{rel}} \\ p_y &= -l\sin\beta + d\cos\beta = -l\frac{V_{rel,x}}{V_{rel}} + d\frac{V_{rel,y}}{V_{rel}} \end{aligned} \tag{16.9}$$

Equation 16.9 is valid for both the upstream and downstream part of the streamtube shown in Figure 16.6, but the induced velocity, W_x, to compute the relative velocity from Equation 16.4 is different whether it is the up- or downstream part. It is *assumed* that the induction from the total thrust is present at the plane $x=0$ and $-r<y<r$. Further, a streamwise gradient of the induced velocity is *assumed* as

$$\frac{dW_x}{dx} = K\frac{W_x}{r} \tag{16.10}$$

and thus the up- and downstream value becomes

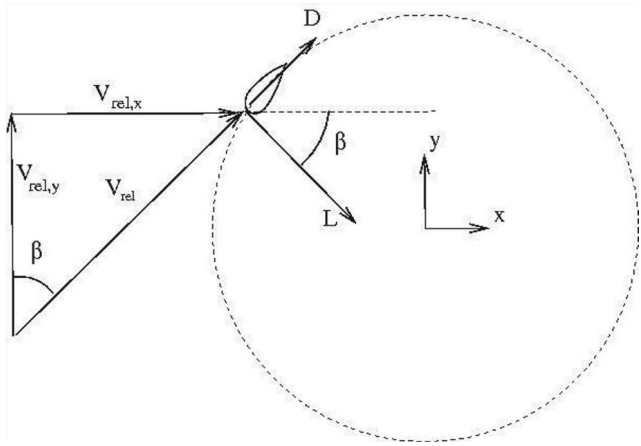

Figure 16.7 Another way of setting up the velocity triangle for a blade in a VAWT

$$W_x(\theta) = W_x - \frac{dW}{dx}\left|r\sin\theta\right| = W_x(1 - K\sin\theta) \quad 0 \le \theta \le 180$$
$$W_x(\theta) = W_x + \frac{dW}{dx}\left|r\sin\theta\right| = W_x(1 + K\left|\sin\theta\right|) \quad 180 < \theta < 360 \tag{16.11}$$

$\left|r\sin\theta\right|$ is the streamwise distance between the midplane and the upstream and downstream part of the rotor within the streamtube and K is a constant that needs to be calibrated. By comparing the load distributions with a vortex-based method (see Figures 16.11 and 16.12) it is found that the value of K is around 0.3. The total axial loading for each streamtube is the sum of the upstream and downstream loading, both calculated from Equation 16.9 but with different values of the induced velocities. Next, this loading has to be reduced since for every revolution a blade is only inside the streamtube a fraction of the time per revolution. The time for one rotation is, $T=2\pi/\omega$, and the time it takes one blade to go through a streamtube is $\Delta t=\Delta\theta/\omega$, and since the number of blades is B, the fraction of time that a blade is inside a streamtube becomes $frac=B\Delta t/T=B\Delta\theta/2\pi$ and thus the mean axial loading becomes

$$\overline{p}_x = frac \cdot p_x = \frac{B \cdot \Delta\theta}{2\pi} p_x \tag{16.12}$$

The thrust coefficient for a streamtube becomes

$$C_T = \frac{\overline{p}_x \Delta z}{\frac{1}{2}\rho V_o^2 h \Delta z} = \frac{\overline{p}_x}{\frac{1}{2}\rho V_o^2 h} \tag{16.13}$$

And with that an axial induction factor can be estimated from the empirical Glauert relationship as also given in Chapter 6.

$$C_T = \begin{cases} 4a(1-a) & a < \frac{1}{3} \\ 4a(1-\frac{1}{4}a(5-3a)) & a > \frac{1}{3} \end{cases} \tag{16.14}$$

And finally the axial induction factor can be related to axial induction as

$$W_x = a \cdot V_o \tag{16.15}$$

To sum up the loads may be computed as follows for each streamtube:

1 the unknown induced axial velocity W_x is guessed;
2 Equations 16.4–16.12 are used to determine the loads on the section inside the streamtube based on W_x;
3 using Equations 16.13–16.15 the value of the induced wind W_x is recalculated based on the loads determined in step 2;
4 if this value is different from the previous value go back to step 2.

Figure 16.8 shows the computed power coefficient as function of tip speed ratio for a three-bladed gyro turbine for various solidities $S=Bc/r$ using the described algorithm and the airfoil data from Table 16.1. The area used for the power coefficient is the frontal area seen by the incoming wind $A=2r \cdot H$, where H is the height of the rotor. It is seen that the trend is that the maximum power coefficient up to a certain value increases with increasing solidity but the range of tip speed ratio where the rotor performs well becomes narrower.

An alternative to the single disc approach described above is the so-called double-disc streamtube model, that models the flow as if there are two rotors, one standing in the wake of the other. For more details about the so-called double multiple streamtube (DMS) model see Paraschivoiu (2002) and Strickland (1975).

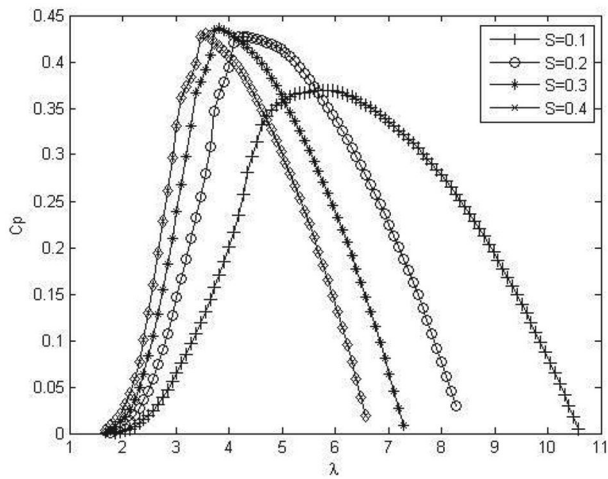

Figure 16.8 Computed power coefficient for gyro-type VAWT using Equations 16.4–16.15 and airfoil data from Table 16.1

Table 16.1 Airfoil data used in the computation of Figure 16.8

α	C_l	C_d
–40.0	–1.1115	1.0090
–30.0	–0.9753	0.6307
–21.0	–0.7471	0.3280
–17.5	–0.7874	0.2331
–15.0	–0.8179	0.1700
–11.0	–0.8580	0.0929
–10.9	–0.8563	0.0483
–10.0	–1.0000	0.0400
–7.5	–0.7692	0.0181
–5.0	–0.4998	0.0128
–2.0	–0.1998	0.0094
0.0	0.0000	0.0085
2.0	0.1998	0.0094
5.0	0.4998	0.0128
7.5	0.7692	0.0181
10.0	1.0000	0.0400
10.9	0.8563	0.0483
11.0	0.8580	0.0929
15.0	0.8179	0.1700
17.5	0.7874	0.2331
21.0	0.7471	0.3280
30.0	0.9753	0.6307
40.0	1.1115	1.0090

It is also possible to model a VAWT in 2-D using a discrete vortex model (DVM), by using the Kutta–Joukowski theorem, the Biot–Savart law and Kelvin's circulation theorem. The Kutta–Joukowski theorem, Equation 16.16, relates the lift of a 2-D airfoil to the so-called bound circulation, Γ_b.

$$l = \rho V_{rel} \Gamma_b \tag{16.16}$$

This can be combined with the definition of the lift coefficient to give

$$\Gamma_b = \tfrac{1}{2} V_{rel} c C_l \tag{16.17}$$

Knowing the circulations distributed in space $\Gamma(x_{vortex}, y_{vortex})$, one can calculate the induced velocity in any point (x_p, y_p) using Equation 16.8 which is a slightly modified Biot–Savarts law

$$u_{ind}(x_p, y_p) = \sum \frac{-(y_p - y_{vortex})\Gamma}{2\pi r^2}\left(1 - \exp\left(-\left(\frac{r}{\varepsilon}\right)^2\right)\right)$$
$$v_{ind}(x_p, y_p) = \sum \frac{(x_p - x_{vortex})\Gamma}{2\pi r^2}\left(1 - \exp\left(-\left(\frac{r}{\varepsilon}\right)^2\right)\right) \tag{16.18}$$

ε denotes a vortex core and basically prevents the velocities of Equation 16.18 to become infinitely large as the distance, r, from the point to the vortex becomes small.

The total velocity in each point is found by adding the induced wind to the free flow as

$$V_x = V_{o,x} + u_{ind}$$
$$V_y = V_{o,y} + v_{ind} \tag{16.19}$$

The relation of these basic equations to a 2-D VAWT model is shown in Figure 16.9, showing the vortex system behind one blade. At each time step, the relative velocity seen by the airfoil is found by first calculating the wind speed at the point of the blade and then adding the rotational speed just as in Equation 16.4. Then the angle of attack can be determined and the lift coefficient is found from tabulated airfoil data for the applied airfoil. It should be noted that a dynamic-stall model should be applied since the angles of attack vary periodically with the frequency of the rotation and may be large. With this the bound circulation on the airfoil is calculated using Equation 16.17. Further, Kelvin's circulation theorem must be applied, that states that the total amount of circulation stays constant, i.e.

$$\frac{d\Gamma}{dt} = 0 \tag{16.20}$$

To fulfil this, a new vortex has to be introduced at each time step with a circulation equal to the change of bound circulation from the present to the previous time step,

$$\Gamma_w(t) = -\Delta\Gamma_b = -\left(\Gamma_b(t) - \Gamma_b(t - \Delta t)\right) \tag{16.21}$$

The index, w, refers to the wake and the new vortex introduced in each time step simulates the shed vorticity in the wake behind the airfoil and is thus placed near the trailing edge. Then all the vortices in the wake are simply convected as in Equation 6.22 using the velocity at their respective positions, computed using the Biot–Savart law (Equation 16.18) and Equation 16.19.

$$x_{vortex}(t) = x_{vortex}(t - \Delta t) + V_x \cdot \Delta t$$
$$y_{vortex}(t) = y_{vortex}(t - \Delta t) + V_y \cdot \Delta t \tag{16.22}$$

Some examples of the computed placement of the vortices are shown in Figure 16.10 for a two-bladed VAWT at a tip speed ratio, λ, of 2.5 and 5, respectively.

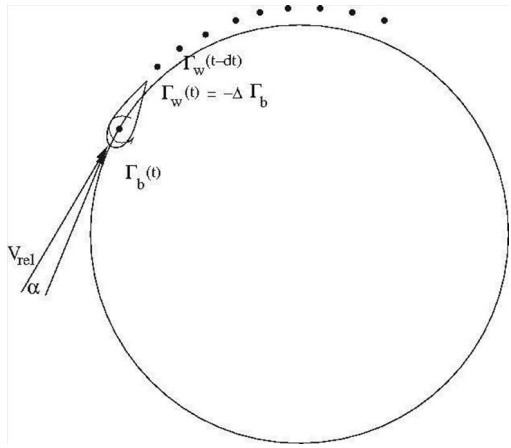

Figure 16.9 The vortex system behind a 2-D airfoil

It should be noted that at low tip speed ratios the dynamic-stall model may become very important but it cannot be modelled directly in the momentum method as described above, since the momentum model is basically a steady model in contrast to the vortex method.

Figure 16.11 and Figure 16.12 show the normal and tangential force coefficients calculated using the vortex method and the momentum method, respectively for a value of K=0.3 for λ=6, B=2 and a solidity of 0.1 and 0.3, respectively.

Alternatively one can apply a CFD model as, for example, described by Hansen and Sørensen (2001), where an inner part of the grid is rotated relative to the stationary outer grid, see Figure 16.13.

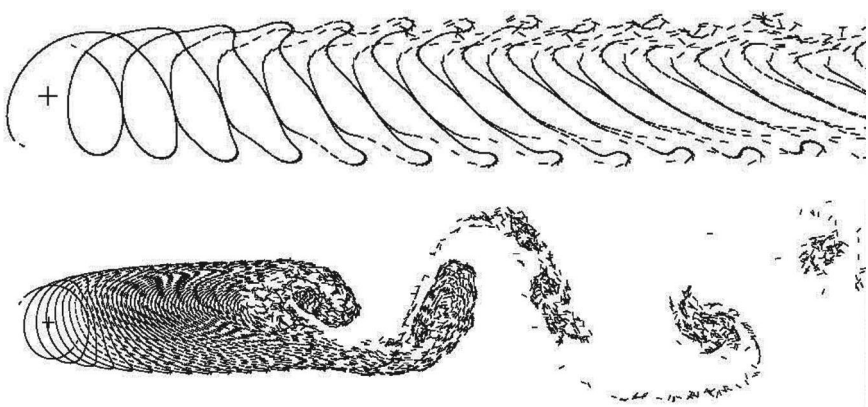

Figure 16.10 The computed vortex system behind a two-bladed VAWT for a tip speed ratio of 2.5 (above) and 5 (below)

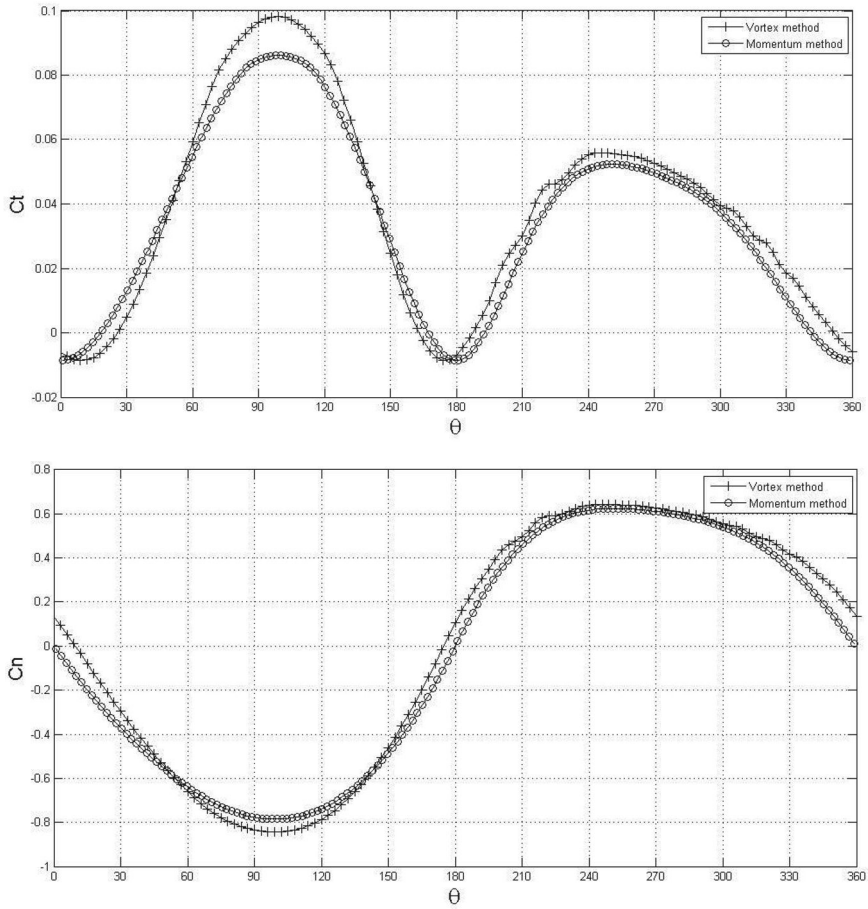

Figure 16.11 Comparison between the computed normal and tangential force coefficient using the momentum method (K=0.3) and the vortex method for S=0.1, B=2 and λ=6, yielding C_P=0.37 and C_T=0.67

Finally, the computed and non-dimensionalized normal and tangential loads are plotted in Figure 16.14 against an experiment by Oler et al. (1983) to give an impression of the accuracy of this type of model. It is noted that the force coefficients shown in Figure 16.14 are normalized with the wind speed and not the relative wind speed.

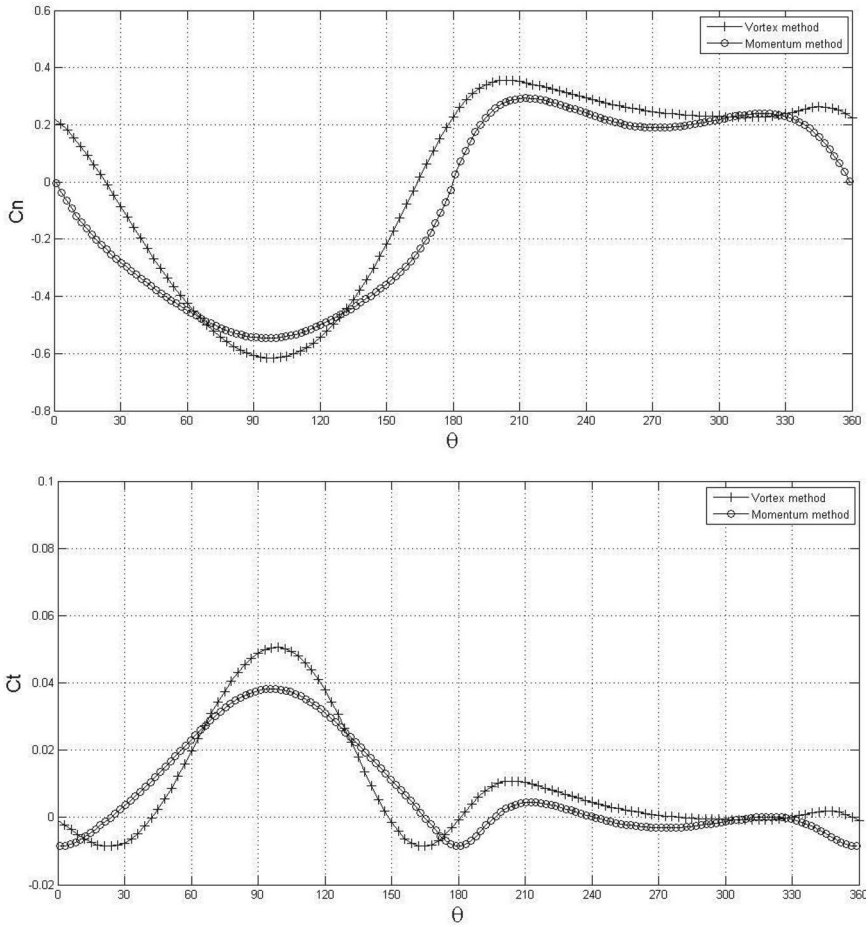

Figure 16.12 Comparison between the computed normal and tangential force coefficient using the momentum method (K=0.3) and the vortex method for S=0.3, B=2 and λ=6, yielding C_P=0.24 and C_T=1.15

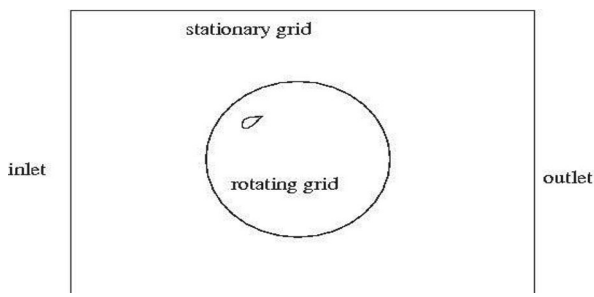

Figure 16.13 Sketch of a CFD grid for a VAWT showing an outer stationary part and an inner rotating part containing the rotor

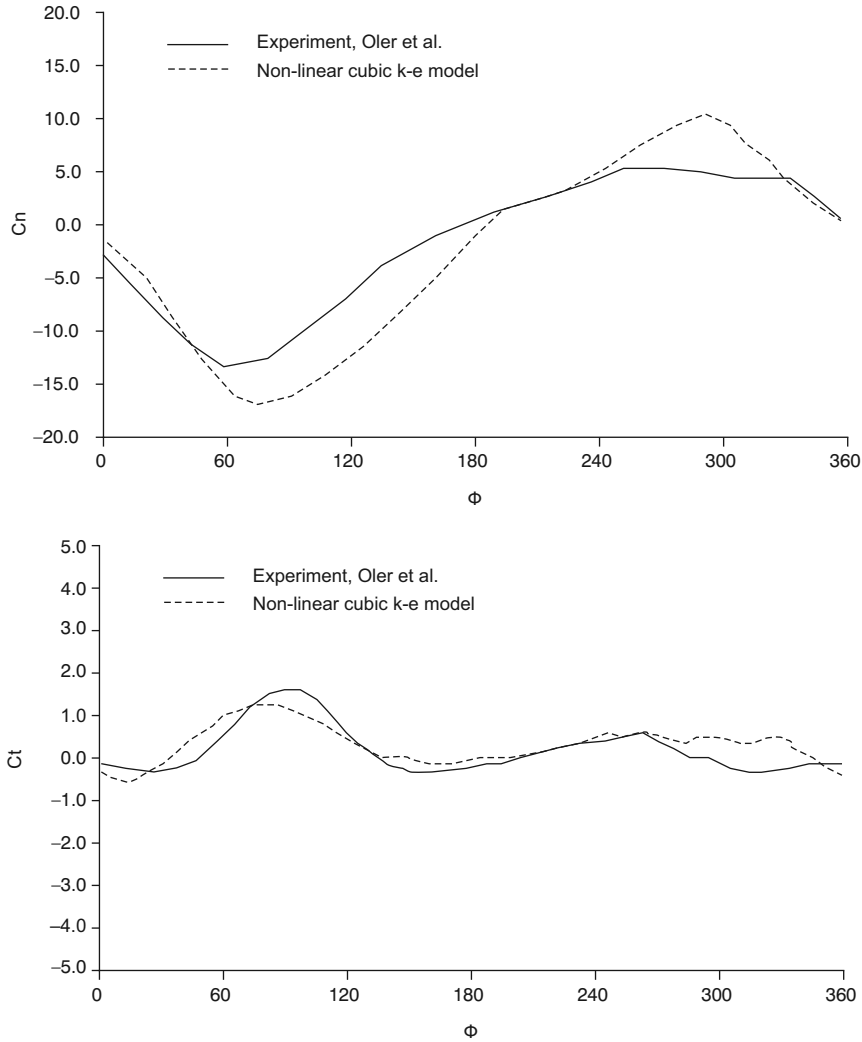

Figure 16.14 Comparison of computed and measured normal and tangential loads

References

Hansen, M.O.L. and Sørensen, D.N. (2001) 'CFD model for vertical axis wind turbine', *Proceedings of EWEC*, 2–6 June, pp. 485–488. Munich: WIP-Renewable Energies.

Oler, J.W., Strickland, J.H., Im, B.J. and Graham, G.H. (1983) *Dynamic Stall Regulation of the Darrieus Turbine* SAND83-7029. Livermore, CA: Sandia National Laboratories.

Paraschivoiu, I. (2002) *Wind Turbine Design: With Emphasis on Darrieus Concept*. Montreal: Polytechnic International Press.

Strickland, J. H., (1975) *The Darrieus Turbine: A Performance Prediction Model Using Multiple Streamtubes*, Sandia National Laboratory Report, SAND 75-041. Livermore, CA: Sandia National Laboratories.

17 Final remarks

The chapters in this book are intended to give an insight into wind turbine aerodynamics and aeroelasticity. The classical steady BEM method was outlined to model the steady performance of a given wind turbine to calculate the annual energy production for an actual site. The loads on a real wind turbine construction are, however, very dynamic, mainly due to gravity and the varying inflow conditions from wind shear, tower shadow and, not least, atmospheric turbulence. All the theory and equations needed to write an unsteady BEM have been given in this book, including all necessary engineering models, such as dynamic inflow, dynamic stall and yaw/tilt models. Further, a method to build a structural model of a wind turbine construction was outlined in order to be able to calculate the dynamic structural response of the different components when exposed to the unsteady loads. The structural vibrations couple back to the aerodynamics through the local velocities that must be subtracted from the wind speed when estimating the angles of attack and thus directly influence the loads. The aerodynamics and structural dynamics are therefore strongly coupled and comprise a so-called aeroelastic problem in which both models must be solved simultaneously in the time domain. During an aeroelastic simulation the aerodynamic model must be called many times (once for every time step) and a fast model is thus required. The BEM method is simple but very fast and will therefore very likely be used for many years to come. However, more advanced tools as CFD (computational fluid dynamics) has made huge progress in the past few years, not least due to advances in processor speed and storage capacity of modern computers. In CFD the domain around the object is divided into a computational grid and for each gridpoint the Navier–Stokes equations (Equations A10–13) are discretized, and the result is a large number of coupled non-linear equations that must be solved numerically; and further if an unsteady solution is sought they must be solved for each time step. Another problem is the variety of scales present in the actual flow, ranging from very tiny turbulent eddies to large scale in the order of the rotor diameter. Solving the equations in a computational grid that resolves all the scales will be impossible for many years since the size of the equation system is enormous. To overcome this, the smallest eddies are modelled with a turbulence model that basically models the extra mixing from the small-scale turbulence. The

existing turbulence models are often calibrated for various different flows and therefore their use introduces additional uncertainty to the computed results. One of the very first papers using CFD on wind turbines is Hansen et al. (1997). More recent calculations (Sørensen and Michelsen, 2000; Duque et al., 1999) of the NREL experiment described in Fingersh et al. (2001) and Simms et al. (2001) have shown excellent agreement between the experiment and the CFD computations. Even though CFD has improved, it is still far too slow to be used in an aeroelastic computation, and wind turbines will for many years still be designed and optimised using BEM methods. However, it is very natural to check the final result using CFD to validate the design and to see, for example, if there are unwanted areas of separation or to investigate the influence of different tip geometries as, for example, made in Hansen and Johansen (2004).

In the so-called actuator line model (Sørensen and Shen, 2002) CFD is used to resolve the wake dynamics and thus the induced velocity at the rotor plane can also be evaluated. Knowing the induced velocities, the local angles of attack can be estimated, just as in the BEM approach, along the blades and the loads are then found from tabulated airfoil data and distributed in the computational grid along lines at the actual blade positions. Since the actuator line model is not resolving the boundary layers on the blades, it is relatively fast and can be made to run in the time domain and be coupled with a dynamic structural model to perform full aeroelastic computations. Using the actuator line model, the effects from yaw and dynamic inflow is a direct output of the Navier–Stokes equations and the results can be used to tune the engineering models in the BEM method.

Further, the actuator line model is very suitable for, and therefore often used to quantify, the dynamic wake effect from upstream wind turbines, since the wakes generated from these hit the downwind turbines and affect the loads.

The author wishes the best of luck to anybody who pursues the task of using and developing aeroelastic models for wind turbines to harvest more efficiently the vast energy resources contained in the wind.

References

Duque, E.P.N., van Dam, C.P. and Hughes, S. (1999) 'Navier–Stokes simulations of the NREL combined experiment phase II rotor', *Proceedings ASME Wind Energy Symposium*, January, Reno, NV.

Fingersh, L.J., Simms, D., Hand, M., Jager, D., Contrell, J., Robinson, M., Schreck, S. and Larwood, S. (2001) 'Wind tunnel testing of NREL's unsteady aerodynamics experiment' AIAA-2001-0035 Paper, 39th Aerospace Sciences Meeting & Exhibition, 8–11 January, Reno, NV.

Hansen, M.O.L and Johansen, J. (2004) 'Tip studies using CFD and Comparison with tip loss models', *Wind Energy*, 7: 343–356.

Hansen, M.O.L., Sørensen, J.N., Michelsen, J.A. and Sørensen, N.N. (1997) 'A global Navier–Stokes rotor prediction model', AIAA 97-0970, 35th Aerospace Sciences Meeting and Exhibit, 6–10 January, Reno, NV.

Simms, D., Schreck, S., Hand, M. and Fingersh, L.J . (2001) *NREL Unsteady Aerodynamics Experiment in the NASA-Ames Wind Tunnel: A Comparison of Predictions to Measurements* NREL/TP-500-29494. Internal NREL report.

Sørensen, J.N. and Shen, W.Z. (2002) 'Numerical modeling of wind turbine wakes', *Journal of Fluids Engineering – Transactions of the ASME*, 124(2): 393–399.

Sørensen, N.N. and Michelsen, J.A. (2000) *Aerodynamic Predictions for the Unsteady Aerodynamics Experiment Phase-II Rotor at the National Renewable Energy Laboratory* AIAA-2000-0037, ASME Wind Energy Symposium, 10–13 January, Reno, NV.

Appendix A
Basic fluid mechanics equations

In a fluid with no individual solid particles, it is common to consider a fixed volume in space denoted a control volume *CV*. Newton's second law is:

$$\mathbf{F} = \frac{d\mathbf{P}}{dt} \tag{A.1}$$

where $\mathbf{F}=(F_x, F_y, F_z)$ is the total force, $\mathbf{P}$ is the momentum and t is the time. The time derivative of the momentum $\mathbf{P}$ is found from integrating over the control volume as:

$$\frac{d\mathbf{P}}{dt} = \frac{\partial}{\partial t}\iiint_{CV} \rho \mathbf{V} d(Vol) + \iint_{CS} \mathbf{V}\rho\mathbf{V}\cdot\mathbf{dA} \tag{A.2}$$

where ρ is the density, $\mathbf{V}$ is the velocity, $d(Vol)$ is an infinitesimal part of the total control volume, *CS* denotes the surface of the control volume and $\mathbf{dA}$ is a normal vector to an infinitesimal part of the control surface. The length of $\mathbf{dA}$ is the area of this infinitesimal part. Newton's second law for the control volume then becomes:

$$\frac{\partial}{\partial t}\iiint_{CV} \rho \mathbf{V} d(Vol) + \iint_{CS} \mathbf{V}\rho\mathbf{V}\cdot\mathbf{dA} = \mathbf{F} \tag{A.3}$$

where $\mathbf{F}$ is the total external force including the pressure and viscous forces acting on the control surfaces. Further, body forces, for example, gravity, and forces from the flow past an object inside the control volume contribute to the total force. Equation A.3 is normally used to determine an unknown force provided that the velocity is known at the control surfaces. When Stoke's hypothesis for an incompressible fluid, Equations A.4–A.9, are used for the stresses on an infinitesimal control volume with side lengths (dx,dy,dz) the three partial differential momentum equations (A.11), (A.12) and (A.13) are derived. The first subscript on τ indicates the face, where the stress is located, and the second subscript is the direction of the stress:

$$\tau_{xx} = -p + 2\mu\frac{\partial u}{\partial x} \tag{A.4}$$

$$\tau_{xy} = \tau_{yx} = \mu\left(\frac{\partial u}{\partial y} + \frac{\partial v}{\partial x}\right) \tag{A.5}$$

$$\tau_{xz} = \tau_{zx} = \mu\left(\frac{\partial u}{\partial z} + \frac{\partial w}{\partial x}\right) \tag{A.6}$$

$$\tau_{yy} = -p + 2\mu\frac{\partial v}{\partial y} \tag{A.7}$$

$$\tau_{yz} = \tau_{zy} = \mu\left(\frac{\partial v}{\partial z} + \frac{\partial w}{\partial y}\right) \tag{A.8}$$

$$\tau_{zz} = -p + 2\mu\frac{\partial w}{\partial z} \tag{A.9}$$

$p(x,y,z,t)$ denotes the pressure, $\mathbf{V}(x,y,z,t)=(u,v,w)$ are the velocity components, $\mathbf{x}=(x,y,z)$ are the coordinates in a cartesian frame of reference and μ is the viscosity.

The three momentum equations (A.11), (A.12) and (A.13) plus the continuity equation (A.10) comprises the Navier–Stokes equations for an incompressible fluid with constant viscosity μ:

$$\frac{\partial u}{\partial x} + \frac{\partial v}{\partial y} + \frac{\partial w}{\partial z} = 0 \tag{A.10}$$

$$\rho\left(\frac{\partial u}{\partial t} + u\frac{\partial u}{\partial x} + v\frac{\partial u}{\partial y} + w\frac{\partial u}{\partial z}\right) = -\frac{\partial p}{\partial x} + \mu\left(\frac{\partial^2 u}{\partial x^2} + \frac{\partial^2 u}{\partial y^2} + \frac{\partial^2 u}{\partial z^2}\right) + f_x \tag{A.11}$$

$$\rho\left(\frac{\partial v}{\partial t} + u\frac{\partial v}{\partial x} + v\frac{\partial v}{\partial y} + w\frac{\partial v}{\partial z}\right) = -\frac{\partial p}{\partial y} + \mu\left(\frac{\partial^2 v}{\partial x^2} + \frac{\partial^2 v}{\partial y^2} + \frac{\partial^2 v}{\partial z^2}\right) + f_y \tag{A.12}$$

$$\rho\left(\frac{\partial w}{\partial t} + u\frac{\partial w}{\partial x} + v\frac{\partial w}{\partial y} + w\frac{\partial w}{\partial z}\right) = -\frac{\partial p}{\partial z} + \mu\left(\frac{\partial^2 w}{\partial x^2} + \frac{\partial^2 w}{\partial y^2} + \frac{\partial^2 w}{\partial z^2}\right) + f_z \tag{A.13}$$

Equation A.10 ensures that the net mass flow is zero in and out of an infinitesimal box with side lengths dx,dy,dz. Equations A.11, A.12 and A.13 are Newton's second law in the x,y and z direction respectively, for an infinitesimal box in the fluid, which is fixed in space. The left hand side terms are the inertial forces and the right hand terms are the pressure forces, the viscous forces and the external body forces $\mathbf{f}(t,x,y,z)=(f_x,f_y,f_z)$ acting on the box, respectively. Equations A.11, A.12 and A.13 can also be written in vector notation as:

$$\rho\left(\frac{\partial \mathbf{V}}{\partial t} + (\mathbf{V}\cdot\boldsymbol{\nabla})\mathbf{V}\right) = -\nabla p + \mu\nabla^2\mathbf{V} + \mathbf{f} \tag{A.14}$$

If no external forces are present and if the flow is stationary and the viscous forces are zero, Equation A.14 reduces to:

$$-\frac{\nabla p}{\rho} = (\mathbf{V}\cdot\boldsymbol{\nabla})\mathbf{V} = \frac{1}{2}\nabla(\mathbf{V}\cdot\mathbf{V}) - \mathbf{V}\times(\boldsymbol{\nabla}\times\mathbf{V}) \tag{A.15}$$

The last equality in Equation A.15 comes from a vector identity. If the flow is irrotational, i.e. $\nabla \times \mathbf{V}=0$, the Bernoulli equation (A.16) comes directly from Equation A.15 and is valid between any two points in the flow domain:

$$p + \tfrac{1}{2}\rho(u^2 + v^2 + w^2) = const \tag{A.16}$$

If the flow is not irrotational it can be shown from Equation A.15 that the Bernoulli equation (A.16) is still valid but only along a streamline.

To use the Bernoulli equation it is necessary that the flow is stationary, that no external forces are present and that the flow is incompressible and frictionless. The Bernoulli equation is generally valid along a streamline but if the flow is irrotational the equation is valid between any two points.

The Navier–Stokes equations are difficult to solve and often the integral formulation equation (A.3) is used in engineering problems. If the flow is stationary and the torque on the sides of an annular control volume is zero the integral moment of momentum equation (A.17) becomes:

$$\mathbf{M} = \iint_{CS} \mathbf{r} \times \mathbf{V} \rho \mathbf{V} \cdot \mathbf{dA} \tag{A.17}$$

where $\mathbf{M}$ is an unknown torque acting on the fluid in the control volume and $\mathbf{r}$ is the radius from the cylindrical axis. If the flow is uniform at the inlet and exit of the control volume and the only non-zero component of $\mathbf{M}$ is in the flow direction z, Euler's turbine equation (A.18) can be derived from Equation A.17:

$$P = M_z \omega = \omega \dot{m}(r_1 V_{\theta,1} - r_2 V_{\theta,1}) \tag{A.18}$$

P is power removed from the flow on a mechanical shaft, ω is the rotational speed of the shaft, V_θ is the tangential velocity component, $\dot{m}$ is the mass flow through the control volumes and subscripts 1 and 2 denote the inlet and exit of the control volume, respectively.

Another important equation is the integral conservation of energy or the first law of thermodynamics for a control volume, which for steady flow is Equation A.19:

$$P + Q = \iint_{CS} \left(u_i + \frac{p}{\rho} + \tfrac{1}{2}(u^2 + v^2 + w^2 \right) \rho \mathbf{V} \cdot \mathbf{dA} \tag{A.19}$$

where P and Q are the mechanical power and the rate of heat transfer added to the control volume and u_i is the internal energy.

Appendix B
Symbols

A	rotor area, scaling factor
a	axial induction factor, tower radius
a'	tangential induction factor
$\mathbf{a_{AB}}$	transformation matrix from system A to B
a_n	Fourier coefficient
B	number of blades
b_n	Fourier coefficient
$\mathbf{C}$	damping matrix
c	chord
C_l	lift coefficient
C_d	drag coefficient
C_p	power coefficient
C_T	thrust coefficient
C_m	moment coefficient
C_n	normal load coefficient
C_q	azimuthal component of axial velocity
C_t	tangential load coefficient
D	rotor diameter, drag
d	2-D drag
$\mathbf{dA}$	normal vector to area
E	modulus of elasticity
ED	moment of centrifugal stiffness
EI	moment of stiffness inertia
ES	moment of stiffness
$\mathbf{F}$	force (vector)
$\mathbf{F}_g$	generalized force (vector)
F	force, Prandtl's tip loss correction
$\mathbf{f}$	external body force (vector)
f	force, probability, frequency
f_n	frequency in discrete Fourier transformation
f_s	separation function
GI	torsional stiffness
H	tower height, form factor

h	height above ground level
h_w	Weibull distribution
I	moment of inertia, turbulence intensity
$\mathbf{K}$	stiffness matrix
k	form factor
k_t	terrain factor
L	mift, distance between two points in space
l	length scale, 2-D lift
$\mathbf{M}$	torque (vector), mass matrix
M	torque, aerodynamic moment
m	mass per length
$\dot{m}$	mass flow
M_G	generator torque
M_{flap}	flapwise bending moment
Ma	Mach number
n	rotational speed of shaft
$\mathbf{P}$	momentum (vector)
P	power
p	pressure, load
p_c	centrifugal load
p_N	load normal to rotorplane
PSD	power spectral density function
p_T	load tangential to rotorplane
Q	rate of heat transfer
q_{2s}	dynamic pressure based on V_{2s}
R	rotor radius
R	resistance
$\mathbf{r}$	radius (vector)
r	radius
Re	Reynolds number
S_{ij}	coherence function
SL	slip
T	thrust, total time
t	time
U	boundary layer edge velocity
u	x-component of velocity vector, axial velocity at rotorplane, deflection
$\dot{u}$	structural velocity
$\ddot{u}$	structural acceleration
u_l	velocity in wake
u^{1f}	deflection first flapwise eigenmode
u^{1e}	deflection first edgewise eigenmode
u^{2f}	deflection second flapwise eigenmode
u_i	internal energy
$\mathbf{V}$	velocity (vector)

v	angle between chordline and first principle axis
v	y-component of velocity vector
V_2	velocity in rotor plane for a shrouded rotor
V_{2s}	time averaged wind speed over a period of 2 seconds
V_{10min}	time averaged wind speed over a period of 10 minutes
$\mathbf{V_b}$	blade velocity (vector)
V_o	wind speed
V_q	tangential velocity component
V_{rel}	relative velocity to airfoil
V_μ	velocity at infinity
w	z-component of velocity vector
$\mathbf{w}$	induced velocity
W_y	tangential component of induced velocity
W_z	normal component of induced velocity
x	local tip speed ratio
z_o	roughness length

Greek

α	angle of attack
β	twist of blade
Γ	circulation
Δt	time increment
δ	boundary layer thickness
δ^*	displacement thickness
ε	augmentation factor, strain
θ	momentum thickness, local pitch
θ_{cone}	cone angle
θ_o	azimuthal position where blade is deepest into the wake
θ_p	pitch angle
θ_{wing}	azimuthal position of blade
θ_{yaw}	yaw angle
λ	tip speed ratio
μ	dynamic viscosity
ν	kinematic viscosity, wind shear exponent
ρ	density
σ	solidity, stress, standard deviation
σ_r	stress range
σ_m	mean stress
τ	shear stess, time constant
ϕ	flow angle
χ	wake skew angle
ω	angular velocity of rotor, eigenfrequency
ω_n	frequency in discrete Fourier transformation

Index